Measurements of Prompt Λ_c^+/D^0 Ratio as a Function of Multiplicity at the ALICE Experiment: An Investigation of Charm Hadronization in Small Systems

by
Oveis Sheibani

A dissertation submitted to the Department of Physcis,

College of Natural Sciences and Mathematics

in partial fulfillment of the requirements for the degree of

Doctor of Philosophy
in Physics

Chair of Committee: Rene Bellwied

Committee Member: Claudia Ratti

Committee Member: Greg Morrison

Committee Member: Demetrio Labate

University of Houston
May 2024

DEDICATION/EPIGRAPH

To my father, Ammar Sheibani (1969-2022), who left us early but whose love lives with us. He was the kindest father I could have asked for, and I hope to always have his blessing in my life.

ACKNOWLEDGEMENTS

I would like to express my profound gratitude to my mother, Atash Ashrafi, for her dedication to my education. I am also deeply thankful to both of my grandmothers, Monireh Fazeli and Pourandokht Yavari, for their lifelong support for our family. I appreciate the encouragement and support of my undergraduate professors at my home School Sharif University of Technology, Dr. Reza Ejtehadi, Dr. Saman Moghimi, Dr. Shant Baghram, and Dr. Ahmad Amjadi for their mentorship and the invaluable lessons I have learned from them. I am grateful to Dr. Cristina Terrevoli, our postdoctoral fellow, for her guidance during this project. I would also like to thank my PhD committee member, Dr. Demetrio Labate, for his contributions during these years. I would like to acknowledge Dr. Greg Morrison for his great classes in statistical mechanics, which were significantly important in understanding the foundation of my research especially the Brownian motion and thermalization. A special acknowledgment goes to my advisors, Dr. Rene Bellwied and Dr. Claudia Ratti, who are exceptional human beings, brilliant physicists, and inspiring teachers, and who gave kind unconditional support to their students. I had a great chance to be one of their students.

ABSTRACT

In this dissertation, the measurement of the prompt Λ_c^+/D^0 ratio as a function of multiplicity in p-Pb collisions at mid-rapidity at $\sqrt{s_{NN}} = 5.02$ TeV is discussed. By performing this measurement as a function of multiplicity in p-Pb collisions and by comparing to similar measurments in pp collisions, we can evaluate the p_T-differential baryon to meson enhancement and relate it to results in e^+e^- and ep collisions, where lower Λ_c^+/D^0 ratios at low and intermediate p_T have been observed. The origin of this discrepancy, which leads to the breakdown of the so-called factorization theorem for the elementary particle collisions, is still being debated. We aim to compare the p-Pb results not only to pp collisions to investigate the possible effects of cold nuclear matter, but to Pb-Pb collisions to study the impact of quark–gluon plasma formation on charm quark hadronization. This dissertation, aims to understand the charm quark hadronization in small systems by its evaluation as a function of system size. We also examine event generators alongside experimental data, both of which are essential to understanding the physics of interest and evaluate detector effects. Our goal is to investigate various models that implement different mechanisms of hadronization, to see where they match or differ from the data. In event generators, we have the ability to manipulate various parameters of the system's dynamics, allowing us to isolate different effects and modes and understand their influence on the final observations. Such comparisons reveal whether we have accurately understood the physics of hadronization. Specifically, we discuss PYTHIA, a time dynamical event generator, and compare its performance against models that incorporate statistical and thermal approaches such as Statistical Hadronization Model (SHM), and Quark (re) Combination Model (QCM). We discuss how these models perform at explaining features of the transition of the system from pp to p-Pb and Pb-Pb.

Contents

LIST OF TABLES

LIST OF FIGURES

1 Theory

1.0.1 Atomic and subatomic age: 1897 to 1950

The discovery of the electron marked the first identification of what was later understood to be a fundamental particle. At the time of its discovery, it was not known to be a fundamental constituent of atoms. Today, the electron is still considered a fundamental particle, but other fundamental particles have been added to the list over the next decades. In J.J. Thomson's 1897 experiments, the voltage applied between the cathode and anode in the cathode ray tube ranged from 20 to 400 volts and this voltage range was enough to accelerate electrons from the cathode towards the anode, providing the necessary kinetic energy for the electrons to travel through the tube. By measuring how these electrons were deflected by electric and magnetic fields positioned perpendicular to their trajectory, Thomson was able to calculate the charge-to-mass ratio (e/m) of the electrons. Building upon Thomson's work, Robert A. Millikan conducted the oil-drop experiment in 1909 to measure the charge of the electron directly. Adjusting the voltage to balance the gravitational and electrical forces on charged oil droplets allowed Millikan to calculate the charge precisely by knowing the total charge transformed to the droplets. The experiments by Thomson and Millikan were conducted under conditions where relativistic effects are negligible due to the relatively low speeds of the electrons (compared to the speed of light) while relativistic effects becomes very important in quantum mechanics and elementary particle physics. To accurately determine if a particle is fundamental, one must explore increasingly smaller scales. After the discovery of the proton by Ernest Rutherford in his famous gold foil experiment, it was believed to be a fundamental particle. Paul Dirac theorized the existence of antimatter in 1928 through his equation, which implied a symmetry between electrons and an as-yet undiscovered particle, the positron. Initially, he speculated that this particle might be the proton, but this was incorrect due to the mass disparity. The actual counterpart, the positron, was experimentally discovered by Carl Anderson in 1932, confirming Dirac's prediction and solidifying the

concept of particle-antiparticle symmetry in quantum physics. Later, the discovery of the neutron by James Chadwick in 1932, revealed another particle inside the nucleus that is neutral but strongly bound to the proton. Werner Heisenberg attempted to explain the symmetry between the proton and neutron by introducing the concept of isospin as a quantum number to understand the symmetry between protons and neutrons, suggesting they could be treated as two states of the same particle, known as the nucleon. This concept was the basis in modeling the strong nuclear force, which binds protons and neutrons together in the nucleus.

Hideki Yukawa in 1935 introduced a theoretical framework to explain the strong nuclear force, the interaction responsible for holding protons and neutrons together in an atomic nucleus. He proposed the existence of a mediator particle, which we now know as the pion, to account for this force. The theory was grounded in a mathematical formulation known as the Yukawa potential,

$$V(r) = -\frac{g^2}{r}e^{-mr} \tag{1}$$

where $V(r)$ is the potential energy as a function of distance r, g represents the coupling constant of the interaction, m is the mass of the mediator particle. Based on this theory, Yukawa predicted the mass of the mediator particle to be about 200 times that of the electron, approximately 100 MeV/c^2. This prediction initially led to the misidentification of the muon, discovered in 1936, by Carl D. Anderson and Seth Neddermeyer at Caltech, during their study of cosmic ray particles. Muons are created in the upper atmosphere through the collision of cosmic rays with atoms and are able to reach the Earth's surface due to their relatively long lifespan of 2.2 microseconds for subatomic particles, which allows them enough time to descend through the atmosphere and be detected. Despite being about 207 times more massive than electrons, muons are unstable and decay into electrons and neutrinos, and their existence and properties have been instrumental in the development and confirmation of particle physics theories. However, the muon did not interact with the nucleus as expected for the mediator of the strong force. It was not until the discovery of the actual pion in

1947 that Yukawa's prediction was fully validated, confirming the existence of the particle responsible for mediating the strong nuclear force, with a mass in the correct range as Yukawa had predicted. Between the discovery of the pion and the formulation of the quark model in the early 1960s, dozens of hadrons were discovered, leading to what was known as the "particle zoo." This period was marked by confusion and fascination as physicists attempted to understand the array of particles being found in cosmic rays and particle accelerator experiments. Among the most important discoveries were the kaons and lambda particles, which introduced the concept of strangeness, a quantum number that helped explain why some particles decayed more slowly than expected. Since 1960, advancements in accelerator technology have enabled the collision of various particle types, leading to the evolution of Hadronic Physics. For a period, physicists, faced with the diverse array of hadrons, lacked a systematic method for categorization similar to the periodic table of elements. Before the quark model, the observed non-conservation of strangeness in weak decays puzzled scientists. Strangeness, conserved in strong interactions but not in weak ones, hinted at deeper particle structures. The quark model explained this by allowing strange quarks to transform into up or down quarks during weak decays, changing the strangeness quantum number.

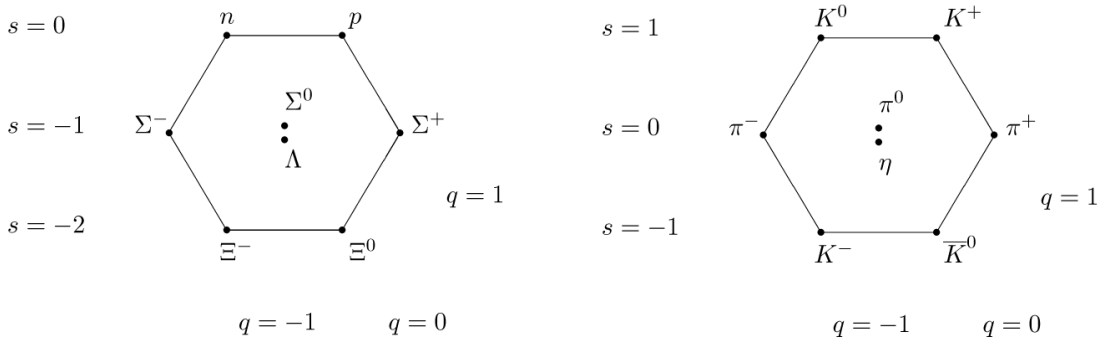

Figure 1: Eightfold Way of mesons (right) and baryons (left) organizing the hadrons based on their quantum numbers: isospin, strangeness, and charge.

After the discovery of the kaon (K) in 1947, a series of strange particles were identified. The Lambda particle (Λ) was discovered in 1950. The Sigma particles (Σ) were identified in the early 1950s, followed by the Xi particles (Ξ). The Omega (Ω^-), discovered at Brookhaven National Laboratory in 1964, was important. Before the concept of quarks was fully accepted, physicists used the quantum number of strangeness to explain the unusual properties of certain particles. They observed that the Ω^- had a much longer lifetime than expected for its mass, indicating a high degree of strangeness. The strangeness quantum number, initially an abstract property to account for observed behaviors, was key in piecing together the puzzle of subatomic particle structure. The concept of strangeness was introduced by Murray Gell-Mann and Kazuhiko Nishijima in the early 1950s as a way to explain the unexpected long lifetimes of certain particles (see Figure 1).

1.0.2 Hagedorn and prediction of phase change

During the 1960s, the discovery of a large number of hadronic particles, which were resonances with various masses and lifetimes, presented a challenge. The bootstrap model in particle physics, often associated with the concept of "nuclear democracy," suggests that all hadrons (particles made of quarks and participating in strong interactions like protons and neutrons) are equally fundamental and can be considered as bound states or resonances of each other. The relationship with Hagedorn comes from his concept of a limiting temperature for hadronic matter, known as the Hagedorn temperature. Physicists noticed that the properties of hadrons, such as their spin and mass, seemed to be related in a way that could be described by straight lines when plotted on a graph (with the spin on one axis and the mass squared on the other). These lines are called Regge trajectories. The bootstrap model, with its idea of particles being composites of each other, naturally incorporates the concept of Regge trajectories, as it implies that the resonances (excited states) of hadrons should align along these trajectories.

The term "bootstrap" in general vocabulary and its concept in physics both draw from the metaphor of "pulling oneself up by one's bootstraps." In common usage, this phrase refers to an impossible task, originally meant to depict the absurdity of someone attempting to lift themselves off the ground by pulling on their bootstraps. Over time, it evolved to symbolize a process of self-initiation or self-sustaining progress without external input. The central idea of the Statistical Bootstrap Model is that hadrons are made up of other hadrons. This self-similar structure suggests that inside each hadron, there are other hadrons, which in turn contain other hadrons, and so on. This concept was somewhat analogous to Russian nesting dolls, where each layer reveals similar but smaller dolls inside. Hagedorn introduced the concept of a limiting temperature, T_H, for hadronic matter. According to his model, as the energy pumped into a system of hadrons increases, the system approaches a temperature T_H beyond which it cannot be heated further. Instead of increasing in temperature, the added energy leads to the production of more and more massive resonance states. This limiting temperature is now interpreted in the context of the phase transition between hadronic matter and quark-gluon plasma. The model states that the number of hadronic states or resonances (N) as a function of mass (m) grows exponentially. This can be represented as: $\rho(m) \sim e^{\frac{m}{T_H}}$ where: $\rho(m)$ is the density of states at mass m, T_H is the Hagedorn temperature, a scale factor that characterizes the growth rate of the spectrum, m is the mass of the resonance. This equation suggests that for higher masses, the number of available states increases dramatically, reflecting the observed proliferation of hadronic resonances. The concept of the limiting temperature, T_H, emerges from the thermodynamics applied to this model. As energy is added to a hadronic system, it leads to the creation of heavier resonances instead of indefinitely increasing the temperature of the system. At the Hagedorn temperature, the system undergoes a phase transition, as adding more energy does not increase the temperature but changes the state of matter. The partition function $Z(T)$ in statistical mechanics is the tool, summing over all possible states of the system, weighted by their energy. For a system of hadrons, the partition function can be written considering the density of states $\rho(m)$ and

the Boltzmann factor $e^{-\frac{m}{T}}$, and ntegrating over all masses:

$$Z(T) = \int_0^\infty \rho(m) e^{-\frac{m}{T}} dm$$

Substituting the exponential growth of $\rho(m)$:

$$Z(T) = \int_0^\infty e^{\frac{m}{T_H} - \frac{m}{T}} dm$$

This integral converges (i.e., the system can be described thermodynamically) only if $T < T_H$. As T approaches T_H, the system reaches a point where the traditional hadronic description breaks down, indicating a phase transition. [1, 2, 3]

Gell-Mann's work on quantum numbers and the proposal of an SU(3) gauge symmetry aimed to provide a systematic framework for the conservation of these numbers in strong reactions [4, 5], In 1964, building on this foundation, Gell-Mann proposed a model in which hadrons were not fundamental particles but were composed of smaller entities he called "quarks." According to this model, protons, neutrons, and other hadrons were made up of quarks, which came in different types and flavors. This quark model offered a unified explanation for the composition and properties of hadrons, introducing a new layer of structure to the known atomic substructure and suggesting a more fundamental basis for the observed patterns in particle physics [6]. In vocabulary, the word "quark" doesn't have a meaning outside of its scientific context. It was famously coined by the physicist Murray Gell-Mann, who borrowed the term from James Joyce's novel "Finnegans Wake." In the book, the phrase "Three quarks for Muster Mark!" appears, and Gell-Mann was intrigued by the word. He liked the sound of it and decided to use it to name the fundamental constituents of hadrons, which he had proposed in his theoretical framework.

Quark existence was confirmed by deep inelastic scatterings (see Figure 2). These experiments

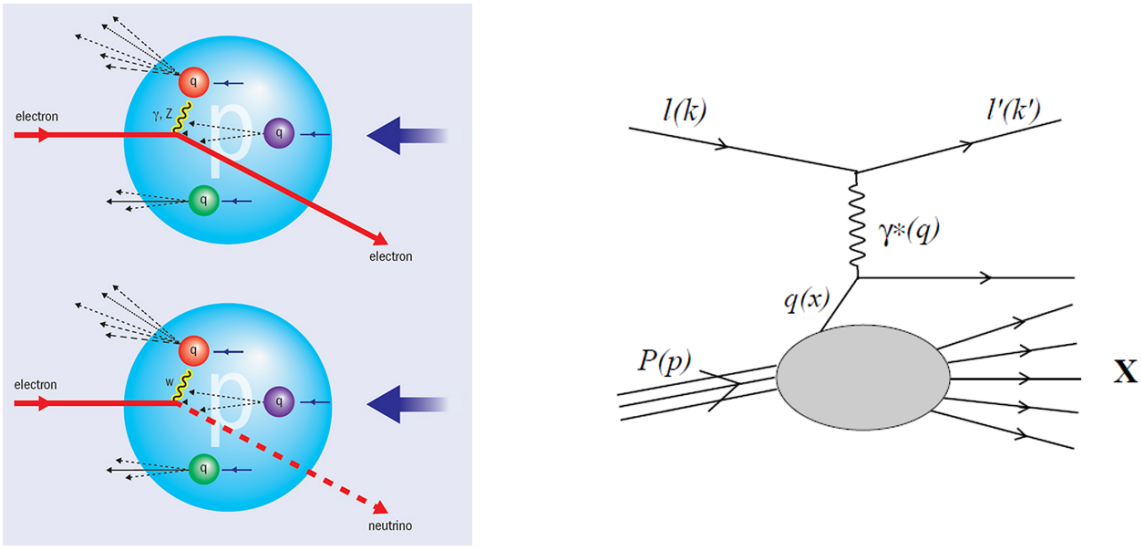

Figure 2: In deep inelastic scattering experiments, the interaction between electrons and protons can reveal the inner structure of the proton through point-like scattering centers, which have a mass comparable to that of the proton.

were conducted in the late 1960s at the Stanford Linear Accelerator Center SLAC, confirming the electric charge and spin of the quarks,[7, 8]. These studies provided the first convincing evidence of quarks, which until then had been largely theoretical constructs. Henry Way Kendall, Jerome Isaac Friedman, and Richard E. Taylor were awarded the Nobel Prize in 1990 for these pioneering investigations. However the experiments were indicating that the majority of masses of hadrons comes from the strong force not the individual quarks. The measured masses of quarks, as revealed through deep inelastic scattering experiments, highlighted a puzzle in particle physics. The masses of up and down quarks, the primary constituents of protons and neutrons, were discerned to be merely a few MeV (mega electron-volts), a scale significantly lower than the masses of the hadrons themselves. A proton has a mass of about 938 MeV, and a neutron is similarly massive, around 940 MeV. This contrast raised questions about the origin of mass in hadrons, suggesting that the simple sum of quark masses could not account for the total mass of a hadron. Compared to the electron, with its mass of approximately 0.5 MeV, quarks are indeed heavier, yet their contribution to the hadron mass seemed disproportionately small. Furthermore, the spin of hadrons became another aspect

of their internal structure. Each quark carries a spin of 1/2, similar to electrons and other fermions. However, the way these spins combine within hadrons, considering the angular momentum and the orbital motion of quarks bound by gluons, contributes to the overall spin of the hadron (proton spin crisis). For instance, the proton and neutron, each with a spin of 1/2, require a delicate quantum mechanical combination of their constituent quarks' spins and orbital angular momenta. This aspect of hadron structure emphasized the complexity of the internal dynamics beyond the simple addition of constituent spins. Murray Gell-Mann's introduction of the term "Quantum Chromodynamics" (QCD) for the theory of the strong interaction indeed incorporates the Greek word "chromo," meaning color. Although the detailed concept of color charge as it is understood today was further developed by others after Gell-Mann's initial work, the term QCD and the notion of "color" were used by the need to introduce an additional degree of freedom for quarks to solve theoretical problems in the quark model. The quark model, as initially proposed by George Zweig in 1964, faced a significant challenge in explaining how particles like baryons, which consist of three quarks, could exist without violating the Pauli Exclusion Principle, given that the quarks in such particles often appeared to be in identical quantum states. Color was introduced as a way to distinguish quarks beyond their flavor and spin, allowing for the construction of baryons and mesons in a manner consistent with observed symmetries and the Pauli Exclusion Principle. While Gell-Mann did not initially detail the dynamics of color charge interactions as later described by Quantum Chromodynamics, his choice of the term "chromodynamics" reflected an anticipation of the need for such an internal quantum number or charge to fully account for the behavior of quarks under the strong force. The development of the theory, including the introduction and formalization of color charge by physicists such as Oscar W. Greenberg, and Moo-Young Han and Yoichiro Nambu, elaborated on this foundational concept, leading to the QCD we know today, which describes the interactions of quarks and gluons through color charge. Oscar W. Greenberg is often credited with introducing the concept of color as a quantum number in 1964 to resolve the issue raised by the "statistics problem" in quark

models, where the existence of particles like the Δ^{++} (Delta baryon) seemed to violate the Pauli exclusion principle if quarks were considered identical fermions. Greenberg proposed that quarks could possess an additional quantum number, which he later related to color, to allow for the combination of three quarks in the same quantum state without violating the exclusion principle. [9, 10, 11]

1.0.3 QED, renormalization, symmetries and forces

Richard Feynman contributed to Quantum Electrodynamics (QED) through the development of the path integral formulation, which provided a new computational tool for analyzing the behavior of particles at the quantum level [12]. Julian Schwinger's contribution was the formulation of QED in terms of operator field theory, offering a rigorous mathematical framework for predicting particle interactions [13]. Sin-Itiro Tomonaga independently developed a similar formulation to Schwinger's, also focusing on renormalization, which allowed for the removal of infinities from QED calculations, making the theory predictive [14]. Each of these contributions was crucial for the advancement of QED, laying the groundwork for our understanding of the quantum world. Their work led to the Nobel Prize in Physics in 1965. In 1954, Chen Ning Yang and Robert Mills introduced Yang-Mills theory, expanding gauge invariance from electromagnetism (U(1) gauge theory) to include SU(2) and SU(3) groups, relevant for nuclear forces in particle physics [15]. This theory laid the groundwork for later developments in the Standard Model. T' Hooft, in the early 1970s, advanced the field by addressing infinite results in quantum field theories through renormalization, crucial for (QED) and the formulation of Quantum Chromodynamics (QCD) for the strong force. The discovery of asymptotic freedom in non-abelian gauge theories by Gross, Wilczek, and Politzer [16, 17, 18, 19], demonstrating that quark forces weaken at closer distances, was key in this area [20]. These efforts contributed to a unified framework for understanding of all forces.

1.0.4 Heavy quarks, the missing piece of the puzzle

Flavor-Changing Neutral Currents (FCNCs) are processes where a quark changes type without changing the electric charge, predicted to be rare in the Standard Model. Theoretical prediction of the charm quark by Sheldon Glashow, John Iliopoulos, and Luciano Maiani (the GIM mechanism, 1970) explained the suppression of FCNCs [21, 22].The rate of Flavor-Changing Neutral Currents (FCNCs) and its relation to mass or flavor in the Standard Model depends on the mechanism of quark mixing, described by the Cabibbo-Kobayashi-Maskawa (CKM) matrix. This matrix explains how quarks of different generations mix and change flavor during weak interactions, a process that is fundamentally linked to their masses [23]. The suppression of Flavor-Changing Neutral Currents (FCNCs) within the Standard Model primarily originates from the mass differences among quarks and the structure of the Cabibbo-Kobayashi-Maskawa (CKM) matrix. The GIM mechanism, introduced by Glashow, Iliopoulos, and Maiani, demonstrates that FCNC processes are suppressed due to destructive interference between different quark loop contributions in weak decays, a phenomenon that becomes particularly effective when virtual quarks have similar masses [22]. This suppression mechanism is represented by the inclusion of terms in loop calculations that depend on the masses of the virtual quarks, such as :

$$f(m_k) \propto \sum_{i,j} V_{ij} V_{ji}^* \log\left(\frac{m_j^2}{m_i^2}\right) \tag{2}$$

where V_{ij} are elements of the CKM matrix, and m_i and m_j are the masses of the virtual quarks. The introduction of a heavier charm quark allows for significant mass differences that ensure the effective suppression of FCNCs by altering the balance of these loop contributions. The disparity introduced by the charm quark's mass is needed to explain the observed low rates of FCNC processes, as it modifies the loop contributions in a way that prevents their frequent occurrence. This theoretical framework, supported by the CKM matrix's experimental verification and the discovery of the charm quark, underscores the interplay

between quark masses and weak interaction dynamics, providing an explanation for the rare observation of FCNCs.

The J/Ψ ($c\bar{c}$) meson was discovered independently in 1974 by teams led by Burton Richter at SLAC and Samuel Ting at Brookhaven, providing evidence for the charm quark. This discovery was a major discovery, as it confirmed the existence of a fourth quark type. [24, 25]. The D mesons, consisting of D^0 and D^+, were discovered in 1976 through experiments that observed their decay products. These mesons are composed of a charm quark and an up or down antiquark, representing the first observed states of charm hadrons [26]. The discovery of the Λ_c^+ baryon was primarily through its decay modes, which provided clear signatures of its existence. The Λ_c^+, composed of a charm quark (c), an up quark (u), and a down quark (d), was observed in its decay to a proton (p), a kaon (K^-), and a pion (π^+) among other modes. This particular decay mode, $\Lambda_c^+ \to pK^-\pi^+$, was instrumental in the identification of the Λ_c^+ because it exhibited a distinct event topology and invariant mass peak that could be distinguished from background processes [27].

The bottom (or "b") quark was discovered in 1977. The discovery was made in experiments conducted at the Fermi National Accelerator Laboratory (Fermilab), led by physicist Leon Lederman.[28]. The Upsilon meson was the hadron that indicated the existence of the bottom quark. The Upsilon meson $b\bar{b}$) was much heavier than any previously known hadrons. Its mass was about 9.5 GeV/c^2, which was unexpected and could not be explained by any combinations of the known quarks at the time (up, down, strange, and charm). Additionally, the Upsilon meson had a very narrow width (i.e., it was very stable before decaying), which indicated that it was not a composite of any known quarks. The production and decay patterns of the Upsilon meson were also inconsistent with any combinations of the known quarks. The discovery of the B meson occurred in 1980 at Fermilab by the CLEO and CUSB collaborations through the observation of events that indicated the presence of particles with

a bottom quark [29]. These B mesons are mesons containing a bottom (or beauty) quark and either an up or down antiquark, contributing to the understanding of the weak force and CP violation in the Standard Model because this particle is heavy and these types of weak decays can be studied well on them. The first beauty baryon, which contains a bottom quark, was the Λ_b^0 baryon. Its discovery was reported in 1991 by the CERN UA1 collaboration. The Λ_b^0 baryon, composed of a bottom quark, an up quark, and a down quark (bud), was identified through its decay channels, particularly the decay into a J/Ψ meson and a Λ baryon [30].

The top quark itself was discovered in 1995 by two experiments, CDF (Collider Detector at Fermilab) and DØ (DZero), at the Fermi National Accelerator Laboratory (Fermilab) in the United States .The discovery did not involve observing bound states of the top quark with other quarks (such as in mesons or baryons) but rather through direct observation of top quark pairs ($t\bar{t}$) produced in proton-antiproton ($p\bar{p}$) collisions.The top quark's discovery was a monumental achievement in particle physics, confirming the last predicted quark of the Standard Model. The detection of the top quark involved analyzing the products of its decay, primarily into a W boson and a bottom quark ($t \to Wb$). Given the top quark's extremely short lifetime, it decays before it has a chance to hadronize. [31, 32].

1.0.5 Early cosmology and its connection to particle physics

General relativity, formulated by Albert Einstein in 1915, provided the theoretical foundation for understanding the universe's large-scale structure and dynamics [33]. It introduced the concept that the geometry of space and time is influenced by the distribution of mass and energy, leading to the prediction of an expanding or contracting universe. Solutions to Einstein's field equations, notably by Alexander Friedmann [34] and Georges Lemaître [35], suggested an expanding universe, which was empirically supported by Edwin Hubble's

observations of receding galaxies in the 1920s.

$$H^2 = \frac{8\pi G}{3}\rho - \frac{k}{a^2} + \frac{\Lambda}{3} \tag{3}$$

where H is the Hubble parameter, indicating the rate of expansion of the universe, G is the gravitational constant, related to the strength of gravity, ρ is the energy density of the universe, k is the curvature parameter, describing the shape of the universe (open, flat, or closed), a is the scale factor, representing the size of the universe as a function of time, and Λ is the cosmological constant, associated with the energy density of the vacuum of space. This equation is fundamental in the field of cosmology, as it relates the expansion of the universe to its content of matter, energy, and the geometry of space. The early idea about the thermal state of the universe was shaped by the Big Bang theory, which states that the universe began in an extremely hot and dense state which was homogeneous and isotropic (see Figure 3). As the universe expanded, it cooled down, transitioning through various phases. George Gamow, Ralph Alpher, and Robert Herman, developed the theoretical framework leading to the prediction of the cosmic microwave background (CMB) radiation [36]. Fred Hoyle's steady-state cosmological model, which posited a constant-density universe with continuous matter creation, was not successful against the Big Bang theory due to its inability to explain the observed cosmic microwave background radiation and the abundance of light elements. The Cosmic Microwave Background (CMB) represents the moment when photons decoupled from matter, as the universe cooled and expanded, allowing light to travel freely for the first time, effectively making the universe transparent The discovery of the CMB by Arno Penzias and Robert Wilson [37] provided strong empirical support for the Big Bang theory. This confirmed that the early universe was indeed in a hot, dense, and thermal state. Shuryak's research in the 1970s and 1980s played an important role in postulating the Quark-Gluon Plasma (QGP) and exploring its properties and implications for heavy-ion collisions and early universe cosmology [38]. He was among the first to suggest that such a state could

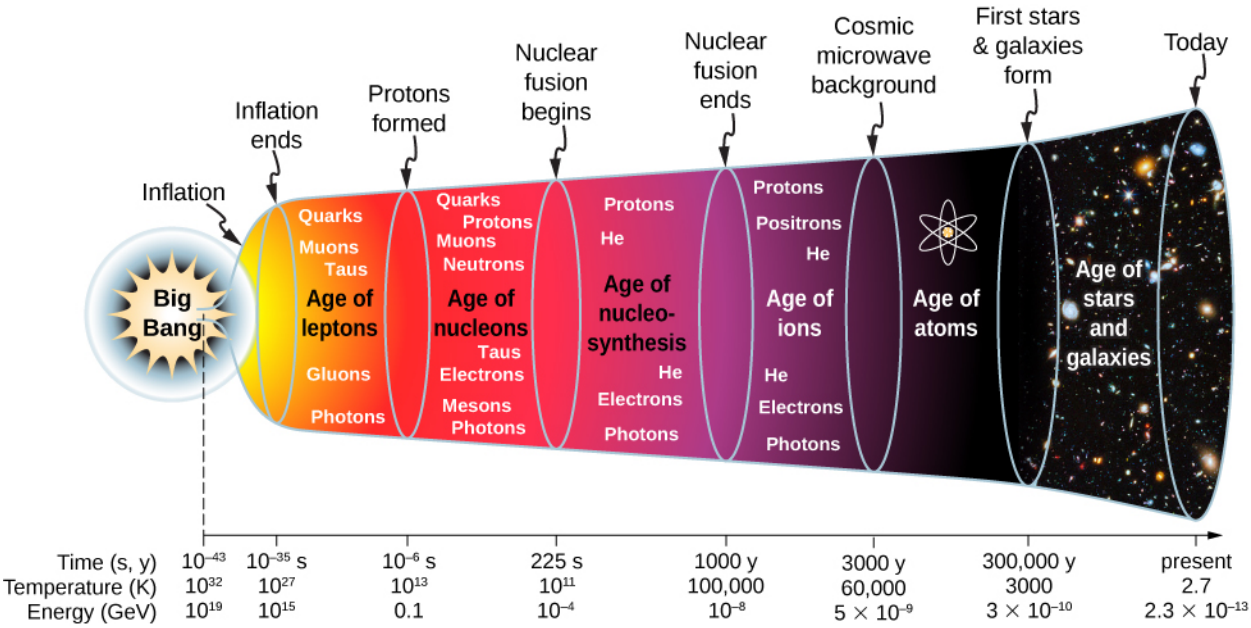

Figure 3: The time line of the universe as it goes through various phases, Image credit: University of Central Florida (UCF)

be created and studied in laboratory conditions through relativistic heavy-ion collisions, providing a direct link between theoretical physics and experimental verification. One of Shuryak's key contributions was developing models that describe how QGP behaves under various conditions, including its thermodynamics, phase transitions, and the role of strong coupling in its dynamics.

1.1 Theory of Quantum Chromodynamics

Quantum Chromodynamics (QCD) is the theoretical framework describing the interactions of quarks and gluons. The mathematical foundation of QCD is well-established; however, its application in predicting experimental outcomes is complicated due to its non-perturbative nature. This problem arises because the transition from the initial state to the final state in QCD processes involves a series of complex interactions. In QCD, quarks possess electric charge, enabling them to engage in electromagnetic interactions mediated by photons. These

interactions result in electromagnetic forces between quarks, albeit with quantum mechanical effects but dominantly the strong interaction is responsible for binding quarks within hadrons. This interaction is mediated by gluons, which, unlike photons, carry a color charge specific to the strong force by its significant strength at short distances but rapid fall beyond the size of a nucleus. Although weak interactions have a less significant role in quark binding compared to the strong force, they are essential for certain particle decay and transformation processes such as flavor change in, for example charm hadron semileptonic decays. The non-perturbative aspects of QCD impose challenges for theoretical predictions of experimental observables. Lattice QCD is a computational approach that allows for the investigation of QCD in the non-perturbative regime, providing insights into hadron structure and the dynamics of quark-gluon interactions. Additionally, effective field theories such as Heavy Quark Effective Theory and Chiral Perturbation Theory offer methods to study aspects of QCD with reduced computational complexity [39].

1.1.1 Experimental evidence for color charges

Particles like the Ω^- [40, 41] are a class of hadrons known as baryons, which are composed of three quarks. The Ω^- is particularly unique because it is made up of three strange quarks. Another similar particle in terms of its composition is the Delta baryon Δ. For example, the Δ^{++} is composed of three up quarks. These particles, like the Ω^-, require the concept of color charge in quarks to adhere to the Pauli Exclusion Principle. The Eightfold way based on their properties such as electric charge, spin, and strangeness is guided by symmetry principles, specifically the $SU(3)$ symmetry in flavor space, which refers to the symmetry under transformations among the three lightest quarks: up, down, and strange. Ω^- particle fits uniquely within this classification scheme. It was predicted based on the patterns and symmetries observed in the hadron spectrum before it was experimentally discovered. According to this scheme, particles are grouped into octets and decuplets based on their quantum numbers. The decuplet is arranged in such a way that the particles' quantum

numbers, including their electric charge and strangeness, increase or decrease along the axes of the diagram. At the time of its prediction, the Ω^- was the only missing member of the baryon decuplet. Its properties, including its mass, electric charge (-1), and a strangeness of -3, were predicted based on its position in the decuplet. The strangeness of -3 indicates that the Ω^- is composed of three strange quarks (sss). This was a direct consequence of the $SU(3)$ symmetry and the organizational principles of the Eightfold Way, which suggested that if up and down quarks could combine in threes to form other baryons, then three strange quarks could also combine to form a new, yet undiscovered baryon. The successful prediction and subsequent discovery of the Ω^- in 1964 was a validation of the Eightfold Way and the quark model that followed. It demonstrated the power of symmetry principles in predicting the existence of particles and their properties without direct observation of the quarks themselves. The resolution of the conflict between the quark model's predictions and the Pauli Exclusion Principle through the introduction of color charge is a fundamental aspect of Quantum Chromodynamics. The concept of color charge was proposed to ensure that baryons, could exist without violating the Pauli Exclusion Principle. This principle states that no two fermions (particles with half-integer spin) can occupy the same quantum state within a quantum system simultaneously. When an electron and positron annihilate at high energies, they can produce either a pair of leptons or a pair of quarks. The probability of producing quarks is enhanced by the fact that quarks come in three colors. The ratio R is defined as:

$$R = \frac{\sigma(e^+e^- \to \text{hadrons})}{\sigma(e^+e^- \to \mu^+\mu^-)} \tag{4}$$

In the naive quark model, ignoring QCD corrections and assuming that all quark flavors are accessible, R would be equal to the sum over all produced quark pairs, each multiplied by a factor of 3 for the three color charges:

$$R = 3\sum_q Q_q^2 \tag{5}$$

where Q_q is the electric charge of the quark q. The experimental observation of R being approximately three times the expected value from just counting quark flavors provided indirect evidence for the three color charges in QCD. This factor of three increase is due to the three possible color charges each quark can carry.

1.1.2 Three jets events

At the PETRA accelerator at DESY in Germany, starting in 1979 (see Figure 4), experiments began to observe events where electron-positron annihilation produced not just two, but three jets. A two-jet event involves the creation of two back-to-back sprays of particles, or jets, resulting from quarks or gluons scattering. These jets are visible as concentrated flows of particles emanating from the collision point. A three-jet event in heavy ion collisions is less common and involves the production of three separate jets, typically from processes involving additional radiation or interactions beyond simple quark-quark scattering. This was a direct indication of the gluon, the carrier of the strong force. Gluons can radiate off quarks in a similar manner to how photons radiate off charged particles. This third jet was interpreted as resulting from the radiation of a gluon by one of the quarks before hadronization (the process by which quarks group together to form hadrons). This means that as a quark or an antiquark emitted a gluon, the gluon itself could materialize into a jet under the right conditions. The presence of three jets in an event suggested a process where a quark-antiquark pair was produced, and one of these particles emitted a gluon, leading to three distinct streams of particles or jets. [42, 43, 44, 45, 46].

1.1.3 QCD lagrangian and SU(3) fundamental symmetry

The problem that QED faced in its early days was that when physicists tried to calculate the probabilities of certain quantum events, such as the scattering of photons by electrons (Compton scattering), they encountered infinities. These infinities arose from the interactions at very short distances and seemed to make the theory non-predictive. Julian Schwinger, Sin-

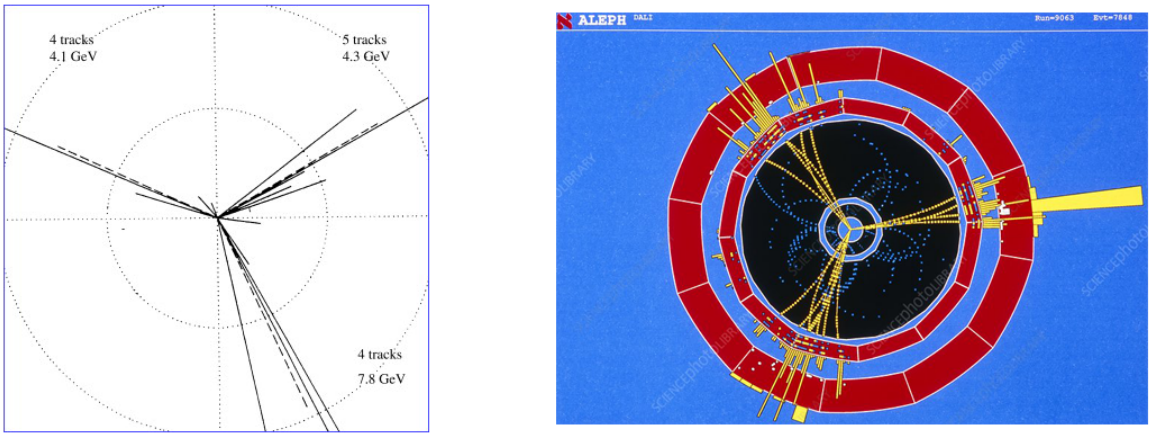

Figure 4: The first image of three jets discovery in 1979 (left), Three-jet Event (right) Detected By Aleph At Cern is a photograph by Cern/science Photo Library

Itiro Tomonaga, and Richard Feynman—each working independently developed methods to systematically cancel these infinities in a process known as renormalization. The idea behind renormalization is that the 'bare' mass and charge of particles, which are the parameters appearing in the equations of QED, are not the same as the 'physical' mass and charge that we measure. The infinities can be absorbed into the bare parameters through a process of redefinition. This redefinition is not arbitrary; it is done in a way that the predictions for observable quantities (like the electron's mass and charge as we measure them) remain finite and well-defined.

The QCD Lagrangian, including perturbative interactions between fermions and gluons, can be expressed as:

$$\mathcal{L}_{\text{QCD}} = -\frac{1}{4}F^a_{\mu\nu}F^{\mu\nu}_a + \sum_f \bar{\psi}_f(i\gamma^\mu D_\mu - m_f)\psi_f \tag{6}$$

The term $F^a_{\mu\nu}$ is the field strength tensor for gluons, describing the color field in QCD, with μ and ν as spacetime indices and a as a color index. The normalization factor $-\frac{1}{4}$ is customary in field theory Lagrangians. The sum $\sum_f$ runs over different quark flavors f, such as up,

down, charm, strange, top, and bottom. The Dirac adjoint of the quark field for flavor f is denoted by $\bar{\psi}_f$, and ψ_f represents the quark field itself for flavor f. The term $i\gamma^\mu D_\mu$ signifies the interaction between quarks and gluons, with γ^μ being the gamma matrices that describe fermions in relativistic quantum field theory, and D_μ is the covariant derivative, which includes perturbative interactions with the gluon field, reflecting the dynamics of quarks and gluons. The mass of the quark of flavor f is represented by m_f.

$$D_\mu = \partial_\mu - ig_s T^a A^a_\mu \tag{7}$$

In this expression, D_μ is the covariant derivative, ∂_μ is the standard partial derivative, ig_s is the strong coupling constant multiplied by the imaginary unit i. T^a are the generators of the SU(3) group in the fundamental representation. The generators T^a of the $SU(3)$ group in the fundamental representation, where a ranges from 1 to 8 (there are only 8 independent generators for $SU(3)$, not 9), are given by the Gell-Mann matrices. These matrices are:

$$T^1 = \frac{1}{2}\begin{pmatrix} 0 & 1 & 0 \\ 1 & 0 & 0 \\ 0 & 0 & 0 \end{pmatrix}, \quad T^2 = \frac{1}{2}\begin{pmatrix} 0 & -i & 0 \\ i & 0 & 0 \\ 0 & 0 & 0 \end{pmatrix}, \quad T^3 = \frac{1}{2}\begin{pmatrix} 1 & 0 & 0 \\ 0 & -1 & 0 \\ 0 & 0 & 0 \end{pmatrix},$$

$$T^4 = \frac{1}{2}\begin{pmatrix} 0 & 0 & 1 \\ 0 & 0 & 0 \\ 1 & 0 & 0 \end{pmatrix}, \quad T^5 = \frac{1}{2}\begin{pmatrix} 0 & 0 & -i \\ 0 & 0 & 0 \\ i & 0 & 0 \end{pmatrix}, \quad T^6 = \frac{1}{2}\begin{pmatrix} 0 & 0 & 0 \\ 0 & 0 & 1 \\ 0 & 1 & 0 \end{pmatrix},$$

$$T^7 = \frac{1}{2}\begin{pmatrix} 0 & 0 & 0 \\ 0 & 0 & -i \\ 0 & i & 0 \end{pmatrix}, \quad T^8 = \frac{1}{2\sqrt{3}}\begin{pmatrix} 1 & 0 & 0 \\ 0 & 1 & 0 \\ 0 & 0 & -2 \end{pmatrix}.$$

Each T^a matrix is a representation of the algebra of the $SU(3)$ group, which underlies the color charge. These matrices are used in the definition of the covariant derivative D_μ in the

QCD Lagrangian to incorporate the interactions between quarks and gluons. A^a_μ are the gluon fields. The gluon field strength tensor $F^a_{\mu\nu}$ is defined as:

$$F^a_{\mu\nu} = \partial_\mu A^a_\nu - \partial_\nu A^a_\mu + g_s f_{abc} A^b_\mu A^c_\nu \tag{8}$$

Under an SU(3) gauge transformation, A^a_μ transforms in a way that leaves $F^a_{\mu\nu}$ invariant. The structure constants f_{abc} of SU(3) ensure that the non-Abelian nature of the group is taken into account.The quark fields ψ_f transform as:

$$\psi_f \to U\psi_f$$

where U is an SU(3) gauge transformation matrix. Since $\bar{\psi}_f$ is the Dirac adjoint, it transforms as:

$$\bar{\psi}_f \to \bar{\psi}_f U^\dagger$$

The covariant derivative in the presence of gluon fields is given by: $D_\mu = \partial_\mu - ig_s T^a A^a_\mu$. Under SU(3) transformations, D_μ transforms in a way that leaves the combination $\bar{\psi}_f(i\gamma_\mu D_\mu - m_f)\psi_f$ invariant. This is to maintain gauge invariance. This Lagrangian containing bare charges and bare masses is able to calculate the tree diagram in first order and any other order.

1.1.4 Wilson's Renormalization Group

Wilson's Renormalization Group (RG) equation describes how physical systems change as we zoom in or out in terms of energy scales.[47]. The concept proposed by Kenneth Wilson refers to how the behavior of a physical system evolves as we examine it at different energy scales, emphasizing that the effective theories at each scale should be independent of an energy cutoff, ensuring that observables like cross sections remain consistent and unaffected as we "zoom out" or vary the energy scale. The equation consists of three main components: the rate of change of the energy scale (μ), the beta function ($\beta(\alpha_s)$) describing how coupling constants

evolve with μ, and the anomalous dimension ($\gamma(\alpha_s)$) characterizing how fields rescale. When this equation is satisfied, it signifies scale invariance, meaning that the system's behavior remains unchanged under rescaling. Fixed points of the equation, [48] where $\beta(\alpha_s) = 0$, indicate situations where the system's behavior is particularly stable or universal. In many cases, the Renormalization Group equations take the form of Wilson's RG equation. It describes how an effective action (or Hamiltonian) changes under rescaling. In one dimension, the equation takes the form:

$$(\mu\frac{d}{d\mu} + \beta(\alpha_s)\frac{d}{d\alpha_s} + \gamma(\alpha_s))S(\mu) = 0 \tag{9}$$

Here, $S(\mu)$ represents an effective action, $\beta(\alpha_s)$ is the beta function, and $\gamma(\alpha_s)$ is an anomalous dimension related to the rescaling of fields. The RG equation for a coupling constant $\alpha(Q)$ is given by:

$$\frac{d\alpha(Q)}{d\log Q} = \beta(\alpha) \tag{10}$$

In this equation, $\beta(\alpha)$ is the beta function. It describes how the coupling constant α evolves with energy. Typically, $\beta(\alpha)$ is expressed as a power series in α:

$$\beta(\alpha) = -b_0\alpha^2 - b_1\alpha^3 - b_2\alpha^4 - \dots \tag{11}$$

Here, $b_0, b_1, b_2, \dots$ are coefficients. $\frac{d\alpha}{d\log Q} = \beta\alpha^2$, is an approximation of the full RG equation. This simplified version assumes that the higher-order terms in the beta function (like $b_1\alpha^3, b_2\alpha^4, \dots$) are negligible compared to the leading term $b_0\alpha^2$. Therefore, we approximate $\beta(\alpha)$ as $\beta\alpha^2$ where β here represents the coefficient b_0.

1.1.5 QED vs QCD renormalization

In QED, the running of the electric charge (or more accurately, the running of the fine structure constant, α) with the energy scale (or momentum transfer) Q is given by [18]:

$$\frac{d\alpha}{d\log Q} = \beta\alpha^2 \tag{12}$$

where β is positive for QED. Its effective charge increases. For QED, at one-loop order, the beta function is given by:

$$\beta(\alpha) = \frac{2}{3\pi}\alpha^2\left(\sum_f Q_f^2\right) + O(\alpha^3) \tag{13}$$

where Q_f is the electric charge of the fermion in the loop, in units of the electron charge, and the sum is over all fermions f that are energetically accessible at the scale μ. This expression shows that the beta function is proportional to α^2, making it inherently positive because α (the fine-structure constant) and Q_f^2 are always positive.

In QCD, the behavior is more complicated due to the self-interactions of the gluons. The running of the strong coupling constant α_s is described by:

$$\frac{d\alpha_s}{d\log Q} = \beta_0\alpha_s^2 \tag{14}$$

with

$$\beta_0 = \frac{11}{3}C_A - \frac{2}{3}n_f \tag{15}$$

Here, C_A is the Casimir invariant of the adjoint representation, which equals 3 for SU(3) (the gauge group of QCD), and n_f is the number of active quark flavors at the energy scale Q. As long as $n_f < 16$, β_0 is negative. This means that α_s decreases as Q increases, and vice versa. The key factor in the formula above is the $\frac{11}{3}C_A$ term, which arises due to the

gluon-gluon interactions. The $-\frac{2}{3}n_f$ term arises from quark-antiquark pair creation, analogous to the electron-positron pairs in QED, which would indeed lead to a screening effect if taken alone. However, the gluon contribution dominates, leading to the anti-screening behavior. To understand this in a semi-qualitative manner, when a quark emits a gluon, the gluon can either: Interact with other quarks (analogous to photon-electron interactions in QED) — this gives the $-\frac{2}{3}n_f$ term. Interact with other gluons — this is unique to QCD and gives the $\frac{11}{3}C_A$ term.

The anti-screening is similar to the behavior observed in magnetic materials. In QCD, the self-interaction of gluons around a quark creates a viscous cloud that effectively enhances the color charge of the quark at larger distances. This gluon-gluon interaction is a fundamental aspect of the strong force, contributing to the confinement of quarks and gluons within hadrons. As the distance from a quark increases, the strong force does not diminish as it would under a purely Coulombic potential; instead, the presence of additional gluons in the cloud increases the effective color charge, a property known as anti-screening. This mechanism in QCD is similar to the behavior of magnetic materials in an external magnetic field. Ferromagnetic materials, for instance, enhance the external magnetic field within their domain due to the alignment of magnetic moments of atoms. This alignment leads to a net magnetization in the direction of the applied field, thereby amplifying the magnetic field inside the material. The process, driven by the intrinsic spin of electrons and the exchange interaction among atoms, mirrors the anti-screening effect in QCD, where the interaction among gluons leads to an enhancement of the strong force with increasing distance from the quark. In contrast, dielectric materials exhibit a screening effect when subjected to an external electric field. The electric field induces dipoles within the material that align in a way to reduce the field's strength inside the material. This polarization effect screens the external electric field, analogous to the screening of electric charges in electrodynamics but in contrast to the anti-screening observed in QCD and the enhancement effect in magnetic materials (see

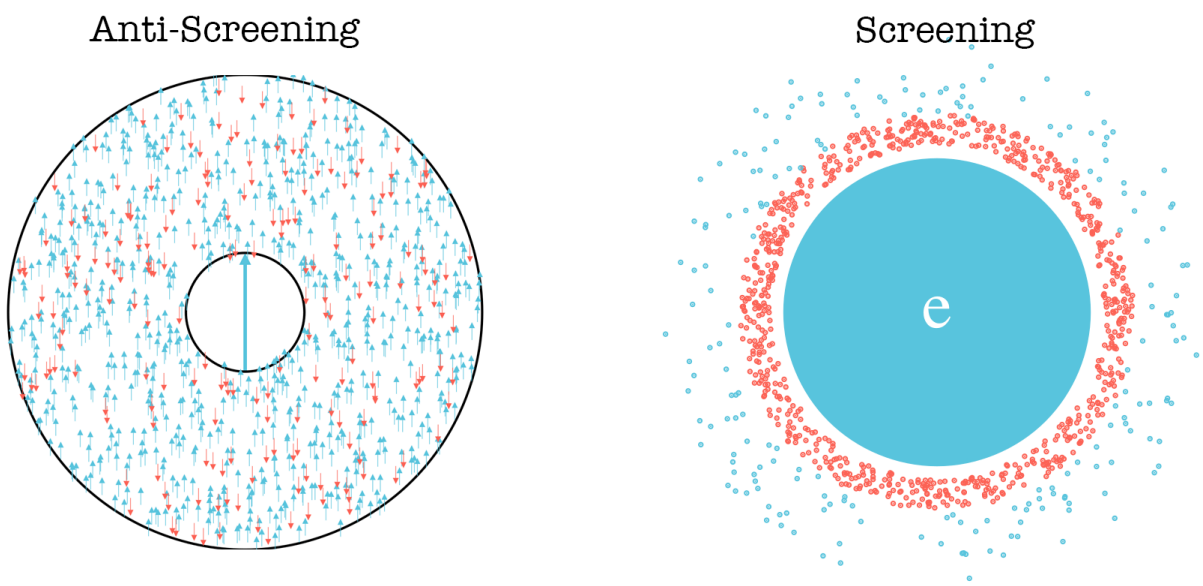

Figure 5: Magnetic anti-screening effect (left) where the effective magnetic moment of the system is enhanced by aligning with the magnet in the center; electrical charge screening effect (right), where the effective electric charge is reduced because the vacuum acts like a dielectric.

Figure 5)

1.2 Confinement and chiral symmetry breaking

Confinement refers to the phenomenon that quarks and gluons cannot be isolated as individual particles in free space under normal conditions. Instead, they are perpetually bound together within composite particles. This property of QCD emerges from the behavior of the strong force, which is mediated by gluons and acts between particles carrying color charge. Confinement remains one of the most challenging puzzles in theoretical physics, primarily due to the non-perturbative nature of QCD at low energies or long distances. The non-perturbative regime is where the strength of the strong force becomes so significant that traditional perturbative techniques, which involve expanding the interactions in a series and considering them term by term, are no longer applicable or effective. This is the regime where confinement occurs, and understanding it requires methods that can deal with the full

complexity of QCD without relying on perturbation theory.

The theoretical framework of confinement encompasses a broad spectrum of phenomena. At its foundation lies the concept of color neutrality, necessitating that observable hadron such as protons and neutrons appear colorless. This condition is met by quarks forming color-singlet states, effectively canceling out their color charges to render the strong force's influence impossible to perceive beyond the particle's boundaries. Flux tube formation introduces a geometrical perspective to confinement, where the gluon field connecting quarks is visualized as tubular structures confining the force. This results in a potential energy that scales linearly with the distance between quarks, symbolic of confinement and hindering the isolation of single quarks. Alongside, chiral symmetry breaking addresses the mass formation mechanism in hadrons, a process where the QCD vacuum imparts masses to inherently massless quarks. This spontaneous breaking of symmetry is important for the mass gap between the vacuum and observable hadrons, firmly holding quarks within bound states and the examination of gluon condensation and the vacuum's topological features, including effects from instantons and monopoles, enrich our understanding of vacuum dynamics. The presence of virtual quark-antiquark pairs, or sea quarks, influences the strong force across different energy scales, affecting the behavior of valence quarks within hadrons. Moreover, phase transition phenomena at extreme conditions, such as those in heavy-ion collisions and possibly within neutron stars, highlight the QCD phase diagram's complexity, revealing scenarios where quarks may briefly escape confinement to form a quark-gluon plasma. These elements collectively contribute to a multi perspective of confinement.

1.2.1 Color neutrality

The sum of net color charges of hadrons including mesons and baryons is a color singlet. Hence, both the baryon and meson color singlet states remain unchanged under SU(3)

transformations, verifying their color neutrality. For baryons, which consist of three quarks, the color singlet configuration ensures that the combined color charges of the quarks result in a net color-neutral state. Using the typical notation of red (r), green (g), and blue (b) for quark colors:

$$|\text{baryon}\rangle = \epsilon_{ijk} q_i q_j q_k \tag{16}$$

Here, the indices i, j, k iterate over the three colors, and ϵ_{ijk} is the Levi-Civita symbol ensuring the antisymmetric combination of colors.

$$|\text{baryon}\rangle = q_r q_g q_b - q_r q_b q_g + q_g q_b q_r - q_g q_r q_b + q_b q_r q_g - q_b q_g q_r \tag{17}$$

The above expression ensures that every color combination is considered. This means that a baryon effectively combines all three primary color charges (red, green, and blue) to produce a color-neutral (or 'white') state. Mesons are composite particles consisting of a quark and an antiquark. The strong interaction requires that the combined color charges of the quark and the antiquark in a meson result in a net color-neutral state. This color-neutrality is referred to as a "color singlet." For mesons, the color singlet configuration is achieved by pairing a quark of a given color with an antiquark of the corresponding anti-color. If we utilize the conventional notation of red (r), green (g), blue (b) for quark colors and anti-red ($\bar{r}$), anti-green ($\bar{g}$), and anti-blue ($\bar{b}$) for antiquark colors, the color singlet configuration for mesons can be represented as:

$$|\text{meson}\rangle = \delta^i_j q_i \bar{q}^j \tag{18}$$

Here, the indices i and j iterate over the three colors (or anti-colors), and δ^i_j is the Kronecker delta ensuring the correct pairing of color with its anti-color. Expanding this expression, we get:

$$|\text{meson}\rangle = q_r\bar{q}^r + q_g\bar{q}^g + q_b\bar{q}^b \tag{19}$$

1.2.2 QCD vacuum behaviour

The confinement can be viewed from an alternative perspective, focusing on the non-trivial behavior of the vacuum in QCD, where an instantaneous symmetry breaking leads to mass generation as the system deviates from maintaining chiral symmetry. In this model, the explanation for hadronization does not require the quark and gluon content; instead, it is explained by how massless hadrons become massive through the acquisition of mass from the QCD vacuum [49]. The QCD vacuum isn't "empty" in the naive sense (see Figure 6, left). It is a complex state with rich structure. This vacuum can be thought of as a "sea" of quark-antiquark pairs and gluon fields. There are non-trivial field configurations called instantons and other topological objects in the vacuum. The words "trivial" and "non-trivial" topology of the vacuum refer to the structure and properties of the vacuum state in these theories. A "trivial" topology implies a vacuum state that is simple, homogeneous, and without any interesting structure or fluctuations. This means the vacuum does not contain any fields or particles, and all quantum numbers are zero. On the other hand, a "non-trivial" topology indicates a vacuum that has complex structures or configurations, such as topological defects, solitons, or instantons. These features can have significant implications for the properties of the vacuum, including the possibility of vacuum polarization, where the vacuum behaves as if it were filled with virtual particles and antiparticles. In QCD, a non-trivial vacuum topology is crucial for understanding phenomena such as color confinement and the breaking of chiral symmetry, leading to the generation of mass for hadrons in the absence of explicit mass terms in the Lagrangian [50][51][52].

Chiral symmetry in quantum field theory refers to the invariance of a system under separate

transformations of its left-handed and right-handed fermion components. This this symmetry implies that the physics should be invariant if the left-handed and right-handed quarks are transformed independently, which is strictly true for massless quarks. The QCD Lagrangian with chiral symmetry, particularly for massless quarks, can be expressed as:

$$\mathcal{L}_{QCD} = \bar{\psi}_L i\gamma^\mu D_\mu \psi_L + \bar{\psi}_R i\gamma^\mu D_\mu \psi_R - \frac{1}{4} G^a_{\mu\nu} G^{\mu\nu}_a \tag{20}$$

However, this symmetry is not absolute; it is explicitly broken by quark masses and spontaneously broken by the QCD vacuum, leading to massive particles and the emergence of pseudo-Goldstone bosons (see Figure 6, right), which are key to understanding the mass spectrum of hadrons.

The vacuum expectation value of the quark bilinear $\langle \bar{q}q \rangle$ is non-zero, which indicates the spontaneous breaking of chiral symmetry. The direct relationship between chiral symmetry breaking and confinement, however, remains to be fully elucidated. Confinement refers to the final state of hadrons, characterized by their mass and color neutrality. Therefore, any process that leads to the generation of mass and ensures color neutrality can be considered part of the confinement mechanism. This explains the use of the term "hadronization" to describe the complex processes involved in the confinement of quarks and gluons

The linear sigma model, also known as the pion-sigma model, serves as a theoretical framework for describing the spontaneous breaking of chiral symmetry, a key aspect in the low-energy domain of QCD. This model incorporates a scalar field, σ, representing the scalar quark-antiquark bound state, alongside a three-component pseudoscalar field, $\vec{\pi} = (\pi_1, \pi_2, \pi_3)$, which corresponds to the pions. The scalar nature of the σ field implies it remains invariant under parity transformations, reflecting its role in denoting the spontaneous chiral symmetry breaking through its non-zero vacuum expectation value (VEV). Conversely, the pions are

pseudoscalar, changing sign under parity transformations, aligning with their empirical pseudoscalar characteristics. As Goldstone bosons resulting from chiral symmetry breaking (assuming massless quarks), their pseudoscalar nature arises from the axial component of the broken chiral symmetries. The inclusion of one scalar and three pseudoscalar fields fulfills the minimum criteria for depicting the spontaneous breaking of $SU(2)_L \times SU(2)_R$ chiral symmetry within an effective field theory, allowing for the representation of the observed three pions as Goldstone bosons and the σ meson as the scalar quark-antiquark bound state. These choices are grounded in QCD symmetries and the physical attributes of the mesons. The model's Lagrangian density is given by:

$$\mathcal{L} = \frac{1}{2}\partial_\mu \sigma \partial^\mu \sigma + \frac{1}{2}\partial_\mu \vec{\pi} \cdot \partial^\mu \vec{\pi} - U(\sigma, \vec{\pi}) \tag{21}$$

where $U(\sigma, \vec{\pi})$ represents the potential responsible for spontaneous symmetry breaking:

$$U(\sigma, \vec{\pi}) = \frac{\lambda^2}{4}\left(\sigma^2 + \vec{\pi} \cdot \vec{\pi} - v^2\right)^2 \tag{22}$$

In this expression, λ denotes a coupling constant, and v signifies a nonzero value that determines the spontaneous symmetry breaking scale. The vacuum state is characterized by field values that minimize the potential U, implying: $\sigma^2 + \vec{\pi} \cdot \vec{\pi} = v^2$. This setup underscores the mechanism of spontaneous chiral symmetry breaking and its implications for meson mass generation and the theoretical underpinnings of QCD. [53][54][55].

1.2.3 Confinement force

The notion of force manifests as a macroscopic effect under conditions where the number of photons is large and the temporal scale surpasses the exchange frequency of these photons. Force is essentially described as the gradient of energy with respect to length. This framework for understanding classical force holds when the energy stored within a system is trivial relative to the rest mass of the real particles contained within that volume. An example is a

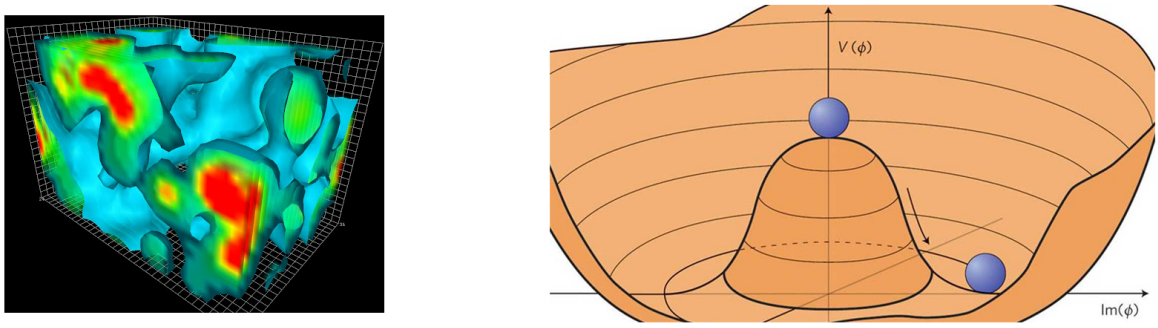

Figure 6: The QCD vacuum is not empty but exhibits a complex structure (left, Image credit Derek Leinweber). The phenomenon of spontaneous symmetry breaking is effectively modeled using the Mexican hat potential, demonstrating how symmetries are dynamically broken in quantum field theories (right).

hydrogen atom, where the stored energy is the ionization energy of the electron, approximately 13 eV, while the rest mass of the electron is 0.5 MeV, and the proton's mass is about 1GeV. This disparity stems from the characteristics of the QED coupling constant. Transitioning from QED to QCD, the dependency of energy on the coupling constant markedly intensifies. In scenarios where the coupling strength of the strong force is considerable, the energy associated with gluon exchange within a volume becomes comparable to the rest mass of both light and heavy flavor quarks, despite initially focusing on light quarks. This shift underscores the significant impact of the strong coupling constant in QCD on energy storage relative to particle rest masses. The running of the strong coupling constant α_s as a function of the momentum transfer squared Q^2 at low orders is given by:

$$\alpha_s(Q^2) = \frac{\alpha_s(\mu^2)}{1 + \frac{\alpha_s(\mu^2)}{12\pi}\beta_0 \ln\left(\frac{Q^2}{\mu^2}\right)} \tag{23}$$

Here, μ^2 is the renormalization scale and β_0 represents the leading order beta function coefficient in the renormalization group equation of QCD. In QCD, the propagator for a gluon in the Feynman gauge, ignoring the effects of quark loops for simplicity, is given by:

$$D_{\mu\nu}(q) = \frac{-ig_{\mu\nu}}{q^2 + i\epsilon} \tag{24}$$

From the gluon propagator, the potential between two quarks in position space can be derived via the Fourier transform of the gluon propagator. This relationship is expressed as:

$$V(r) \propto \int \frac{d^3q}{(2\pi)^3} e^{i\mathbf{q}\cdot\mathbf{r}} D_{00}(q) \tag{25}$$

One key aspect of the quark-quark potential in QCD is confinement. At large distances between quarks, the potential demonstrates a linear rise, indicative of a confining force. This potential can be modeled as:

$$V(r) = -\frac{\alpha_s}{r} + \sigma r + \text{const.} \tag{26}$$

Where the term $\frac{\alpha_s}{r}$ represents the Coulombic interaction, σ is the string tension or energy density of flux tube that describes the strength of the linear confinement, and the "const." term is an additive constant which represents the mean field average energy stored in a flux tube.

1.2.4 Flux tubes

Schwinger mechanism [56] for particle production in a strong electric field is a foundational quantum field theoretic description of how a strong field can induce particle-antiparticle pairs from the vacuum. Julian Schwinger, a Nobel laureate, first derived this result in Quantum Electrodynamics (QED). In quantum field theory, the vacuum isn't a truly "empty" state. It is filled with fluctuations, where particle-antiparticle pairs momentarily pop into existence and then annihilate. The Schwinger mechanism involves the transition of virtual electron-positron pairs (off-shell) to real electron-positron pairs (on-shell) due to the presence of a strong electric field. The electric field provides the necessary energy to allow this transition to occur, effectively "promoting" a virtual pair to become real. The rate of electron-positron pair

production per unit volume in a strong electric field can be given by,

$$\frac{dN}{d^3x\,dt} = \frac{e^2E^2}{(2\pi)^3}\exp\left(-\frac{\pi m^2}{eE}\right) \tag{27}$$

The mass of the electron (or any charged particle) is needed for the formula. The exponential suppression factor in the Schwinger formula relies on the mass m. If the electron were massless, this term would not behave in the same way, making the formula invalid in that scenario. The Schwinger mechanism predicts particle production specifically due to quantum tunneling effects, which are sensitive to the particle's mass. Although the concept of particle production in strong fields still exists, the mechanisms and relevant equations would be different from those derived by Schwinger for massive electrons. The electric field itself does not directly provide energy to the particles in the same way a particle collider might impart kinetic energy to particles. Instead, it changes the conditions of the vacuum so that the energy barrier for particle creation is effectively lowered, enabling the virtual particles to tunnel through this barrier and become real.

Applying the Schwinger mechanism to QCD could be feasible, but it is important to recognize the significant differences in scale between QED and QCD. In the realm of QCD, we discuss an external chromofield that induces particle production, though this field operates under principles similar to the electromagnetic field known in QED. To make sense of quark-antiquark pair production in the presence of a strong chromofield, we rely on an approximation termed "Abelian dominance." This approach suggests splitting the chromofield into two segments: a coherent field and a non-coherent part. The coherent field can be likened to a classical electromagnetic wave, essentially representing the mean field approximation of the gluon field created when two nuclei pass through each other. This method allows us to apply classical electromagnetic analogies to the QCD setting, aiding in the calculation of quark-antiquark pair production based on chromofield characteristics. The non-coherent segment, though not fully

detailed, accounts for the more complex and fluctuating aspects of the chromofield, deviating from the simplicity of the mean field approximation. This includes the unique quantum behaviors and interactions within QCD, such as gluon self-interactions and the strong force's non-Abelian qualities. The process of diagonalization plays a critical role in isolating the Abelian (commutative) components from the non-Abelian gauge fields. This diagonalization allows for a simplification where the complex non-Abelian dynamics can be approximated or analyzed through a more tractable Abelian framework. By diagonalizing the gauge field matrices, the dynamics of the gauge fields can be simplified to those resembling Abelian gauge theories like Quantum Electrodynamics (QED). This simplification occurs because, in the diagonalized form, the gauge fields' behavior is governed by the linear superposition principle, without the complications of the non-Abelian self-interactions represented by the off-diagonal elements. The diagonalization and subsequent focus on the coherent field make certain analytical and numerical studies more feasible.

After diagonalization, the gauge fields can be approximated by their diagonal components, simplifying the field strength tensor to:

$$F^a_{\mu\nu} \approx \partial_\mu A^a_\nu - \partial_\nu A^a_\mu \tag{28}$$

for the a corresponding to the diagonal generators. This approximation neglects the gluon self-interaction terms ($gf^{abc}A^b_\mu A^c_\nu$), leading to a linear, Abelian-like form that resembles electromagnetism. The dynamics described by these simplified fields are governed by equations analogous to Maxwell's equations, facilitating analysis using familiar electromagnetic concepts. The Abelian dominance approximation involves focusing on the diagonal (or Abelian) components of the gauge fields, suggesting that they dominate the confinement mechanism. The chromofield is often decomposed into coherent and non-coherent parts:

$$\mathbf{A}_\mu = \mathbf{A}_\mu^{\text{coh}} + \mathbf{A}_\mu^{\text{non-coh}} \tag{29}$$

Where $\mathbf{A}_\mu^{\text{coh}}$ represents the long-range, confining components. $\mathbf{A}_\mu^{\text{non-coh}}$ signifies the short-range, perturbative parts. The Abelian dominance emphasizes that confinement is largely due to the coherent component of the chromofield. The Color Glass Condensate (CGC) model is a paradigm that explains particle production based on Schwinger mechanism, utilizing flux tubes that adhere to Abelian dominance. At high energy scales, the gluon densities reach a threshold that triggers nonlinear effects, leading to a saturated state characterized by a balance between the proliferation and recombination of gluons. This state is defined by a specific momentum scale, denoted as Q_s, which signifies the juncture at which the growth of gluon distribution becomes regulated. The Color Glass Condensate (CGC) model uses classical Yang-Mills equations to describe the evolution of dense gluon fields, making it an effective tool for exploring the dynamics of gluons at high densities. This framework is particularly useful for studying parton distribution functions at small-x values, where 'x' is the fraction of a proton's momentum carried by its constituent partons. The CGC model plays a crucial role in understanding a range of phenomena, from the initial conditions in heavy-ion collisions to partonic interactions in deep inelastic scattering experiments [57][58][59]. It provides insights into gluon density saturation, explaining observed multiplicity distributions and transverse momentum patterns in experimental data from RHIC and LHC. Additionally, the CGC model accounts for geometric scaling and azimuthal anisotropies like elliptic flow, reflecting the impact of high gluon densities on particle behavior in collisions [60][61][62]. These findings affirm the CGC's ability to capture key aspects of gluon-dominated processes in quantum chromodynamics (see Figure 7).

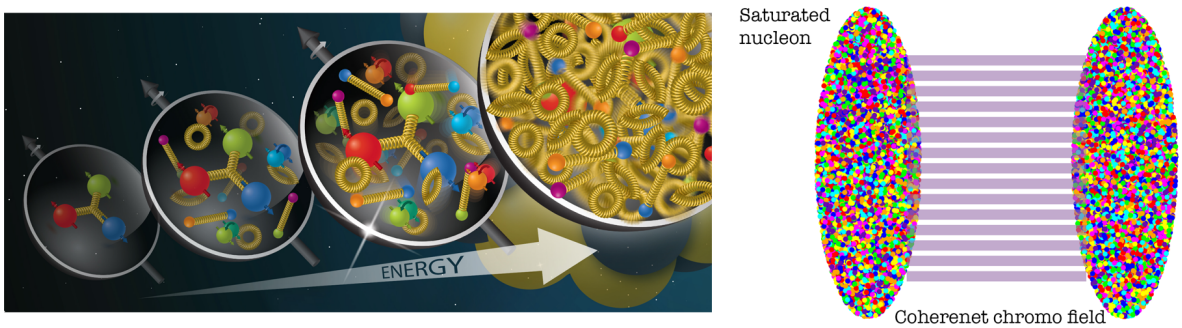

Figure 7: The saturation of protons scales with the energy used to probe them, a focus of research by the EPIC Collaboration, which aims to investigate proton structure at low x and the saturation scale (left). Credit: EPIC Collaboration. The formation of flux tubes after two nucleons pass each other is depicted, highlighting that the chromo field comprises a coherent mean field background augmented by quantum corrections (right)

1.3 Space-time evolution of heavy ion collisions

Space-time evolution of heavy ion collisions refers to the temporal dynamics from the initial system to the final state measured. Ultimately, the detector measures the charged tracks and charged particles comming from the collision area. The space-time evolution of heavy ion collisions depends on the type of system involved. For example, Pb-Pb collisions are considered large systems where the formation of quark-gluon plasma is notably enhanced. Quark-gluon plasma is a state of matter where color charge can diffuse. The consequences of color diffusion in heavy ion collisions manifest through jet quenching, where partons lose energy interacting with the medium, elliptic flow indicating momentum anisotropy due to initial spatial anisotropy and color diffusion, and color screening, which weakens the color force over distance, affecting quarkonia states. Strangeness enhancement in heavy ion collisions involves the increased production of particles with strange quark content. For example, kaons (K^+) are composed of up (u) or down (d) quarks paired with a strange ($\bar{s}$) quark, making them $K^+(u\bar{s})$ or $K^0(d\bar{s})$. Lambda (Λ) baryons consist of one strange quark along with up and down quarks (uds), and Xi (Ξ) baryons contain two strange quarks and either an up or down quark (uss or dss). Pions (π), while not containing strange quarks, serve as a baseline for particle production comparisons. The ALICE experiment at the LHC has provided

significant insights into strangeness enhancement, supporting the existence of quark-gluon plasma [63]. This phenomenon illustrates the deconfined state's ability to produce strange quarks more freely compared to hadronic states, highlighting the unique conditions present in heavy ion collisions. The argument of whether proton-proton collisions are able to create quark-gluon plasma is the subject of investigation in this thesis. If such a state of matter is formed, it has a smaller effect compared to what we see with respect to Pb-Pb collisions. This is because the lifetime of such a produced fireball is shorter and the multiplicity of the system is also smaller. This makes it harder to define local equilibrium, and the system can be mostly seen as out of equilibrium. The proton-proton collisions serve as a fundamental baseline for measurements in Pb-Pb collisions. It may seem that electron-positron (e+e-) collisions could act as a baseline for proton-proton collisions; however, it is crucial to consider that e+e- collisions are not as energetic due to the significant mass difference. Electrons and positrons are approximately 2000 times lighter than protons, and accelerating them to energies comparable to those in proton-proton collisions is challenging due to bremsstrahlung radiation. This phenomenon limits the energy electrons and positrons can achieve without losing a substantial amount through radiation, thus impacting their suitability as a direct baseline for proton-proton collisions.

In general the heavy ion collision can be factorized into a time evolution associate with different phases (see Figure 8 and 9). In the next section, we are going to discuss the phase transition in a broader context. In general, phase is a term used to describe an era where certain types of physics can be applied. Phase is associated with thermal equilibrium, and the idea is that the universe has evolved in different stages. A phase transition refers to the transformation of a system from one state of matter to another, driven by changes in physical conditions such as temperature or pressure. These transitions are critical for understanding various phenomena in the universe, from the formation of early cosmic structures to the behavior of matter under extreme conditions. An important aspect of phase transitions is

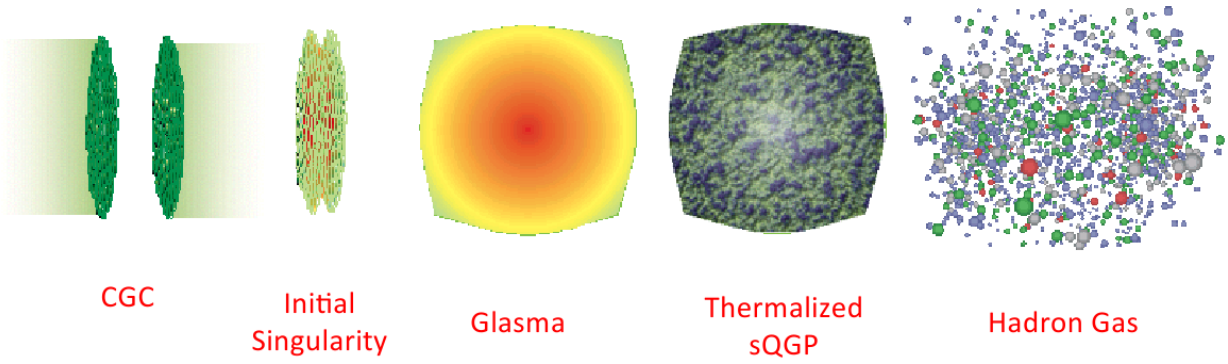

Figure 8: Evolution of heavy ion collisions, image credit Larry McLerran's

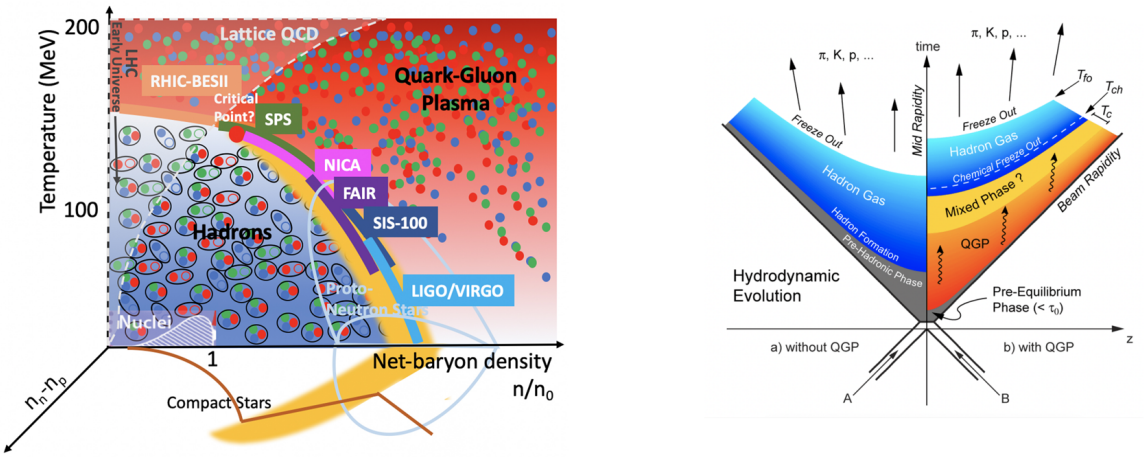

Figure 9: QCD phase diagram (left, Image credit Claudia Ratti [65, 66]), Surfaces of heavy ion collisions, with and without the formation of Quark Gluon Plasma (right, Image credit Shuryak)

the concept of symmetry breaking, where the symmetric state of a system changes to a state with lower symmetry due to changes in external conditions [64]. This concept is pivotal in the theory of the early universe, explaining how different forces and particles emerged from a unified state as the universe cooled down.

1.3.1 Phase transitions

In physics, thermodynamics is a branch that deals with the macroscopic emergent properties of systems, which can be described using the concepts of heat and entropy. Thermodynamics has a long history, dating back to the eighteenth century when heat engines began playing a crucial role in industrialization and the transformation to the automation of processes.

When thermodynamics was formulated in the mid-19th century, the modern understanding of molecules and atoms was not known, which means the actual strength of thermodynamics is that it does not have to deal with the microscopic variables of the systems. The foundational laws of thermodynamics establish the principles that govern energy exchange and the directionality of processes. The zeroth law of thermodynamics introduces the concept of temperature as a fundamental property that equilibrates between bodies in thermal contact [67]. The first law, also known as the law of energy conservation, formalizes the idea that energy cannot be created or destroyed, only transformed or transferred [68]. The second law introduces the concept of entropy, providing a direction to thermodynamic processes and setting limits on energy conversion efficiency [69]. Finally, the third law of thermodynamics states that as the temperature approaches absolute zero, the entropy of a perfect crystal approaches a constant minimum [70]. These principles have profound implications not only in physics but also in chemistry, engineering, and biology, demonstrating the universality of thermodynamic laws across different scales and systems. The development of statistical mechanics in the late 19th and early 20th centuries further bridged the gap between macroscopic thermodynamic behavior and microscopic physical laws, providing a molecular interpretation of thermodynamic quantities such as temperature and entropy [71]. Thermodynamics typically uses temperature, pressure, and volume to define the state of a system. The connection between thermodynamics and microscopic degress of freedom was done through the invention of statistical mechanics where the partition function of a system can be calculated using the microscopic degrees of freedom. This partition function allows us to connect macroscopic variables, such as energy and entropy from counting and integrating over a range of microscopic degrees of freedom. Phase transitions in thermodynamics refer to the change of a substance from one state of matter (phase) to another, such as from solid to liquid or liquid to gas. Each phase, whether solid, liquid, or gas, is characterized by distinct physical properties. The transition between these states involves changes in energy and physical properties under varying conditions of temperature and pressure. Phase transitions

in thermodynamics are categorized into different orders, primarily first and second order, based on their characteristics and the nature of the changes they involve. The Landau theory of phase transitions is a theoretical framework that explains the behavior of physical systems as they undergo phase transitions, particularly emphasizing the concept of symmetry breaking. The core idea revolves around an order parameter that characterizes the different phases of the system. The Landau free energy can be expanded in terms of this order parameter, ϕ, near the phase transition point, typically expressed as:

$$F(\phi) = F_0 + a\phi^2 + b\phi^4 + \cdots \tag{30}$$

$F(\phi)$ represents the Landau free energy, F_0 is a reference free energy, and a and b are coefficients, where b is generally positive to ensure the stability of the system. The coefficient a can change sign as the temperature varies, leading to a phase transition. At high temperatures, a is positive, and the minimum energy state is $\phi = 0$, corresponding to a symmetric phase. At low temperatures, a becomes negative, and the system minimizes its energy with a nonzero value of ϕ, indicating a phase of broken symmetry. Another crucial aspect is the emergence of long-range order as the system undergoes a phase transition, which can be described by the correlation function:

$$G(r) = \langle \phi(0)\phi(r) \rangle \tag{31}$$

This function describes how the order parameter correlations decay with distance. In the symmetry-broken phase, these correlations extend over long distances, indicating the emergence of long-range order. The significance of Landau's theory lies in its universal approach to describing phase transitions and symmetry breaking, providing a fundamental understanding that applies to various physical systems, from ferromagnets to superconductors. Although it simplifies the complexity of microscopic interactions, it remarkably captures the essential features of phase transitions, particularly the concept of an order parameter and

the role of symmetry breaking. First order transitions are characterized by a discontinuous change in entropy and volume. A classic example is the transition from ice to water. In a first-order transition, the system absorbs or releases a fixed amount of energy, known as latent heat. This energy is necessary for breaking or forming the intermolecular bonds that define the phases. The Clausius-Clapeyron equation,

$$\frac{dT}{dP} = \frac{T\Delta V}{\Delta H} \tag{32}$$

where ΔH is the latent heat and ΔV is the change in volume, is particularly relevant in describing these transitions. The equation shows how the pressure and temperature at which the transition occurs are related. During a first-order transition, properties such as density and enthalpy show abrupt changes, and the system can coexist in both phases at the transition point. As external conditions, such as temperature or pressure, are varied, the system reaches a point where the symmetrical state becomes unstable, and a new, less symmetric state becomes energetically favorable. The Landau theory of phase transitions provides a framework for describing these transitions, modeling the free energy of a system as a function of the order parameter and showing how different minima in the free energy landscape correspond to different phases of the system [72].

In lattice QCD, the determination of an analytic crossover or a phase transition involves numerical simulations that compute thermodynamic quantities across a range of temperatures and chemical potentials. For an analytic crossover, researchers look for smooth, continuous changes in observables such as the chiral condensate or the Polyakov loop without any discontinuities or singularities. This behavior indicates that the system is undergoing a gradual transition between phases [73]. In the case of a phase transition, particularly a first-order phase transition, simulations focus on identifying discontinuities in the first derivatives of the free energy, such as the entropy or the order parameter. The presence of hysteresis

loops in the order parameter as a function of temperature, or the development of a double peak structure in the probability distribution of an observable at finite volume, can signal a first-order transition [74]. The critical point, marking the end of the first-order phase transition line and the beginning of the crossover region, is especially challenging to locate. It requires precise simulations at finite baryon densities, which are complicated by the sign problem. Various methods, including Taylor expansion, reweighting techniques, and the imaginary chemical potential approach, are utilized to circumvent these difficulties and estimate the location of the critical point [75], [76].

1.3.2 Hydrodynamic description of the system

Hydrodynamics is a theoretical framework used to describe the macroscopic behavior of many-body systems in terms of averaged quantities, such as density, velocity, and temperature. It is rooted in the conservation laws (e.g., conservation of energy, momentum, and number of particles) and is employed when certain conditions are met. To use the framework of hydrodynamics there are some condition which are relevant in the context of thermodynamics.

Hydrodynamics is a macroscopic theory, which means it deals with average or coarse-grained quantities rather than individual microscopic details. In many systems, there are microscopic interactions, collisions, or scatterings that work to equilibrate or thermalize the system. In a globally equilibrated system, quantities like temperature or pressure are uniform throughout the entire system. However, in many practical scenarios, especially those where hydrodynamics is applied, the system is not in global equilibrium. Instead, different regions of the system might be at different temperatures or velocities due to external influences, boundary conditions, or initial conditions. Despite these global differences, if over small enough regions (or "patches") the system has undergone enough interactions to be approximately in thermal equilibrium, then we say the system is in local equilibrium. Even if two neighboring regions are at different temperatures, within each small region, there

have been enough interactions to establish a local thermal equilibrium. So, within that patch, particles have a Maxwell-Boltzmann (or Fermi-Dirac or Bose-Einstein, depending on the statistics) distribution corresponding to that local temperature, Similarly, even if there are global flows or velocity gradients in the system, within each small patch, there is a well-defined average velocity. It is essentially a drift velocity of the medium in that small region. The mean free path is the average distance a particle travels between successive collisions. For hydrodynamics to be valid, the characteristic length scale L of the system (like the size of the fluid or the scale over which properties change) should be much larger than the mean free path: $L \gg \lambda$. This ensures that there are many collisions over scales of interest, leading to a smoothing out or averaging of microscopic details. Hydrodynamic models in heavy-ion collisions are grounded in the principle of local thermal equilibrium, implying the system's behavior can be described by macroscopic thermodynamic variables. These models, including the TRENTo model for initial state parameterization, are frameworks in simulating the evolution of quark-gluon plasma (QGP) and its interaction dynamics, especially regarding light quarks. Their success in reproducing experimental observables like particle spectra validates the rapid thermalization assumption and underscores the utility of thermal physics in describing complex QCD phenomena [77], [78]. Elliptic flow (see Figure 10), represented by the azimuthal anisotropy coefficient v_2, emerges as a key observable for testing the fidelity of hydrodynamic models. This phenomenon results from the conversion of initial spatial anisotropies into momentum anisotropies, facilitated by the collective flow of the QGP. The ability of these models to accurately predict elliptic flow measurements across various collision conditions attests to their effectiveness in capturing the essential physics of QCD under extreme conditions [79]. Furthermore, the analysis of elliptic flow provides insights into the transport properties of the QGP, notably the shear viscosity to entropy density ratio (η/s). A low η/s ratio, inferred from elliptic flow data, suggests that the QGP behaves akin to a near-perfect fluid. This observation, aligned with predictions from the AdS/CFT correspondence, highlights the QGP's unique fluid dynamics properties and reinforces the

relevance of hydrodynamic models in understanding the microscopic processes governing heavy-ion collisions [80]. [77] [79], [80]

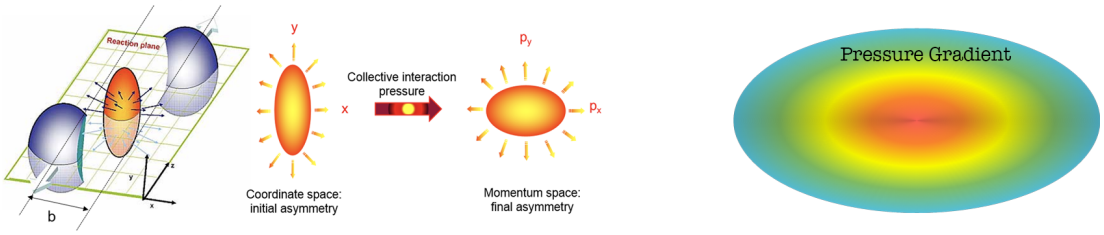

Figure 10: The illustration of the elliptic flow in the heavy ion collisions, the initial asymmetry in the initial state of the collisions in the overlap region, this would result in the final anisotrophy of the light hadrons such as pions and kaons and protons

1.3.3 Lattice QCD and equation of state

Lattice QCD discretizes spacetime onto a grid, approximating continuous space and time. Using Monte Carlo methods, it samples configurations of quark and gluon fields. At zero chemical potential, it explores the QCD phase diagram, revealing insights into confinement and chiral symmetry breaking. Near 150 MeV, it studies the crossover transition between hadronic matter and quark-gluon plasma, providing valuable information about the thermodynamics of strongly interacting matter. In lattice Quantum QCD, the continuous spacetime is divided into a grid of points, forming a four-dimensional lattice with a fixed spacing. This discretization allows us to estimate integrals over regions of spacetime by summing over these lattice points, as expressed by the equation:

$$\int d^4x \approx a^4 \sum_{\vec{n}} \tag{33}$$

To explore the configurations of quark and gluon fields, methods such as Monte Carlo simulations are employed. These methods sample field configurations based on their

probability, determined by the action $S(\phi)$, with acceptance probabilities determined by

$$P(\phi) \propto e^{-S(\phi)} \tag{34}$$

Moreover, integrals of functions are approximated by averaging function values at randomly chosen points, a process known as Monte Carlo integration. This principle is mathematically represented as the sum of function values at sampled points, given by

$$\int f(x)\,dx \approx \frac{1}{N}\sum_{i=1}^{N} f(x_i) \tag{35}$$

Additionally, the Wilson loop operator in studying gauge field strength, is approximated by considering the product of gauge links around a closed path, aiding in the study of QCD phenomena on the lattice, as defined by:

$$W(C) = \frac{1}{N_c}\mathrm{Tr}\left(\mathcal{P}\exp\left(ig\oint_C A_\mu dx^\mu\right)\right) \tag{36}$$

P denotes path ordering, g is the strong coupling constant, and A_μ is the gauge field associated with the gluons. The integral is taken over the closed loop C, and the trace is taken in the color space. The behavior of the Wilson loop is closely related to the confinement phenomenon in QCD. The area law of the Wilson loop, where the expectation value of the loop decreases exponentially with the area enclosed by the loop, is indicative of quark confinement. This means that the potential energy between quarks increases linearly with distance, suggesting that quarks are permanently bound into hadrons. The Wilson loop is gauge-invariant, meaning its value does not change under gauge transformations. This property makes it a particularly useful tool for probing the non-perturbative aspects of QCD, where traditional perturbative techniques are not applicable. In lattice QCD, thermodynamic variables are derived from the derivatives of the lattice free energy, which characterizes the equilibrium state of the system. Pressure, entropy, energy density, and susceptibilities

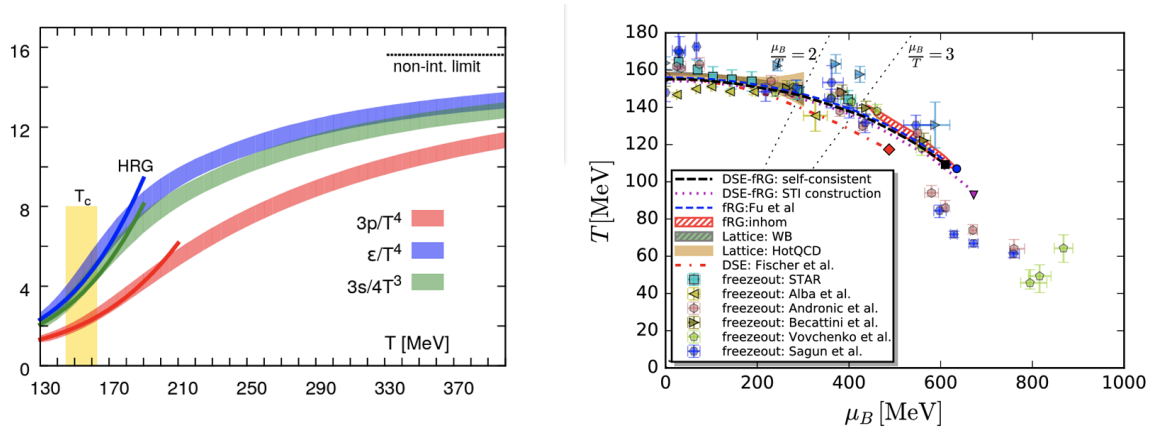

Figure 11: Dimensionless variables representing the pressure (red), energy density (blue) and entropy density (green) as the function of temperature at lattice QCD calculation at zero chemical potential (left) [81] The location of the critical point in the 2D phase diagram, temperature vs chemical potential by various theoretical frameworks and lattice QCD (right) [82]

are obtained by taking derivatives of the free energy with respect to volume (see Figure11, left), temperature, and chemical potential at appropriate conditions. Pressure is computed from the derivative with respect to volume, entropy from the derivative with respect to temperature, and energy density from a combination of volume and inverse temperature derivatives. Susceptibilities, representing the system's response to external perturbations, can be obtained from higher-order derivatives. Through numerical or analytic methods, these derivatives provide valuable insights into the thermodynamic behavior, equation of state, and phase transitions of strongly interacting matter in lattice QCD simulations (Figure11, right).

2 The ALICE detector

ALICE is one of the four main experiments at the Large Hadron Collider (LHC), the world's largest and most powerful particle accelerator. Unlike the ATLAS and CMS experiments, which are general-purpose detectors designed to explore a wide range of physics, ALICE is specialized to study the quark-gluon plasma. This influenced every decision made about its components and instrumentation. Other experiments like ATLAS and CMS optimized for a broad spectrum of particle physics research, including the search for the Higgs boson, supersymmetry, and more. One of the most illustrative examples is the Time Projection Chamber (TPC) as it is shown in Figures 12 and 13, which is the primary tracking detector in ALICE. The TPC has millions of readout channels, allowing it to detect and distinguish between particles even when they're produced very close to one another in space and time.

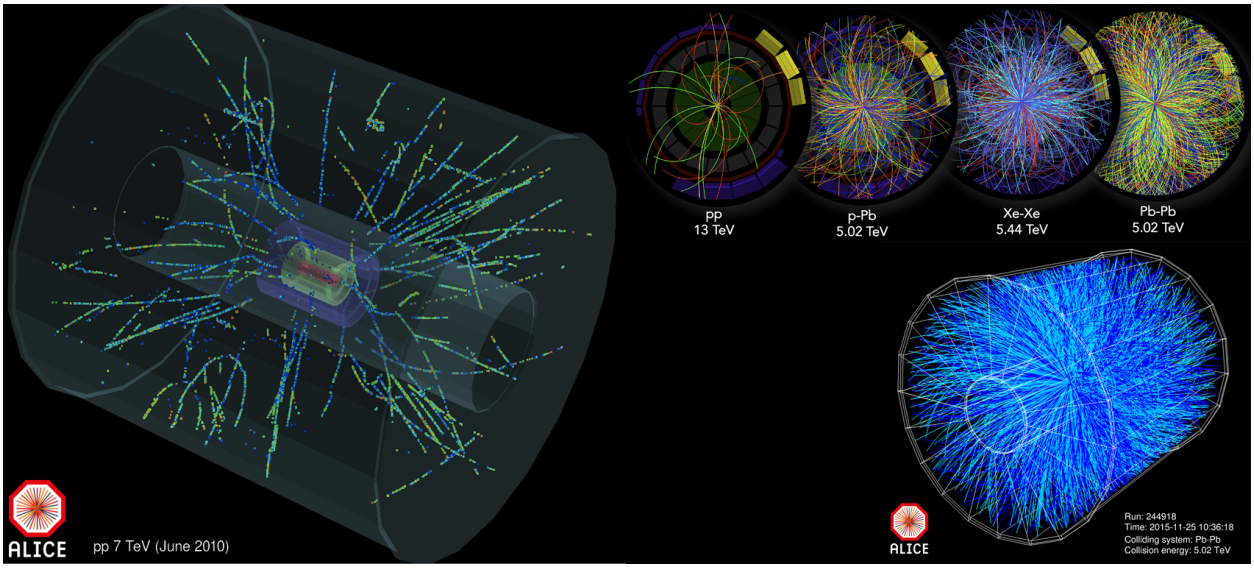

Figure 12: Visualization of collision events in the ALICE detector's Time Projection Chamber (TPC). The left image shows tracks of charged particles from a proton-proton collision at 7 TeV in June 2010. The series on the right displays the complexity of different collision systems, including proton-proton (pp) at 13 TeV, proton-lead (p-Pb) at 5.02 TeV, xenon-xenon (Xe-Xe) at 5.44 TeV, and lead-lead (Pb-Pb) at 5.02 TeV, with each collision energy denoted.

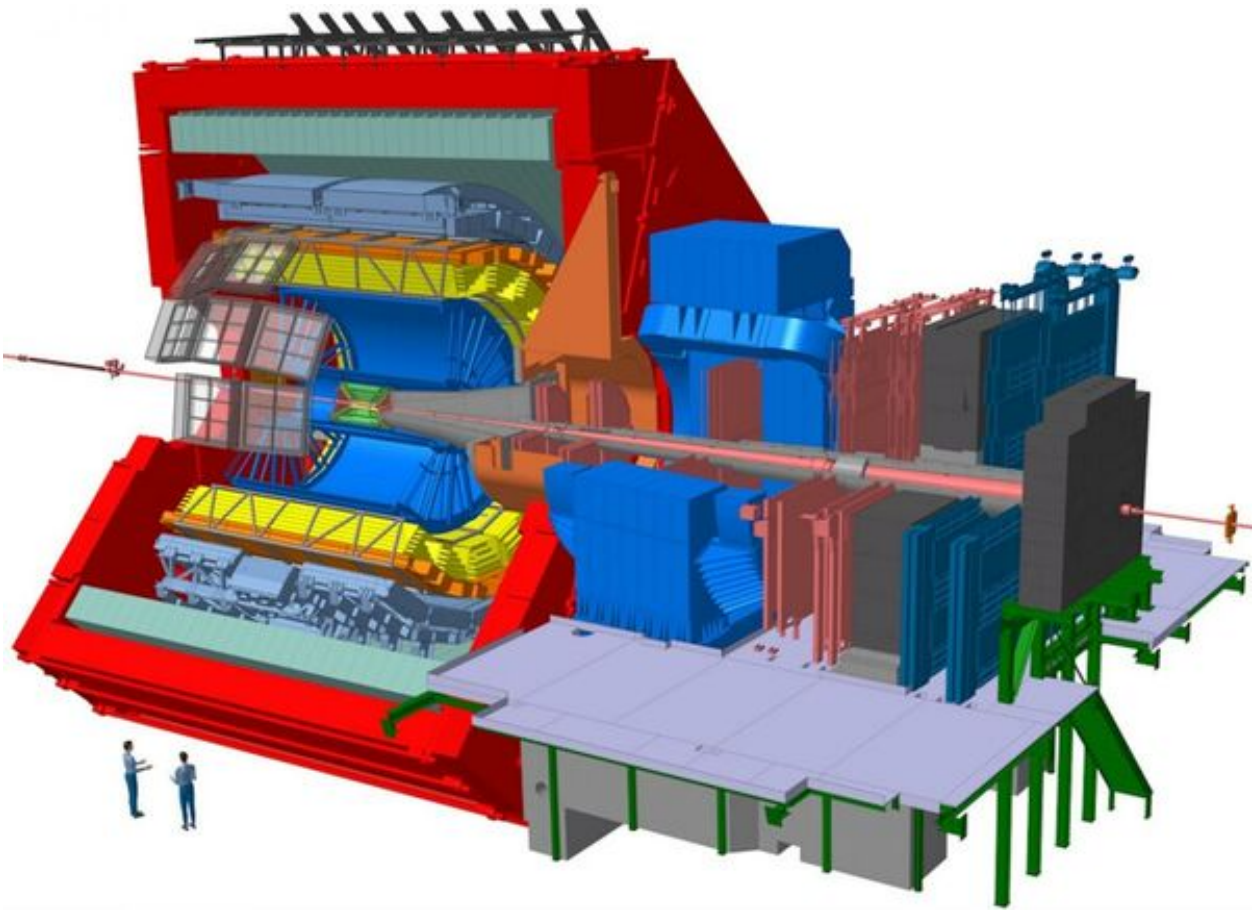

Figure 13: Schematic picture of ALICE detector

2.0.1 LHC synchrotron

The first operational synchrotron was developed in the 1940s. This technology marked a leap forward, as synchrotrons were capable of accelerating particles to energies much higher than their predecessors. Early synchrotrons could accelerate particles to several GeV (Giga-electron Volts), and modern synchrotrons can reach even higher energies, in the range of hundreds of GeV, making them powerful tools for high-energy physics research. Synchrotrons accelerate particles using a combination of magnetic and electric fields. The particles are injected into a ring-shaped vacuum chamber and accelerated to high speeds by radio frequency (RF) cavities. As the particles gain energy, the strength of the magnetic field in the ring is progressively increased to keep the particles on a circular path. This dynamic adjustment of the magnetic field is a key difference from cyclotrons, where the magnetic field is constant.

The synchrotron's ability to synchronize the magnetic field strength with the particle's energy allows it to overcome the limitations of relativistic mass increase that affect cyclotrons. Synchrotrons have been built and operated by numerous major laboratories and institutions worldwide. Some notable examples include: CERN (European Organization for Nuclear Research), home to some of the world's most advanced synchrotrons and particle colliders (see Figure 14). Fermilab (Fermi National Accelerator Laboratory) in the United States, known for its contributions to high-energy physics. DESY (Deutsches Elektronen-Synchrotron) in Germany, a leading center for the study of particle and high-energy physics. SLAC National Accelerator Laboratory in the United States, which houses several state-of-the-art synchrotron facilities. KEK (High Energy Accelerator Research Organization) in Japan, renowned for its research in particle physics and accelerator science. Synchrotrons achieve high particle energies by expertly synchronizing increasing magnetic field strength and radiofrequency (RF) electric field pulses to accommodate the relativistic mass increase of particles as they approach the speed of light. This continuous acceleration process over many cycles, combined with the adjustment of the magnetic field to keep particles on a stable path, is key to reaching these elevated energy levels. The magnetic field strength in high-energy synchrotrons varies, with fields ranging from a few teslas to over ten teslas in some cases, as exemplified by the Large Hadron Collider (LHC) at CERN, which utilizes superconducting magnets producing a field strength of about 8.3 teslas. The particle mass also plays an important role, especially under relativistic conditions. Taking protons as an example, their rest mass is approximately 1.67×10^{-27} kilograms, but at near-light speeds, as in the LHC where protons are accelerated to up to 6.5 TeV, their relativistic mass increases significantly, corresponding to a Lorentz factor of around 6930. The radius of the particle's orbit in synchrotrons like the LHC is large, about 4.3 kilometers given its 27-kilometer circumference, allowing for the accommodation and control of these high-energy particles. In contrast, smaller synchrotrons used in medical or material science applications have much smaller radii, typically just a few meters, suited for lower energy requirements. These parameters underscore the scale and

precision involved in synchrotron operation, enabling the achievement of particle energies far beyond the capabilities of earlier accelerators.

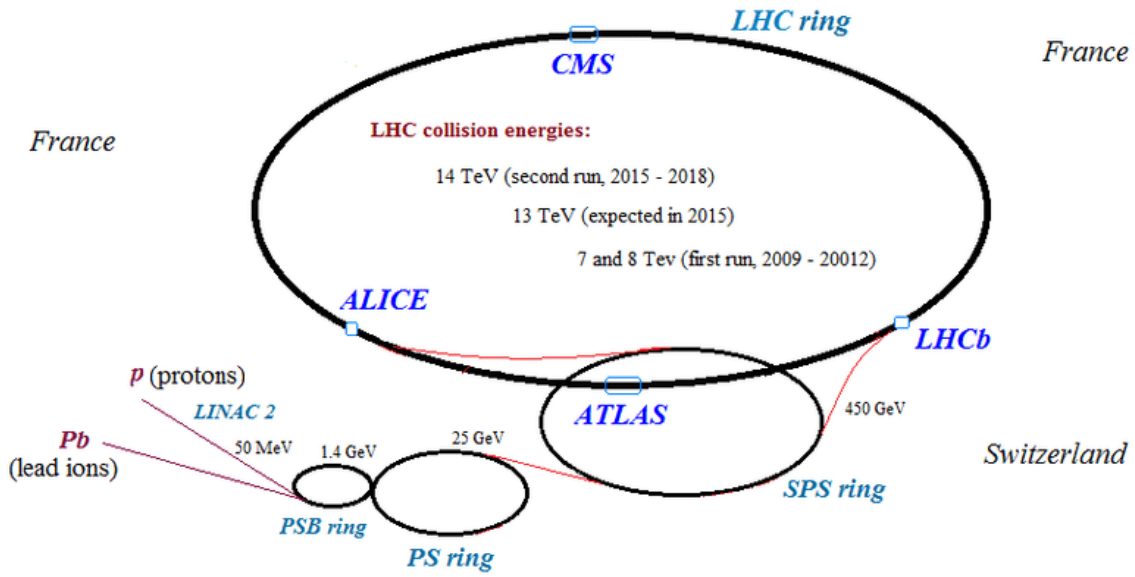

Figure 14: Schematic of the Large Hadron Collider (LHC) at CERN, illustrating the LHC ring with the CMS, ATLAS, ALICE, and LHCb detectors. The synchrotron is indicated, along with the beam lines for protons (p) and lead ions (Pb). Collision energies at various stages of the LHC operation are also noted.

2.1 Inner tracking system

Silicon Vertex Detectors, emerging in the 1980s, are a collective innovation in particle physics, born from the convergence of semiconductor technology and the need for enhanced precision in particle tracking. These detectors, integrating arrays of silicon wafers or strips, use the semiconductor properties of silicon to accurately detect and track charged particles. As these particles pass through the silicon, they generate electron-hole pairs, which are swiftly collected, providing precise electrical signals that map the particles' trajectories. This high spatial resolution is essential for pinpointing the vertices of particle collisions and decays, especially for short-lived particles like bottom and charm quarks. The development of Silicon Vertex Detectors is not credited to a single inventor but is the result of collaborative efforts

by physicists and engineers, particularly from leading particle physics laboratories such as CERN. Semiconductors have significantly enhanced particle detection technology, offering distinct advantages over older detector types. Their small band gap allows for the efficient conversion of a particle's energy into an electrical signal, providing a high degree of sensitivity and accuracy in detecting various particles.

2.1.1 Material budget

The "material budget" in reference to detectors like the Inner Tracking System (ITS) of ALICE at CERN, refers to the total amount of material that particles must traverse as they move through the detector. It is usually expressed as a fraction of the radiation length (X_0), which is a property of the material and is defined as the length over which a high-energy electron will lose $\frac{1}{e}$ (about 63.2) of its energy primarily through bremsstrahlung, or equivalently, the distance over which a photon has a 63.2 chance of being absorbed or scattered. The material budget is a critical parameter for the design and performance of particle detectors for several reasons. As particles pass through material, they interact with the atoms and electrons in the material. This can lead to scattering, which can change the trajectory of the particles. For high-precision tracking detectors, it is crucial to minimize these interactions to preserve the accuracy of the particle tracks. Particles lose energy as they traverse material, primarily through ionization and radiation. This energy loss can affect the performance of the detector and the accuracy of particle identification and momentum measurement. Interactions between particles and the detector material can produce secondary particles. This background noise can complicate the analysis of the data and reduce the detector's ability to accurately identify and track particles. For these reasons, a low material budget is desirable, especially for the innermost layers of tracking detectors, which are closest to the collision point and where the precision of track reconstruction is most critical. The ALICE Inner Tracking System (ITS), positioned closest to the interaction point, plays a the most important role in the charmed hadron reconstruction. Its functions include identifying the primary collision vertex with a

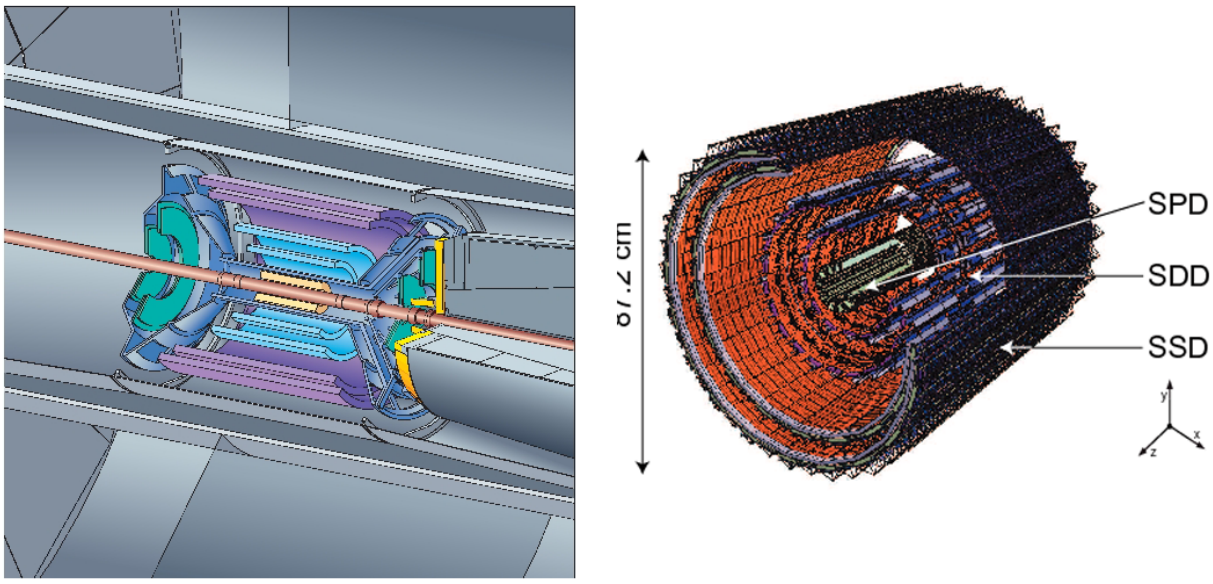

Figure 15: The left image shows a cutaway view of the ALICE inner tracking system, revealing the integration of various detector components. The right image is a wireframe model detailing the layers of the Silicon Pixel Detector (SPD), Silicon Drift Detector (SDD), and Silicon Strip Detector (SSD), with the overall dimension of the system indicated as 87.2 cm.

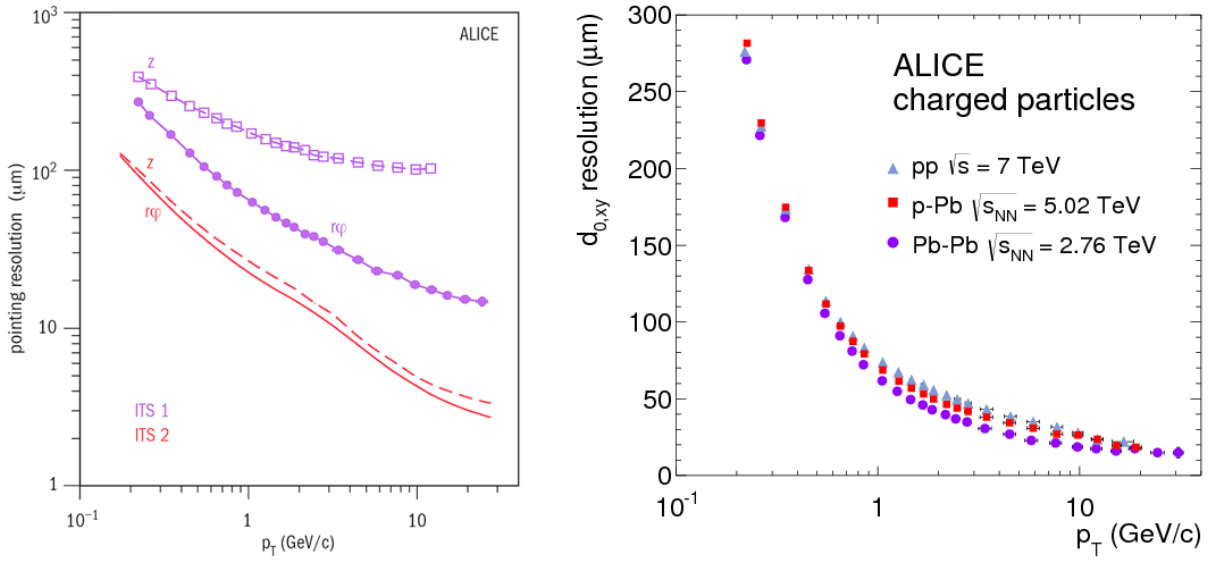

Figure 16: The resolution of ITS at Run1 and Run2 (left), the impact parameter charged particles (right)

resolution below 100, detecting secondary vertices from hyperon (Λ, Ξ^-, Ω^-) and heavy flavor decays, facilitating PID and tracking for low p_T particles ($p_T < 200$ MeV/c), and enhancing p_T and angular measurement precision in conjunction with the TPC. Additionally, ITS is vital for charm hadron reconstruction, capable of detecting their few-micrometer decay lengths [83]. It consists of six layers of silicon-based detectors, including Silicon Pixel Detectors (SPD), Silicon Drift Detectors (SDD), and Silicon Strip Detectors (SSD), each chosen for their precision in tracking and vertexing capabilities (see Figure 15). The primary purpose of the ITS is to accurately pinpoint the location of collision vertices, reconstruct the trajectories of particles, especially those with low momentum, enhance the momentum resolution, and contribute to the identification of different particle species. The ITS is designed to have a low material budget to minimize these adverse effects, especially multiple scattering, which can degrade the momentum resolution and vertex reconstruction accuracy. The SPD layers are closest to the interaction point and are designed with the thinnest possible materials to minimize multiple scattering. The goal is to keep the material budget as low as possible, typically aiming for less than about 1 percent of the radiation length per layer.

2.1.2 SPD

Hybrid silicon refers to a technology used in particle detectors, combining silicon sensor elements with separate readout electronics. The sensor elements detect charged particles, and the readout electronics, which are bonded to the sensors using conductive bumps, process and record the signals. This combination allows for high-precision tracking and data acquisition in high-energy physics experiments. Silicon is used in particle detectors because of its semiconductor properties, which allow for high-resolution tracking of charged particles. Its bandgap energy ensures efficient charge collection and signal generation when particles pass through. Silicon detectors provide fine spatial resolution, are relatively radiation-hard, making them suitable for high-radiation environments, additionally, its well-understood technology is adaptable for various detector designs, from pixel detectors to strip and drift detectors,

accommodating diverse experimental requirements. The first two inner layers of the ITS are composed of Silicon Pixel Detectors (SPD), situated at distances of 3.9 cm and 7.6 cm from the beam axis [83]. The primary functions of these layers include assisting in the identification of the primary vertex and measuring the impact parameter for tracks from the weak decays of strange, charm, and bottom hadrons. Each SPD cell measures 50 μm by 425 μm (see Figure 16), with a total of approximately 9.84×10^6 cells across the SPD [83]. The detectors offer a broad pseudorapidity range of $-1.98 < \eta < 1.98$.

2.1.3 SDD

The Silicon Drift Detector (SDD) is positioned as the middle layers between the innermost Silicon Pixel Detectors (SPD) and the outermost Silicon Strip Detectors (SSD). The SDD consists of a silicon sensor that operates on the principle of sideways drift of electron-hole pairs in an applied electric field towards a collecting anode. The design of the SDD allows for precise spatial resolution in two dimensions. This is achieved by applying a voltage gradient across the detector, causing electrons generated by incoming charged particles to drift towards the anodes. The drift time is measured and, along with the known drift velocity, is used to determine the position where the particle interaction occurred. The subsequent two layers of the ITS consist of Silicon Drift Detectors (SDD), positioned at radii of 15.0 cm and 23.9cm from the beam axis. These layers excel in multi-particle tracking and supply energy loss (dE/dx) data crucial for particle identification (PID).

2.1.4 SSD

The Silicon Strip Detector (SSD) is another integral component of the ALICE experiment's Inner Tracking System (ITS), situated as the outermost layers of the detector array. The SSD is composed of silicon sensors equipped with narrow, elongated strips that act as individual particle detection elements. These strips are doped to create p-n junctions that produce electrical signals when charged particles traverse the silicon, ionizing atoms along their path.

Silicon Strip Detectors (SSD) form the two outermost layers of the Inner Tracking System (ITS) and are positioned at radii of 30.0 cm and 43.0 cm from the beam axis. SSDs offer a two-dimensional measurement of track position, which is crucial for matching tracks from the ITS to the Time Projection Chamber (TPC). They also provide information on energy loss dE/dx which is valuable for particle identification (PID) of low momentum particles. The cells in SSDs are significantly larger than those in the Silicon Drift Detectors (SDD) and Silicon Pixel Detectors (SPD), measuring $95\mu\text{m} \times 40000\mu\text{m}$ each, with a total of approximately 2.6 million (2.6×10^6) cells. [83]

2.2 Time projection chamber

The ALICE Time Projection Chamber (TPC) is the primary tracking and particle identification (PID) device in ALICE. Working together with other detectors in the central-barrel, the TPC aims to provide accurate momentum measurements for charged particles, ensure good two-track separation, facilitate PID, and assist in vertex determination. The TPC, cylindrical in shape and the largest of its kind globally, has a total volume of 90 m^3, an inner radius of approximately 85 cm, an outer radius of about 250 cm, and a length of 500 cm along the beam axis. It is filled with a gas mix of 90% neon and 10% CO_2 (see Figure 18). The TPC encompasses the full azimuth ($0 \rightarrow 2\pi$) and a pseudorapidity range of $|\eta| < 0.9$ ($|\eta| < 1.5$ for shorter tracks [83], but with lower momentum resolution). It comprises a substantial field cage with a central high voltage electrode positioned in the middle and two read-out endplates, one on each side of the TPC. When a charged particle from a collision enters the TPC, it traverses the gas-filled chamber, ionizing gas molecules. This ionization process causes electrons (and ions) to drift toward the endplates, influenced by the electric potential of the central high voltage electrode, set at 100 kV. This electrode generates a uniform electric field of 400 V/cm [83] in the beam direction (z-direction) inside the gas chamber. The endplate readout chambers are Multi Wire Proportional Chambers (MWPC) (see Figure 17) equipped with cathode pad readout and a gated wire grid. This grid acts to obstruct drifting

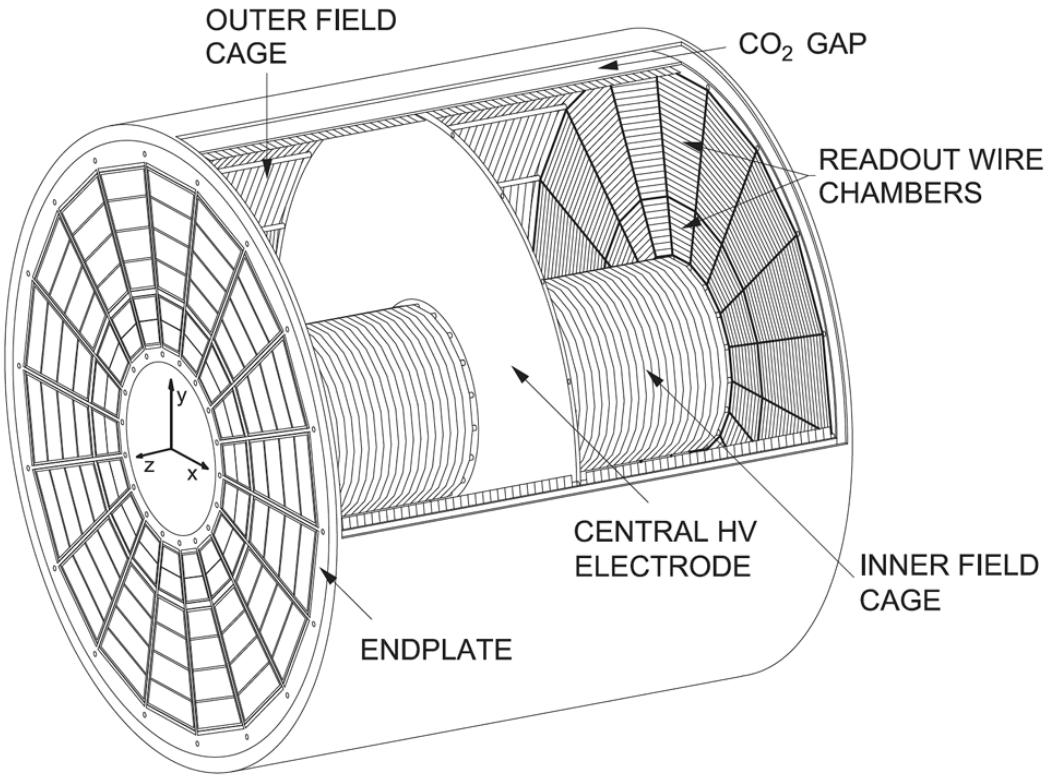

Figure 17: A charged particle's trajectory within the TPC drifts towards the readout system

charges when the TPC is not triggered. The electrons interact with the grid of charged wires, instigating an avalanche of electrons. This results in the secondary production of electrons and ions. Given that the drifting electrons from the initial ionization of the gas do not induce a sufficiently large signal in the readout planes, this amplification process becomes necessary. In the Time Projection Chamber (TPC), the quantity of secondary electrons produced offers insights into the number of primary electrons induced, revealing the energy loss dE/dx of the charged particle as it moves through the TPC. Furthermore, the generation of secondary ions provides information regarding the spatial location of the charged particle in the xy-plane. The maximum drift time is approximately $90\mu s$, indicative of the duration for which the gating plane remains open, permitting electrons to drift towards the pad planes. The ALICE TPC and other central-barrel detectors are located within a 0.5 T [83] solenoidal magnetic

field. This constant magnetic field, in conjunction with the TPC's electric field, induces a curved, or helical, path for charged particles passing through the chamber. The particle's direction post-collision and the influence of the electric field are initial determinants of its path, but the magnetic field introduces a circular motion component to the trajectory via the Lorentz force.

$$F = qE + v \times B \tag{37}$$

where F is the net Lorentz force acting on the charged particle, q is the charge, E is the external electric field, v is the particle's linear velocity, and B is the external magnetic field. Assuming the magnetic field is perpendicular to the charged particle's momentum in the TPC, the magnetic component of this equation simplifies to

$$qvB = \gamma m v^2/r \tag{38}$$

By substituting the mass and velocity with relativistic transverse momentum ($p_T = \gamma m v$), this further simplifies to

$$qB = p_T/r \tag{39}$$

Particularly, charged particles with $p_T \leq 100$ MeV/c are curved so extensively by the strong magnetic field that they fail to reach most central-barrel detectors. The TPC uses energy loss per unit length (dE/dx) of the charged particle in the gas chamber in order to identify particles. The energy loss in the TPC can be theoretically described by the Bethe-Bloch parameterization [83]:

$$\frac{dE}{dx} = 4\pi N e^4 \frac{mec^2}{Z^2\beta^2} \ln\left(\frac{2mec^2\beta^2\gamma^2}{I}\right) - \beta^2 - \delta(\beta)\frac{1}{2} \tag{40}$$

where N is the number density of electrons in the gas medium, e is the elementary electric charge, mec^2 is the rest energy of the electron, Z is the charge of the particle, β is the speed of the particle over the speed of light (v/c), γ is the Lorentz factor ($\frac{1}{\sqrt{1-\beta^2}}$), and I is the

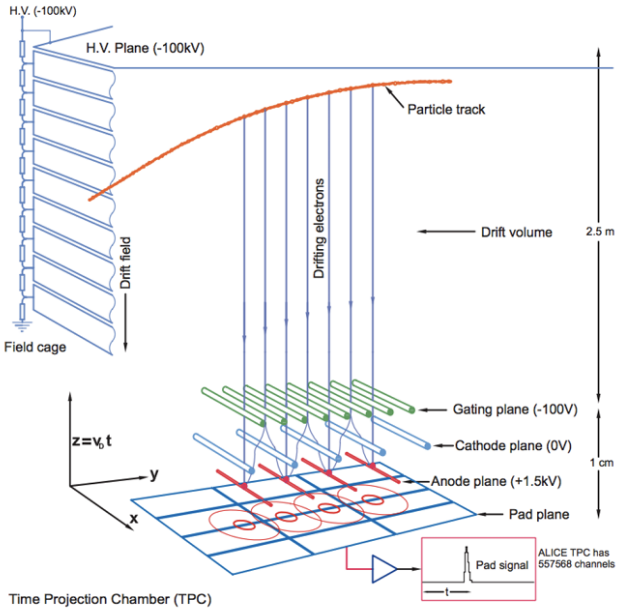

Figure 18: A schematic of the ALICE Multi Wire Proportional Chamber as a readout system for the driifted electron from ionization of the gas

mean excitation energy of the atom. Particle identification is performed by evaluating $n\sigma$, which represents the deviation of the measured value of dE/dx from the theoretical value given by the Bethe-Bloch parameterization, normalized by the resolution of the TPC:

$$n\sigma = \frac{(dE/dx)_{\text{measured}} - (dE/dx)_{\text{Bethe-Bloch}}}{\sigma_{\text{TPC}}} \tag{41}$$

The closer $n\sigma$ is to zero, the more closely the track aligns with the theoretical Bethe-Bloch value (see Figure 19), enhancing the confidence in identifying the track as the correct particle species.

2.3 Time of flight

The Time of Flight (TOF) detector was designed and implemented to enhance ALICE's capability for identifying charged particles, addressing a gap left by the TPC, which struggles with accurate identification in the intermediate momentum range. The TOF effectively covers

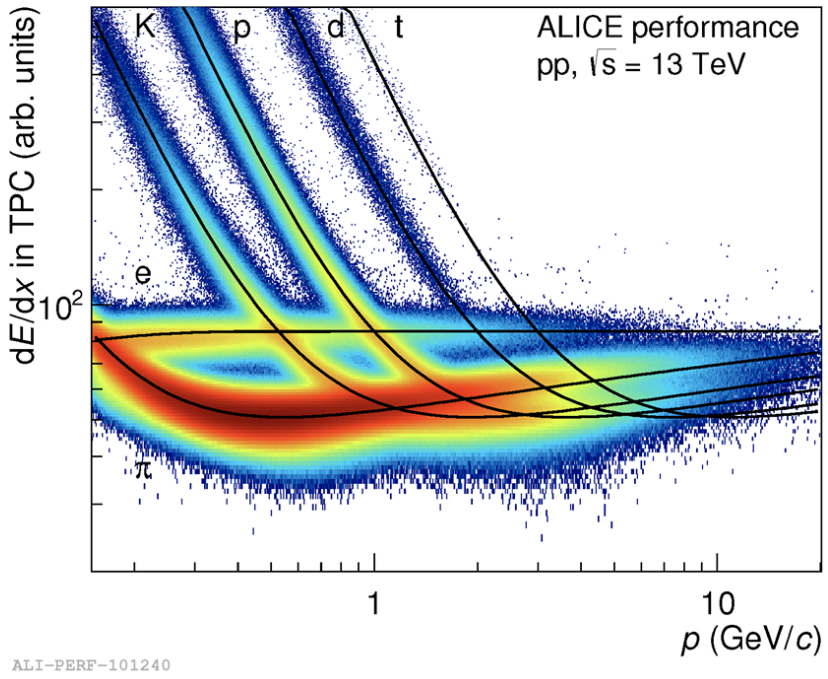

Figure 19: Specific energy loss (dE/dx) vs momentum in the TPC for 0.2 T for Run 2 pp collisions at $\sqrt{s} = 13$ TeV. Solid black lines indicate the signal calculated from the Bethe-Bloch formula for a particle species. Color intensity corresponds to the number of signals for dE/dx measured for a specific p value.

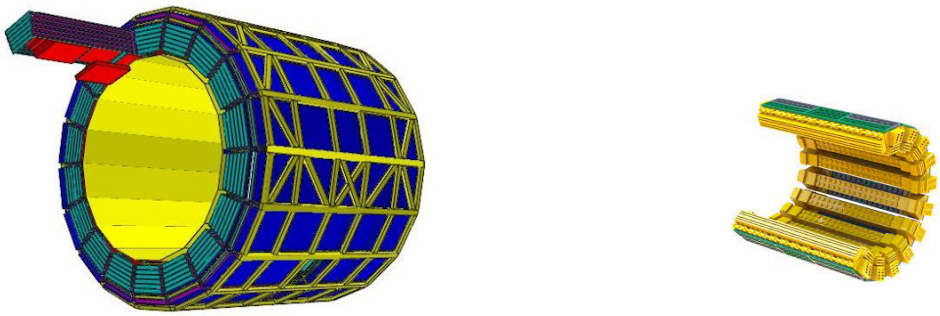

Figure 20: The images showcase the Time of Flight (TOF) detector system. The left image presents a sectional view of the TOF barrel, illustrating its geometric arrangement around the central axis.

this missing momentum range from approximately 0.4GeV/c to 3GeV/c [83]. Together, the ITS, TPC, and TOF extend the particle identification capabilities across a broad transverse momentum spectrum, ranging from 0.150GeV/c to 20GeV/c. The ALICE TOF is a cylindrical detector that has a pseudorapidity coverage of $|\eta| < 0.9$ over the full azimuth ($0 \rightarrow 2\pi$). The TOF has a modular structure that consists of 18 sectors in ϕ and 5 segments in the beam direction. The entire TOF is inside a cylindrical shell with an inner radius of 370 cm and an outer radius of 399 cm away from the beam pipe. TOF geometrical illustration is shown in Figure 20 The TOF contains 1638 Multigap Resistive Plate Chamber (MRPC) strips (see Figure 21). Each MRPC strip is 122 cm long by 13 cm wide [83] and consists of stacks of glass plates with a high voltage applied to its external surface. When a charged particle traverses the TOF, it ionizes the gas molecules in between the gaps of the plates, which causes a gas avalanche. This means that the freed electrons will be accelerated by the electric field in the TOF, which causes them to bump into more gas molecules which will free even more electrons, amplifying the electric signal The resistive glass plates are not only transparent to the signal produced, they also stop the avalanche in order to prevent the amplification from sparking. Using the timing information, the TOF can determine the mass

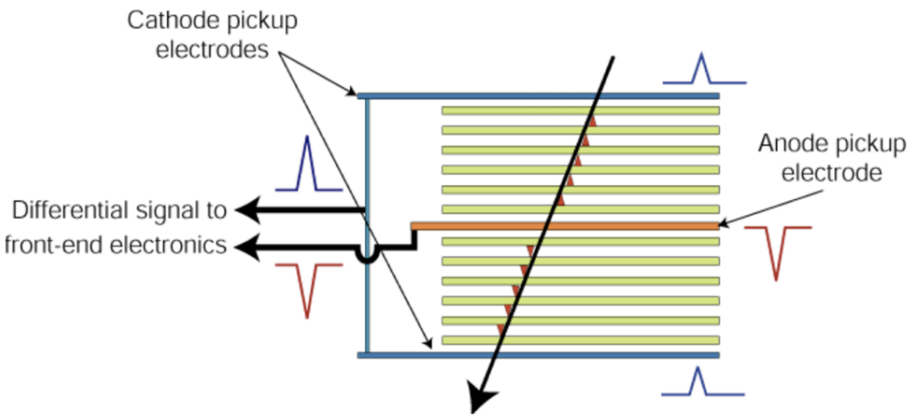

Figure 21: A charged particle passes through a Time-Of-Flight (TOF) detector that contains ionizing gas molecules, it initiates a series of interactions that lead to the generation of an electric signal.

of the particle by the equation (see Figure 22, [83])

$$m = \frac{p}{c}\sqrt{\left(\frac{c^2t^2}{l^2} - 1\right)} \tag{42}$$

where m is the mass of the particle, p is its momentum as measured by the ITS/TPC, t is the time of flight, and l is the track length. The initial starting time of the particle at the primary vertex is determined by the T0 detector, which will be discussed in the next section. The main scope of the TOF is to find the time of flight of each particle from the primary vertex to the TOF detector. The timing obtained from the TOF signal combined with the distance the particle traveled will determine the velocity $\beta = v/c$. The primary purpose of the TOF is to obtain a difference between the signals of K^-p and K^-. In order to achieve this, the TOF is optimized so that a 3σ separation between π and K is achievable at the higher end of the momentum range for a particle track of 4 meters.

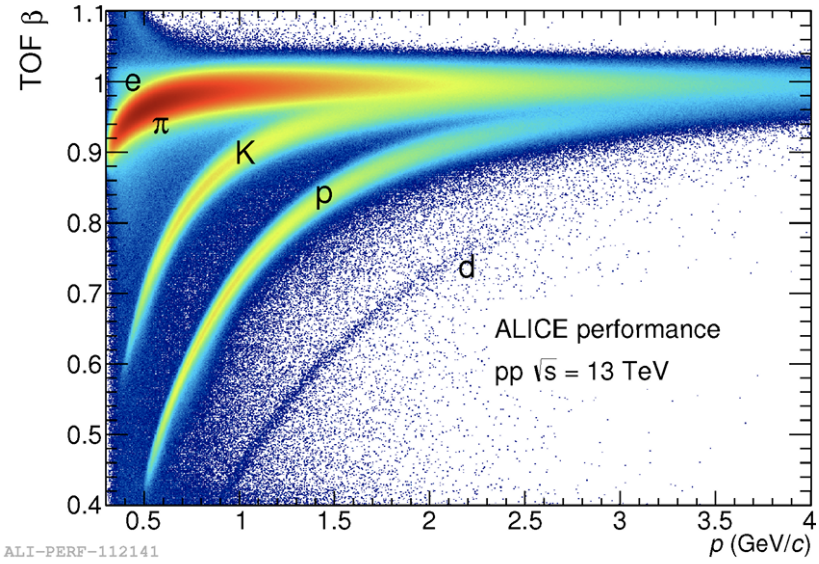

Figure 22: Performance plot of TOF β versus momentum in proton-proton collisions at $\sqrt{s} = 13\,\text{TeV}$.

2.4 V0 and T0 detector

The V0 detector is designed as a small angle detector, comprising two distinct arrays of scintillator counters: VZERO-A and VZERO-C, positioned on opposing sides of the interaction point. Specifically, VZERO-A is situated 340 cm away from the interaction point, opposite the muon spectrometer, while VZERO-C is positioned 90 cm from the interaction point. The V0-A covers a pseudorapidity range of $2.8 \leq \eta \leq 5.1$, while VZERO-C spans $-3.7 \leq \eta \leq -1.7$ [83] (see Figure 23). The primary function of the VZERO detector is to act as a trigger for the central-barrel detectors in minimum-bias events during pp and A-A collisions. Upon a collision, emitted particles from the primary vertex can initiate this trigger, as can secondary interactions within the vacuum chamber elements. A linear relationship exists between the count of detected particles by the VZERO and the quantity of primary particles emitted, thus enabling the VZERO detector to effectively indicate the centrality of a Pb-Pb collision through event multiplicity measurement. A basic trigger mechanism employed is the minimum-bias (MB) trigger, activated when any signal is detected in both VZERO-A and VZERO-C, marking the event for inclusion in the minimum-bias dataset

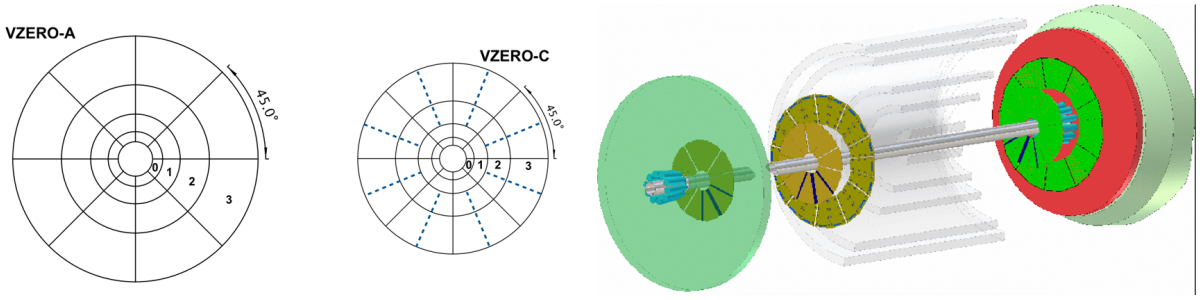

Figure 23: The diagrams present VZERO-A and VZERO-C, components of the event triggering and forward detection system. The leftmost images depict the layout of the scintillator arrays within each detector segment, denoted by their angular coverage. The right image illustrates a 3D model of the forward detector system, highlighting its longitudinal section and scintillator placement used for capturing spectator particles in collision events.

under trigger kINT7 [83]. These triggers are crucial in verifying the occurrence of an event and distinguishing genuine signals in the central-barrel detectors from those resulting from beam-gas interactions. The ALICE T0 detector consists of two arrays of Cherenkov counters. Similar to the VZERO detector, the T0 consists of two separate arrays that are located on different sides of the interaction point. The T0-C is located 72.7 cm away from the interaction point, covering a pseudorapidity range of $-3.28 \leq \eta \leq -2.97$, while the T0-A is situated 375 cm [83] from the interaction point, with a pseudorapidity range of $4.61 \leq \eta \leq 4.92$ [83]. The principal function of the T0 detector is to generate a start time for the TOF. The timing signal in the T0 serves as the real-time indication of the collision, independent of the collision vertex's position. Additionally, the T0 aids in determining the location of the primary vertex and helps to discriminate against beam-gas interactions.

3 Experimental studies on heavy flavor observables

3.1 Charmed hadron cross section

The question is how to calculate the cross sections of charmed hadrons within the most generalized approach across all collisions. In theory, The factorization approach is a method to break down the cross-section of charmed hadrons into three processes. This approach is especially applicable to heavy-flavor hadrons, rather than light-flavor hadrons, due to the substantial mass of the charm and beauty quarks. Specifically, the charm quark's mass is approximately 1.27 GeV/c^2, and the beauty quark's mass is around 4.18 GeV/c^2. These masses significantly exceed any potential perturbations or "kicks" from other partons or the surrounding environment, which might include interactions or momentum changes during the collision process. Therefore, these interactions cannot induce inelastic scattering on the charm quarks. This considerable mass disparity allows the use of the charmed hadrons' corrected yield as a reliable way to trace back to the primordial charm quark. The formula represents the observable cross-section for producing a specific hadron :

$$\sigma = \sum_{a,b} \int dx_a \int dx_b f_a(x_a, Q^2) f_b(x_b, Q^2) \hat{\sigma}_{ab\to c}(x_a, x_b, Q^2) D_{c\to h}(z, Q^2) \tag{43}$$

Where σ is the observable cross-section for producing a specific hadron h in the final state. The sum $\sum_{a,b}$ runs over all types of partons (e.g., quarks and gluons) in the colliding hadrons. $f_a(x_a, Q^2)$ and $f_b(x_b, Q^2)$ are the parton distribution functions (PDFs) for partons a and b in the initial state hadrons, which describe the probability of finding a parton with a fraction x_a or x_b of the hadron's momentum, evaluated at the scale Q^2. $\hat{\sigma}_{ab\to c}(x_a, x_b, Q^2)$ is the hard scattering cross-section for partons a and b to collide and produce a parton c, which is calculable using perturbative QCD for a given process at the scale Q^2. $D_{c\to h}(z, Q^2)$ is the fragmentation function for parton c to transform into the observed hadron h with a fraction z of the parton's momentum, also evaluated at the scale Q^2. The integrals over dx_a and dx_b

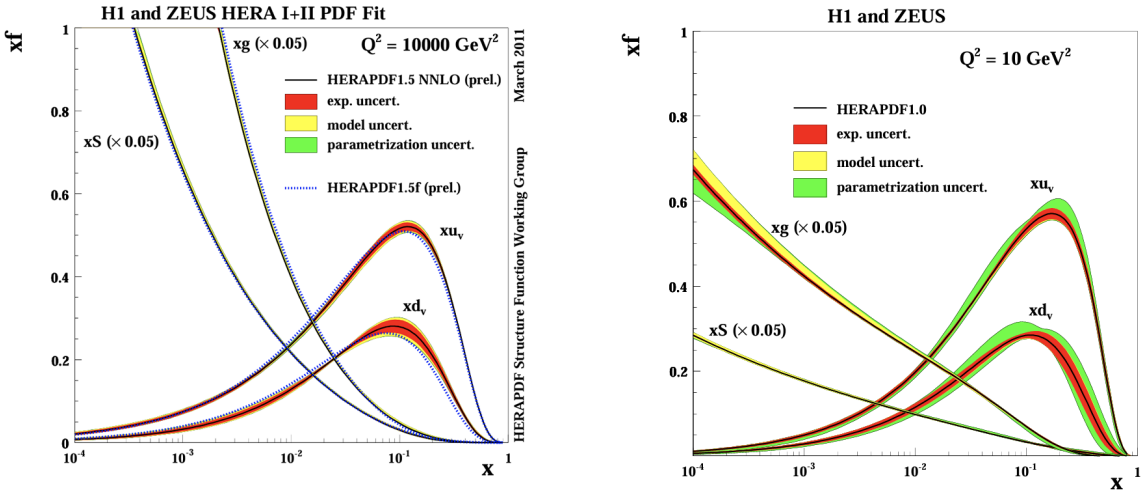

Figure 24: The parton distribution functions, derived from data obtained by the H1 and ZEUS collaborations, illustrate the variation in the cross-section of electron-proton scattering as a function of momentum fraction x and the square of the momentum transfer Q^2. These functions highlight the contributions of up and down quarks, as well as gluons. Notably, the gluon contribution significantly surpasses that of sea quarks at lower values of x, emphasizing the dominant role of gluons in this regime. Image credit: R.Placakyte presentation

represent the convolution of the PDFs and the hard scattering cross-section, integrating over all possible momentum fractions of the initial partons. The variable Q^2 typically represents the momentum transfer or the energy scale of the hard scattering process, which is a crucial parameter in both the PDFs and the fragmentation functions, reflecting the dependence of these functions on the resolution scale of the interaction.

3.2 Parton Distribution Functions

The initial stage involves Parton Distribution Functions (PDFs) which are mathematical tools to describe the probability of finding a parton inside a hadron (such as a proton or neutron) with a specific momentum fraction of the hadron's total momentum, at a given energy scale. such as those studied in QCD. In simpler terms, [84, 85, 86] PDFs help physicists understand how the momentum of a fast-moving hadron is distributed among its constituent quarks and gluons. This distribution is not fixed but depends on the energy scale at which the hadron is probed, reflecting the quantum nature of QCD. As the energy of the interaction increases,

more quarks and gluons, which are collectively referred to as partons, can be resolved, and the structure of the hadron as seen in a high-energy collision becomes more complex. PDFs are determined through experimental measurements, particularly from deep inelastic scattering experiments, where electrons or other particles are collided with hadrons at high energies, allowing to probe the internal structure of the hadrons. The resulting data, interpreted through the framework of perturbative QCD, are used to extract the PDFs, which then serve as essential inputs for theoretical predictions of processes in high-energy particle physics. [87, 88, 89] The process involves an electron scattering off a proton by exchanging a virtual photon. The kinematics of the scattering process are characterized by the squared momentum transfer Q^2 (a measure of the resolution of the probe) and the Bjorken scaling variable x, which is related to the fraction of the proton's momentum carried by the struck parton (see Figure 24 where PDF are illustrated at certein Q^2). The cross-section for electron-proton deep inelastic scattering can be expressed in terms of the structure functions $F_1(x, Q^2)$ and $F_2(x, Q^2)$, where $F_2(x, Q^2)$ is particularly relevant for extracting PDFs. The relationship between the differential cross-section and the structure functions is given by the formula:

$$\frac{d^2\sigma}{dxdQ^2} = \frac{4\pi\alpha^2}{xQ^4}\left[\left(1 - y + \frac{y^2}{2}\right)F_2(x, Q^2) - \frac{y^2}{2}F_1(x, Q^2)\right] \tag{44}$$

where σ is the cross-section for the scattering process, α is the fine structure constant, y is another kinematic variable related to the energy loss of the electron in the proton's rest frame, $x = \frac{2p\cdot q}{Q^2}$ is the Bjorken scaling variable, with p being the four-momentum of the proton and q the four-momentum of the exchanged virtual photon, $Q^2 = -q^2$ is the negative of the square of the four-momentum transfer. The structure function $F_2(x, Q^2)$ can be related to the PDFs by:

$$F_2(x, Q^2) = x \sum_{\text{flavors}} e_f^2 \left[f_f(x, Q^2) + f_{\bar{f}}(x, Q^2)\right] \tag{45}$$

where: The sum is over all quark and antiquark flavors f, e_f is the electric charge of the quark of flavor f in units of the elementary charge, $f_f(x, Q^2)$ and $f_{\bar{f}}(x, Q^2)$ are the PDFs for

quarks and antiquarks of flavor f, respectively, representing the probability density for finding a parton with a fraction x of the proton's momentum and at the scale Q^2. By measuring the differential cross-section of deep inelastic scattering experiments at various values of x and Q^2, and using theoretical models to interpret the data, researchers can extract the PDFs. These PDFs are crucial inputs for making predictions in high-energy physics, allowing for a detailed understanding of the proton's internal structure at different scales. The Glauber model acts as a bridge between parton distribution functions (PDFs) and hard scattering processes in heavy ion collisions by offering a geometric framework that estimates the number and distribution of nucleon-nucleon collisions based on impact parameter and nuclear density profiles. This model enables the assessment of initial conditions for parton-parton interactions within colliding nuclei. PDFs detail the momentum distribution of partons within a nucleon, setting the stage for these partons to engage in hard scattering—high-energy interactions characterized by significant momentum transfer. The Glauber model, through its picture of multiple scattering events at the nucleon level, indirectly facilitates an understanding of the spatial and momentum configuration of partons prior to hard scattering.

3.3 Hard scattering processes

In QCD, the scale at which perturbative calculations become applicable is determined by the strength of the strong force, as characterized by the QCD coupling constant (α_s). Perturbative QCD (pQCD) calculations are typically feasible when α_s is sufficiently small, which occurs at high energy scales due to the property of asymptotic freedom. This means that as the energy scale increases (or equivalently, as the distance scale decreases), quarks and gluons interact more weakly, making a perturbative approach viable. The QCD scale, Λ_{QCD}, is the energy scale below which the coupling constant becomes large and non-perturbative effects dominate. This scale is roughly on the order of 200 MeV to 300 MeV. Below this scale, the strong force becomes so strong that quarks and gluons are confined within hadrons, and perturbative techniques are no longer reliable. Perturbative calculations are generally

reliable in processes involving momentum transfers much larger than $\Lambda_{\rm QCD}$. For instance, in processes with momentum transfers or energy scales in the range of a few GeV or higher (e.g., hundreds of GeV to TeV), α_s is sufficiently small, and perturbative techniques can be effectively applied. For the production of heavy quarks like charm (c) and bottom (b) quarks, which have masses of about 1.3 GeV and 4.2 GeV respectively, the energy scales involved are typically much larger than $\Lambda_{\rm QCD}$. This allows for the use of perturbative QCD to calculate processes such as heavy quark pair production in high-energy collisions. The running of the QCD coupling constant, $\alpha_s(Q^2)$, with the energy scale Q^2 can be described by the renormalization group equation. At leading order, it is given by:

$$\alpha_s(Q^2) = \frac{12\pi}{(33 - 2n_f) \ln\left(\frac{Q^2}{\Lambda^2_{\rm QCD}}\right)} \tag{46}$$

where n_f is the number of active quark flavors at the energy scale Q^2. This equation illustrates how α_s decreases as Q^2 increases, enabling perturbative calculations at high energy scales. The number 33 in the formula for the running of the QCD coupling constant, $\alpha_s(Q^2)$, originates from the structure of Quantum Chromodynamics (QCD) itself, specifically from the QCD beta function at one-loop order. The beta function in QCD, which dictates how the coupling constant α_s changes with the energy scale Q^2, is derived from the quantum corrections to the strong force interactions. The formula at one-loop order is given by: $\beta(\alpha_s) = -\left(\frac{11}{3}C_A - \frac{4}{3}T_F n_f\right)\frac{\alpha_s^2}{2\pi}$ where C_A is the Casimir operator in the adjoint representation of the gauge group $SU(3)$ of QCD, which equals 3. T_F is the trace normalization of the fundamental representation, which equals $\frac{1}{2}$. n_f is the number of active quark flavors at the energy scale considered. In practical terms, pQCD is often used for processes involving high-momentum transfers, such as deep inelastic scattering, high-energy jet production, and heavy quark production, where the scale Q^2 (the momentum transfer squared) is much greater than the QCD scale parameter $\Lambda_{\rm QCD}$, which is in the range of 200 to 300 MeV.

3.4 Fragmentation

Fragmentation is a complex process initiated by initial quarks emitting an array of radiation, which subsequently decays into various types of quarks. This process results in the formation of quarks and gluons, which eventually aggregate into color-neutral hadrons. The essential aspect of fragmentation is its initiation by an initial parton, which could be either quarks or gluons. The dynamics of this process can be divided into perturbative and non-perturbative stages. Perturbative stages are crucial for understanding fragmentation, as they provide most of the information on multiplicity through the initial showers. These showers, characterized by collinear and soft radiations, form the basis of the theoretical explanation for the observed phenomena. Monte Carlo simulations play a important role in modeling these cascades of initial states, allowing for a detailed analysis of the fragmentation process. The concept of fragmentation, while primarily theoretical, faces challenges when connected to experimental observables due to the lack of direct access to initial partons. Instead, observations are confined to the final state of particles. Therefore, obtaining complete information about fragmentation processes is not straightforward and relies on the analysis of indirect effects. Primarily, the study of fragmentation can be conducted through jets, as they possess higher momentum. However, reconstructing heavy flavor particles that are not part of jets can also be used to study fragmentation.

A distinctive feature of heavy flavor hadrons, in contrast to light hadrons, lies in the production process of heavy quarks, such as charm and beauty quarks. Unlike light quarks, heavy quarks are not generated within the quark-gluon plasma. They are primarily produced through energetic exchanges of gluons or photons. This distinction holds true even in proton-proton collisions, where the concept of an extensive quark-gluon plasma does not apply. In a perfect situation where we identify one jet, we can look closely at everything that comes out of this jet and how these smaller parts relate to each other in terms of position, momentum, and quantum number correlation. In experiments, detectors capture data on thousands of

particles produced in high-energy collisions. Algorithms analyze this data to identify jets, which are groups of particles believed to originate from a single parton. Within each jet, the distribution of hadrons (types, energies, momenta) is measured. These distributions are what theorists aim to predict using fragmentation functions.

The evolution of fragmentation functions, $D_q^h(z, Q^2)$, with the energy scale Q^2 is governed by the DGLAP (Dokshitzer-Gribov-Lipatov-Altarelli-Parisi)[90, 89, 91] equations. These equations describe how the fragmentation functions change as the scale of the interaction Q^2 varies, incorporating the effects of parton splitting. For a parton of type q fragmenting into a hadron h, the DGLAP equations can be expressed as:

$$\frac{d}{d\ln Q^2} D_q^h(z, Q^2) = \sum_{q'} \int_z^1 dz' P_{q' \to q}\left(\frac{z'}{z}, \alpha_s(Q^2)\right) D_{q'}^h(z', Q^2) \tag{47}$$

where $P_{q' \to q}\left(\frac{z'}{z}, \alpha_s(Q^2)\right)$ are the splitting functions, z' is the fraction of the parent parton's momentum before splitting, and $\frac{z'}{z}$ represents the fraction of momentum transferred from the parent to the daughter parton. The sum over q' accounts for all possible parton types that can split into parton q. Splitting functions, $P_{q' \to q}(z)$, quantify the likelihood of a parton q' splitting into a parton q with a certain fraction of its momentum. These functions are calculated within perturbative QCD and are fundamental to modeling the evolution of parton distributions and fragmentation processes. For example, the splitting function for a gluon g splitting into a quark-antiquark pair ($q\bar{q}$) is determined by:

$$P_{g \to q\bar{q}}(z) = \frac{1}{2}\left(z^2 + (1-z)^2\right) \tag{48}$$

and for a gluon splitting into two gluons:

$$P_{g\to gg}(z) = 6\left[\frac{z}{(1-z)} + z(1-z) + \frac{(1-z)}{z}\right] \tag{49}$$

These equations illustrate the probabilistic nature of parton splitting and the redistribution of momentum during the fragmentation process, emphasizing the role of z in determining how a parton's momentum is partitioned among its fragmentation products. Through the integration over z' and the convolution with splitting functions, the DGLAP equations provide a framework for predicting the evolution of fragmentation functions across different energy scales.

3.5 PYTHIA

This is one of the most famous models for hadronization. In this model, the field between a quark and antiquark (or between quarks and gluons) is envisioned as a "string" that gets stretched as the partons move apart. When the string reaches a certain tension, it breaks, and new quark-antiquark pairs are produced, resulting in the formation of hadrons. The Lund String Model is indeed dynamic, as it provides a time-dependent description of the hadronization process, where quarks and gluons produced in high-energy particle collisions transition into hadrons. The model was first presented by Bo Andersson and his colleagues in the early 1980s. [92]. Di-quarks are theoretical constructs representing two quarks bound together. Within a baryon, a di-quark and a separate quark can be envisioned as being connected by strings that converge at a junction, a key feature for maintaining the baryon's stability and color neutrality. This Y-shaped configuration illustrates the complex interactions and the role of the strong force in holding the quarks together, ensuring the baryon's integrity. Fragmentation parameters within PYTHIA are finely adjusted based on experimental data to ensure that the simulated events closely mirror real-life particle collisions. This tuning process involves adjusting the parameters governing the probability distributions for how

strings break and the resultant energy and momentum distributions of the produced particles. The goal is to match the observed distributions of particles produced in high-energy collisions as accurately as possible. [93, 92]

3.5.1 Monash Tune

The MONASH 2013 tune, employed within the PYTHIA 8.3 framework [94] is a set of finely adjusted parameters that calibrate the Monte Carlo simulation to closely replicate experimental data from high-energy particle collisions. The MONASH 2013 tune was aimed at high momentum-transfer collisions using leading-order matrix elements coded in PYTHIA, emphasizing the hypothesis that hadronization is environment-independent. The parameters were primarily constrained using electron-positron e^+e^- data, especially from the Large Electron-Positron Collider(LEP) and SLAC Large Detector (SLD) for b-hadron specific observables. The tuning process involved adjusting physics parameters related to hadronization, final state radiation, and particle decays. It was noted that the initial-state parameters, such as those related to initial-state radiation, beam remnants, and multiparton interactions, were tuned using LHC data, with scaling obtained by including Tevatron data.

3.5.2 Color re-connection beyond the leading color

Color reconnection in final states refers to the rearrangement of color strings connecting partons. As the partons move apart, they pull out color flux tubes, which can break and reconnect in different configurations before hadronization. This reconnection can alter the potential energy landscape between the partons, leading to different hadronic final states. In the Leading Color (LC) limit, only the leading terms in $\frac{1}{\sqrt{N_c}}$ are kept in the perturbative expansion, which are the terms associated with the simplest color connections forming color-singlet objects. This approximation ignores subleading contributions that are more complex and less probable. In the limit of $N_c \to \infty$, with the strong coupling constant

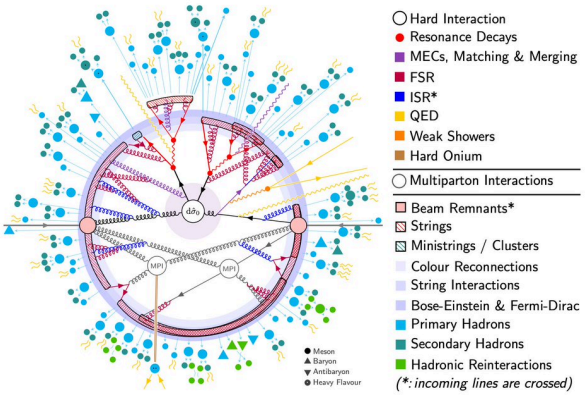

Figure 25: Diagram displaying stages in a high-energy hadron collision: ISR (Initial State Radiation), FSR (Final State Radiation), MPI (Multiple Parton Interactions), beam remnants, and the hadronization process including string formation, leading to the generation of primary and secondary hadrons [93].

$\alpha_s N_c$ held fixed, the perturbation series simplifies, and only planar diagrams dominate. In practical terms, especially in Monte Carlo event generators, this assumption allows for a more straightforward modeling of the parton shower and hadronization processes. The large N_c limit has also theoretical appeal due to its connection with the gauge/gravity duality (AdS/CFT correspondence), where a gauge theory at large N_c is related to a string theory in a higher-dimensional space. This duality provides profound insights into the non-perturbative regime of QCD-like theories. In PYTHIA, different modes such as mode0, mode2, mode3, use different time dilation parametrizations. This characteristic time indicates how much time is required for two strings or partons to impose leading color potential and form a flux tube. Mode0 and mode2 have relatively less constraint on the time, allowing more color reconnection, while mode3 has the tightest parameter.

3.6 Non universality of fragmentation functions

The observations on fragmentation functions reveal substantial disparities in charm baryon production in proton-proton pp collisions at the Large Hadron Collider versus those in

electron-positron (e^+e^-) collisions at LEP and B factories, and electron-proton (*ep*) collisions at HERA. [95] Figure 26 illustrates the relative abundance of charmed species (left) across collisions and charm pair production per event (right), which is slightly higher than the predictions at leading order (LO) in FONLL and next-to-next-to-leading order (NNLO). This suggests that the total charm pair production is not entirely consistent with the pQCD calculation. For instance, the PYTHIA multiparton interaction model can be employed, where charm is secondarily scattered from the rest of the partons in the nucleus, thus producing more charm pairs and enhancing the initial charm pair prediction in the hard scattering process.

A notably higher prompt Λ_c^+ baryon fragmentation fraction in *pp* collisions ($\sqrt{s} = 13$ TeV) is about three times that observed in e^+e^- and ep collisions, pointing to a marked enhancement of charm baryon production in the *pp* collision environment. Furthermore, Ξ_c^0 baryons, accounting for approximately 10% of total charm hadron production at midrapidity in LHC *pp* collisions—previously deemed negligible in e^+e^- and *ep* collisions—indicate a significant shift towards baryon production, consequently reducing the relative abundance of D mesons by about a factor of 1.5. The measurement of the Σ_c^{0+++} baryon fragmentation fraction in *pp* collisions reveals an approximately sevenfold increase compared to e^+e^- collisions, with Σ_c^{0+++} production comprising about 40% of the prompt Λ_c^+ baryon production at midrapidity, far exceeding measurements from e^+e^- collisions and PYTHIA 8 Monash tune simulations. These findings suggest a departure from the expected universality of fragmentation functions, underscoring the influence of the parton-rich *pp* collision environment on the hadronization process, distinct from that observed in e^+e^- and *ep* collisions, and highlighting the role of the surrounding partonic environment in shaping hadronization mechanisms without a significant dependency on the centre-of-mass energy. The production cross section of each charm hadron species was normalized by the p_T-integrated production cross sections for a selected group of measured charm hadrons, including D^0, D^+, D_s^+, J/ψ, Λ_c^+, Ξ_c^0, and

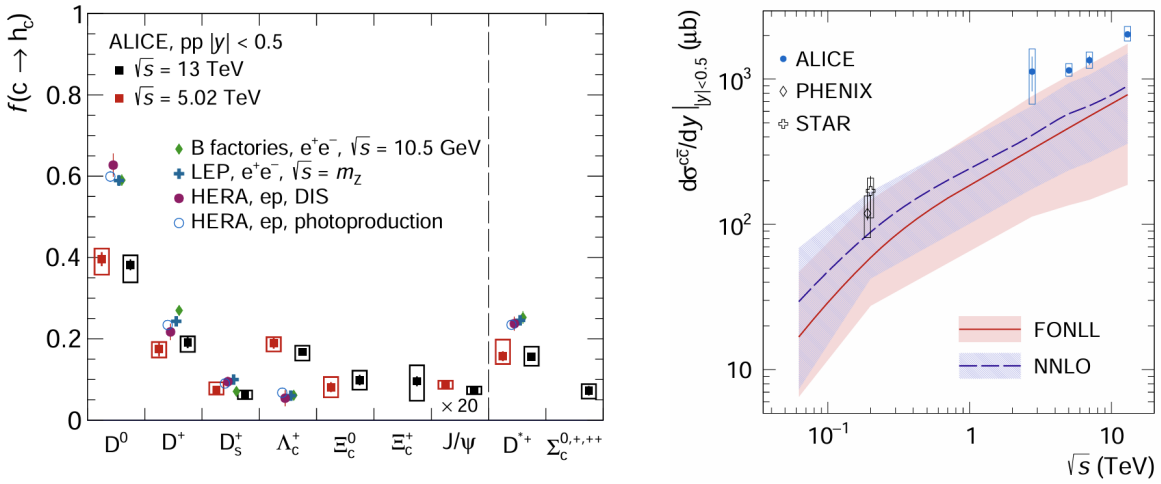

Figure 26: The self-normalized ratio of different species of charmed hadrons in ALICE collaboration and H1(left). The total charm production rate as a function of center-of-mass energy (right) [95]

Ξ_c^+. This normalization strategy is instrumental in enabling a comparative analysis of the production rates of different charm hadrons. An integral assumption underpinning this analysis is that all observed charm hadrons originate from a single charm quark pair produced in the initial collision. Furthermore, the study delineated the fragmentation fractions for D^{*+} mesons and Σ_c^{0+++} baryons due to their primary decay into D^0, D^+ mesons, and Λ_c^+ baryons, respectively—components already included in the normalization sum.

In proton-proton pp collisions, the significant multiplicity dependent enhancement of the Λ_c^+/D^0 ratio illuminates the discrepancy from the simpler fragmentation patterns observed in electron-positron (e^+e^-) collisions. [96]. The p_T differential Λ_c^+/D^0 ratio exhibits a clear enhancement with increasing multiplicity, a phenomenon quantified with a significance of 5.3σ as it is shown in the Figure 27 and Figure 28. The data points (represented by symbols) are compared to predictions from the PYTHIA 8.2 event generator with different tunes: Monash, CR-BLC Mode 0, Mode 2, and Mode 3. Additionally, the Canonical Ensemble Statistical Hadronization(CE-SH) model prediction by Y. Chen and M. He is shown. The Monash tune does not align well with the data, particularly for the Λ_c^+/D^0 ratio, and lacks a multiplicity

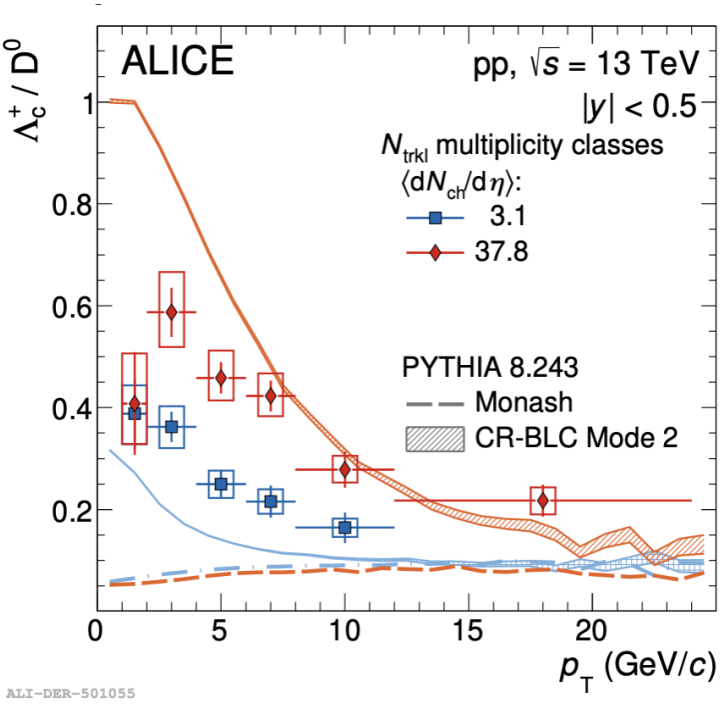

Figure 27: p_{T} differential $\Lambda_{\mathrm{c}}^{+}/\mathrm{D}^{0}$ ratio for pp collisions at 13 TeV and comparison to the PYTHIA,monash tune (dashed lines) and the color reconnection mode2 [96]

dependence. In contrast, the CR-BLC tunes exhibit a multiplicity dependence and are closer to the measured data, especially for the $\Lambda_{\mathrm{c}}^{+}/\mathrm{D}^{0}$ ratio, suggesting that these tunes are more effective in capturing the observed trends in the data. The CE-SH model appears to align with the low multiplicity class for the D_s^+/D^0 ratio but overestimates the high multiplicity data, while it reproduces the multiplicity dependence for the $\Lambda_{\mathrm{c}}^{+}/\mathrm{D}^{0}$ ratio. This behavior is observed for the light sector where the p_{T} differential ratio is shown in Figure 29 for Λ/K^0 ratio. This ratio is further enhanced for the Pb-Pb collisions and serve as one of the signatures for the quark gluon plasma. This trend suggests a potential common mechanism influencing both light and charm hadron formation, hinting at underlying processes in hadronic collisions that may affect the production rates and ratios of different hadron species. This deviation is profound because the e^+e^- results and the PYTHIA Monash tune, which are traditionally used to benchmark fragmentation processes, do not exhibit this multiplicity dependence. The observed enhancement in pp collisions suggests a scenario where the hadronization

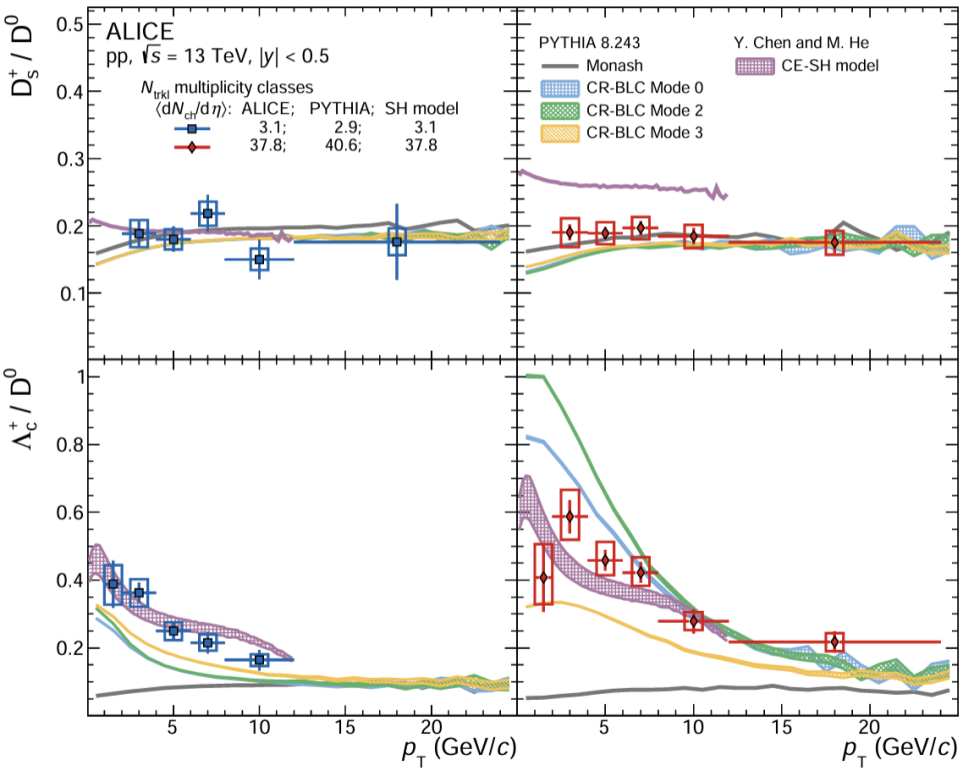

Figure 28: The plot from the paper compares the measured ratios of D_s^+/D^0 and Λ_c^+/D^0 as a function of transverse momentum (p_T) in pp collisions at $\sqrt{s} = 13$ TeV to various theoretical predictions. The upper panel shows the D_s^+/D^0 ratio and the lower panel shows the Λ_c^+/D^0 ratio [96]

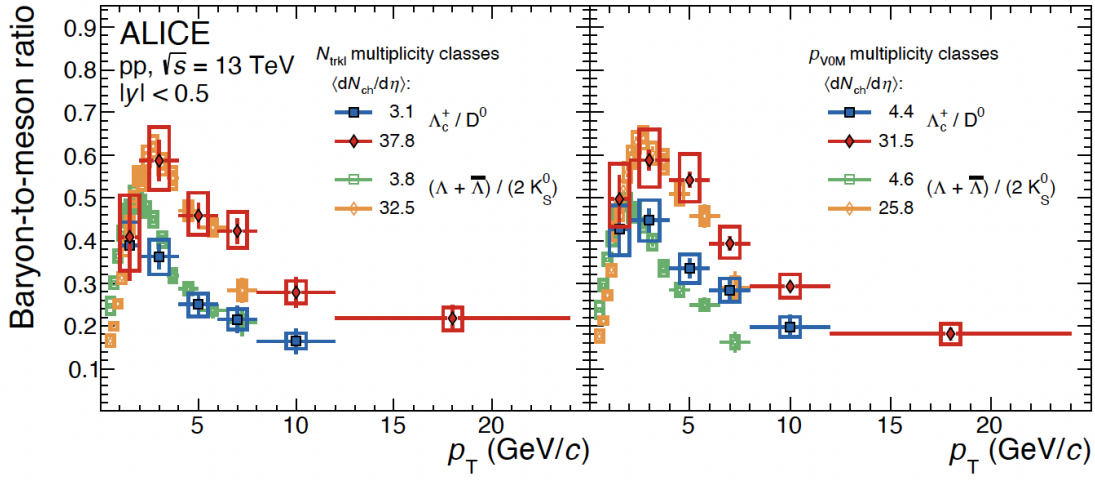

Figure 29: The figure presents the $p_T$differential baryon-to-meson ratios in proton-proton collisions at $\sqrt{s} = 13$ TeV for two sets of multiplicity classes. The left panel shows the Λ_c^+/D^0 and $(\Lambda + \bar{\Lambda})/(2K_S^0)$ ratios as a function of p_T for N_{trkl} multiplicity classes, while the right panel displays the same ratios for $V0M$ multiplicity classes.

mechanisms are influenced by the event's particle multiplicity, indicating that the system size, plays an important role in charm baryon production. Such findings challenge the assumed universality of fragmentation functions, positing that the particle production mechanisms in *pp* collisions are sensitive to the quantum chromodynamic environment, shaped significantly by the event's multiplicity. This sensitivity could lead to an understanding of the hadronization under different conditions, where the traditional models fall short in explaining the enhanced baryon-to-meson ratios observed in high-multiplicity *pp* collision events.

In-medium fragmentation refers to the process by which a high-energy parton (like a heavy quark) that propagates through a dense medium such as the Quark-Gluon Plasma, fragments into hadrons. This process is modified compared to fragmentation in vacuum due to the interactions between the propagating parton and the medium. These interactions can lead to energy loss (via radiative and collisional processes), momentum broadening, and changes in the color charge state of the parton, all of which can affect the fragmentation function and the resulting hadron yields and spectra. The specific mechanisms and effects of in-medium

fragmentation are complex and depend on the properties of the medium, the energy of the parton, and the type of parton (e.g., light quarks, heavy quarks). For heavy quarks like charm and bottom, the mass provides a natural cutoff for the radiative energy loss, making the study of their fragmentation in medium particularly interesting for understanding the properties of the QGP. The calculation of transport coefficients for heavy quarks (HQ) in a Quark-Gluon Plasma involves a combination of perturbative and non-perturbative approaches to account for the complex interactions within the medium. Heavy quarks, due to their higher mass, undergo a Brownian motion-like behavior when interacting with the lighter particles in the QGP. This interaction is described through the Langevin equation, which is a stochastic differential equation used to model the HQ's trajectory through the QGP, taking into account both the drag force and random kicks from the medium particles. The transport coefficients for heavy quarks in a quark-gluon plasma integrate perturbative and non-perturbative QCD effects to describe the quarks interactions with the medium. Perturbative methods calculate the quark's scattering and energy loss due to gluon radiation and collisions with high momentum transfer, while non-perturbative approaches address low-momentum interactions, including potential binding and long-range forces, influenced by the medium's color screening. These coefficients are essential for modeling the heavy quarks' diffusion and energy loss within the plasma, offering insights into the QGP's properties through comparisons with experimental data from heavy-ion collisions. Experimental data that can verify the validity of the calculations regarding transport coefficients include measurements of the nuclear modification factor R_{AA} and the elliptic flow v_2 for heavy-flavor particles, such as D mesons, in heavy-ion collisions.

Radial flow refers to the collective outward movement of particles from the collision center, influencing the particle spectra, particularly at low and intermediate p_T ranges. In high-multiplicity pp collisions, the presence of radial flow can lead to a harder p_T spectrum, meaning particles are pushed to higher momentum. This effect can cause the observed shift in the peak of the $\frac{\Lambda_c^+}{D^0}$ ratio to higher p_T values, as more particles gain momentum

from the collective expansion of the system. The shift in the peak of the Λ_c^+/D^0 ratio with multiplicity could reflect a transition from a scenario dominated by vacuum fragmentation (low multiplicity) to one where the recombination mechanisms (potentially influenced by radial flow) become more relevant (high multiplicity). This transition could indicate that, in high-multiplicity environments, the produced medium significantly affects the hadronization of charm quarks, leading to enhanced baryon production relative to meson production at lower p_T ranges. The simulations with the PYTHIA event generator were performed with the Monash and the CR-BLC tunes. The CR-BLC tunes, which incorporate different constraints on the allowed reconnections among color sources, effectively describe the Λ_c^+/D^0 ratio trends seen in the data, showing a clear multiplicity dependence and aligning with the observed decreasing trend in minimum-bias *pp* collisions at 5.02 and 13 TeV. In contrast, the Monash tune fails to reproduce the Λ_c^+/D^0 ratio and does not exhibit a multiplicity dependence. CR is a mechanism that allows for the rearrangement of color strings connecting partons before they hadronize. Different CR modes in PYTHIA alter how these strings are reconnected, impacting the final state particles' kinematics, multiplicities, and types. For example, CR can affect the production rates of baryons versus mesons, explaining enhancements in baryon-to-meson ratios observed in data, particularly in high-multiplicity environments. By comparing simulations with and without CR, physicists can gauge the impact of these non-perturbative QCD effects on collision outcomes. Junction formation allows for more complex reconnections of color strings that can lead to enhanced baryon production. During high-multiplicity events, the increased probability of string intersections raises the likelihood of forming such junctions, potentially explaining the observed increases in baryon-to-meson ratios and the specific enhancements of certain baryon species, like the Λ_c^+.

4 Analysis Strategy and Results

4.1 Data Set

A detailed description of the ALICE apparatus is available in the previous chapters. The analysis focuses on events that are captured in the minimum bias triggered data, identified by triggers kINT7 or Minimum Bias on the LHC2016 period. The CENTwSDD trigger is designed to select events with central collisions utilizing the Silicon Drift Detector (SDD), which is part of ALICE's Inner Tracking System. This trigger helps in isolating events that are significant for specific analyses, particularly those focused on high-density regions. On the other hand, the FAST trigger is used to rapidly select events based on predefined criteria, allowing for the efficient processing of data by prioritizing events that are likely to be of interest for further analysis. The FAST trigger is typically configured to recognize specific patterns or signatures in the detector that indicate a noteworthy event, such as high-momentum particles, unusual particle trajectories, or rare decay signatures. For this period, the data include the LHC16qt pass2 periods, utilizing trigger classes CENTwSDD and FAST, and an estimated number of events with MB trigger around $600 \cdot 10^6$.

Based on the 5.02 proton-lead (p-Pb) collision data, two specialized Monte Carlo simulations were produced using the PYTHIA+HIJING framework. The first, LHC21k1 (16q,t, CENTwSDD, fast), is a standard D-meson to hadron (D2H) Monte Carlo production enriched in heavy-flavour particles, ensuring the inclusion of a $c\bar{c}$ or $b\bar{b}$ quark pair, or a specific charmed hadron in the appropriate decay chain, in every proton-proton collision. For the simulation of particle interactions with the detector, GEANT3, transport software package, was employed, which models the passage of particles through the detector, accounting for various physical processes like energy loss, multiple scattering, and electromagnetic interactions. The second production, tagged as LHC21j6 or the $\Lambda_c^+ \rightarrow \mathrm{pK}^-\pi^+$ dedicated production, necessitates the presence of the targeted heavy-flavour hadron decay chain in each event. While the standard D2H production

supports D^0 analyses, the dedicated ones are essential for $\Lambda_c^+ \to pK_s^0 \to p\pi^+\pi^-$studies. Comparing the $\Lambda_c^+ \to pK^-\pi^+$ efficiencies derived from both the standard D2H and the dedicated productions, it was observed that their ratio consistently hovers around unity indicating the overal proceedure in both methods does not depend on the type of MC data set. (see Figure 30)

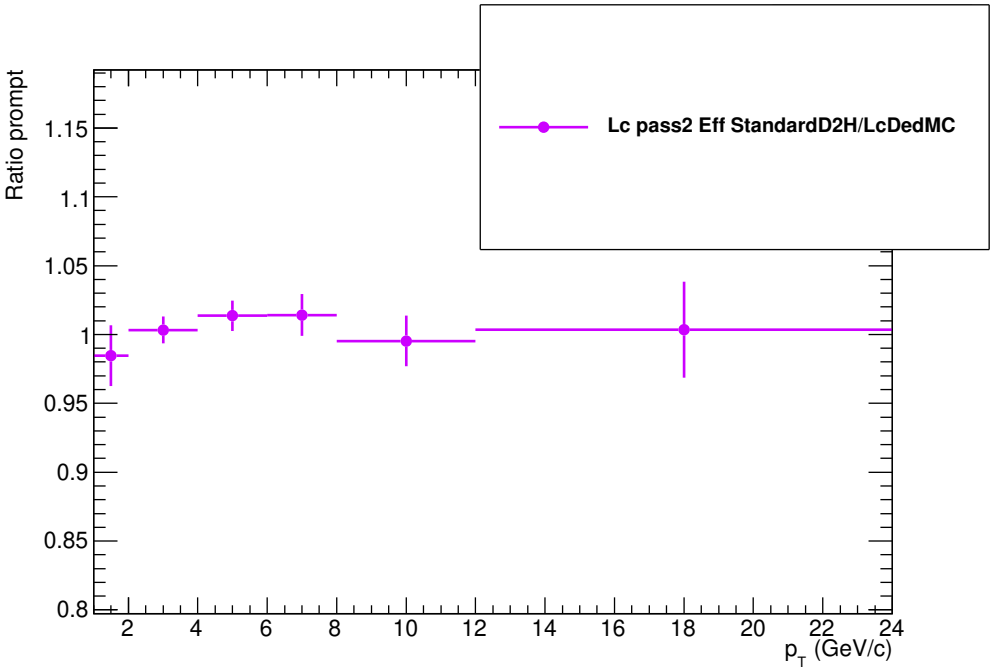

Figure 30: Acceptance-times-efficiency ratio of prompt $\Lambda_c^+ \to pK^-\pi^+$ computed with standard D2H MC and Λ_c^+ dedicated MC.

4.2 Event selection

In order to ensure the quality of the data used for analysis, a standard physics selection was implemented to discard background events. These undesired events are usually due to interactions of the particles in the beam with residual gases or the material of the beam pipe. The analysis only considered events where the interaction vertex, the point where particles collide and interact, was located within a 10 cm range along the beam's direction, denoted as $|z| < 10$ cm. When the primary interaction vertex could be determined using both the

signals from the Silicon Pixel Detector (SPD) and the Time Projection Chamber (TPC), the consistency of their z-position measurements was required. A "tracklet" refers to a pair of hits in the SPD that are assumed to be from the same particle (Figure 31), and these were used in a specialized algorithm designed to detect multiple interaction vertices within the same event, thus reducing the impact of "pile-up." Pile-up events are instances where more than one collision occurs within the same data acquisition window, leading to overlapping signals that can confound the analysis. If a second interaction vertex was identified with at least five associated tracklets, suggesting a pile-up, the event was excluded from the dataset. Further refinement was made based on the χ^2 value of the pile-up vertex and the distance between the primary collision vertex and any secondary pile-up vertex, weighted by their uncertainties. The χ^2 value, a statistical metric, assesses the likelihood that the observed distribution of hits corresponds to a genuine single-collision event. If this value exceeds a certain limit, it could indicate that the secondary vertex is likely due to pile-up and not a single collision.

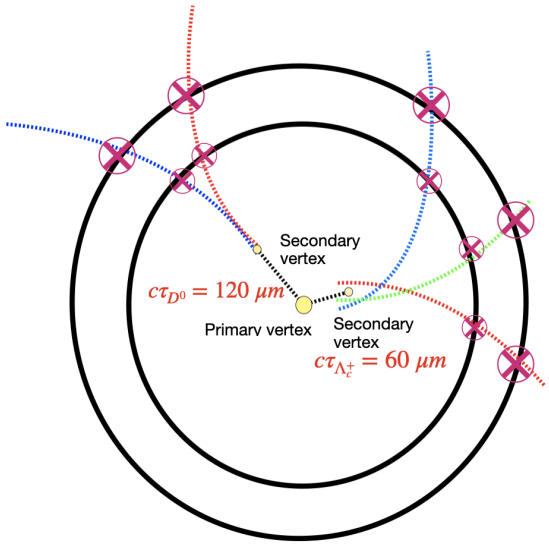

Figure 31: Illustration of tracklet reconstruction in SPD

4.3 Candidate selection

The D^0 and Λ_c^+ hadrons, as well as their respective antiparticles, were identified in the central rapidity area (which is essentially the region around the point where the particles are moving neither too forward nor backward from the collision point) based on their decays into charged hadrons. Specifically, the D^0 was reconstructed from its decay into a kaon and a pion ($D^0 \rightarrow K^-\pi^+$) with a branching ratio (BR) indicating the likelihood of this decay of $3.89 \pm 0.04\%$, and the Λ_c^+ from its decay into a proton, kaon, and pion ($\Lambda_c^+ \rightarrow pK^-\pi^+$) with a BR of $6.28 \pm 0.32\%$. To assemble these heavy-flavour hadron candidates, tracks were chosen that met the established quality criteria. These included having been processed through a fitting procedure with both the Inner Tracking System (ITS) and Time Projection Chamber (TPC), ensuring a precise trajectory reconstruction. Tracks were required to have a substantial number of hits in the TPC, specifically at least 70 out of a potential 159, and a high ratio (over 0.8) of these hits to the total possible hits, indicating a high-quality track. The goodness of the track fit in the TPC was evaluated by ensuring the chi-square per degree of freedom (χ^2/ndf) was less than 2, and at least two hits were recorded in the ITS, out of a possible six. Moreover, these tracks had to be within the rapidity range $|\eta| < 0.8$ and have a transverse momentum (p_T) greater than 0.3 GeV/c. The acceptance of D^0, the region where they are detected, decreases sharply outside a certain rapidity range, which changes with p_T. A p_T-dependent fiducial acceptance region was therefore established, varying from $|y_{lab}| < 0.5$ at low p_T to $|y_{lab}| < 0.8$ for $p_T > 5$ GeV/c, following a second-order polynomial function. The signal for the decays $D^0 \rightarrow K^-\pi^+$and $\Lambda_c^+ \rightarrow pK^-\pi^+$was selected based on the characteristic pattern of their decay: they tend to travel a detectable distance before decaying, unlike particles that don't decay. Particle Identification (PID) was employed, using the energy deposition in the TPC and the flight time measured by the Time of Flight (TOF) detector to differentiate between the kaons and pions. The TOF is particularly effective for identifying particles across a broad momentum range, up to 2 GeV/c. Candidates that met these criteria were then categorized into six transverse momentum bins for further analysis.

This binning strategy, although not very fine, was necessary to ensure that there were enough events (statistics) to accurately determine the number of heavy-flavour hadron decays for each category of event multiplicity. The boundaries for these p_{T} bins were set at 2, 4, 6, 8, 12, and 24 GeV/c. The analysis is based on an optimisation of the topological and kinematic cuts and of the PID selection applied to the candidates and daughters distributions. The yield extraction was performed using a particle selection strategy that has high efficiency and high statistical significance for the D^0 meson and $\Lambda_{\mathrm{c}}^+ \rightarrow \mathrm{pK}^-\pi^+$ baryon signal. The same topological variables as in previous analyses at $\sqrt{s} = 5.02$ TeV, 7 TeV, and 13 TeV were used. The D^0 measurement was performed by reconstructing pairs of tracks with the correct charge-sign combination, as detailed in the (see Table 32). The specific topological cuts applied to the Λ_{c}^+ baryon are summarised in Table 1, and those for the D^0 meson are found in Table 2. The selected events are grouped in sets of event multiplicity in classes of barrel and forward multiplicity. The former one employs the number of tracklets in the SPD detector, while the latter splits the events based on the V0M percentile multiplicity value of the two VZERO scintillator counters (VZERO A). A SPD tracklet is obtained by joining space points, aligned with the reconstructed primary vertex, on the two SPD layers.

Table 1: Geometrical and kinematic cuts used for the Λ_{c}^+ in p_T bins

p_T, Λ_c	p_T, p	p_T, K	p_T, π	DCA	dist12	σ_v	d_{length}	Cosθ_p
$2 < p_T < 3$	> 0.5	> 0.4	> 0.4	< 0.05	> 0.01	< 0.06	> 0.005	> 0
$3 < p_T < 4$	> 0.5	> 0.4	> 0.4	< 0.05	> 0.01	< 0.06	> 0.005	> 0
$4 < p_T < 6$	> 0.5	> 0.4	> 0.4	< 0.05	> 0.01	< 0.06	> 0.005	> 0
$6 < p_T < 8$	> 0.5	> 0.4	> 0.4	< 0.05	> 0.01	< 0.06	> 0.005	> 0
$8 < p_T < 12$	> 0.5	> 0.4	> 0.4	< 0.05	> 0.01	< 0.06	> 0.005	> 0
$12 < p_T < 24$	> 0.5	> 0.4	> 0.4	< 0.05	> 0.01	< 0.06	> 0.005	> 0

4.4 Z-vertex correction

The preliminary step in the data analysis involved adjusting the Silicon Pixel Detector (SPD) multiplicity counts, labeled as $N_{\mathrm{tracklets}}$. This correction was necessary to account for variations in the longitudinal collision vertex position distributions, or z-vertex profiles,

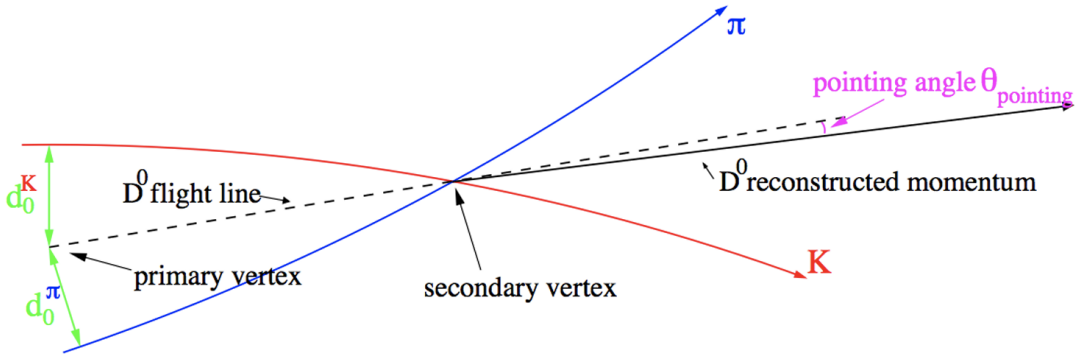

Figure 32: Schematic representation of heavy hadron decay. The primary vertex is the point where the hadron originally forms, while the secondary vertex represents the location where the hadron decays into a K and π particle. The K and π tracks are shown as positively and negatively curved lines, respectively, due to their charges in a magnetic field. The d_K^0 and d_π^0 denote the impact parameters for the K and π, which are the shortest distances from the primary vertex to their respective trajectories. The D^0 flight line is the dashed line that connects the primary and secondary vertices, indicating the path of the hadron before it decays. The D^0 reconstructed momentum vector is the combined momentum of the decay products, illustrated by the blue line. The pointing angle θ_{pointing} is the angle between the D^0 flight line and the D^0 reconstructed momentum vector. This angle is critical for determining the correctness of the decay reconstruction, with smaller angles generally indicating a more accurate reconstruction.

Table 2: Geometrical and kinematic cuts used for the D^0 in p_T bins.

$p_T\,(GeV/c)$	1-2	2-3	3-4	4-5	5-6	6-7	7-8	8-10	10-12	12-16	16-24	24-36
$\lvert\Delta M_{D^0}\rvert$ (MeV/c^2)	400	400	400	400	400	400	400	400	400	400	400	400
DCA(cm)	0.03	0.03	0.03	0.03	0.03	0.03	0.03	0.03	0.03	0.03	0.03	0.03
$\cos\theta^*$	0.8	0.8	0.8	0.8	0.8	0.8	0.8	0.9	0.9	1.0	1.0	1.0
p_TK	0.4	0.7	0.7	0.7	0.7	0.7	0.7	0.7	0.7	0.7	0.7	0.7
$p_T\pi$	0.4	0.7	0.7	0.7	0.7	0.7	0.7	0.7	0.7	0.7	0.7	0.7
$\lvert d_0^K\rvert$(cm)	0.1	0.1	0.1	0.1	0.1	0.1	0.1	0.1	0.1	0.1	0.1	0.1
$\lvert d_0^\pi\rvert$(cm)	0.1	0.1	0.1	0.1	0.1	0.1	0.1	0.1	0.1	0.1	0.1	0.1
$d_{0,K} \times d_{0,\pi}$(cm^2)	-0.00025	-0.0002	-0.00012	-0.00008	-0.00008	-0.00008	-0.00007	-0.00005	-0.00005	-	-	-
$\cos\theta_{point}$	0.8	0.9	0.9	0.85	0.85	0.85	0.85	0.85	0.85	0.85	0.85	0.85

noted during different data collection periods. Such variations can arise due to fluctuating operational conditions of the SPD—specifically the differing statuses of SPD pixels across various runs. To mitigate these effects, the data was categorized into four distinct groups. Each group was selected based on the similarity in the distribution pattern of $N_{\text{tracklets}}$ within the respective sample. In the ongoing analysis using the second pass of data, the V0A multiplicity estimator is exclusively utilized. In this context, the term "profile" describes the

observed distribution of $N_{\text{tracklets}}$ with respect to the z-vertex. It serves as a diagnostic tool to evaluate the uniformity and effectiveness of the SPD's pixel response across its spatial range. Correcting for the profile is essential to ensure that the SPD's operational variations do not skew the multiplicity measurements, thus providing an accurate representation of the underlying physics events.

4.5 Multiplicity

The V0M percentile is a comparative measure established for each run of the experiment. It is derived by dividing the amplitude of the V0M signal by its average value and then splitting this normalized distribution into segments that each contain a specific percentage of the total number of events. An event is then assigned a percentile rank based on the segment in which it falls, ranging from 0 to 100 percent. This process is performed for each run individually rather than for the entire dataset at once. This run-by-run calibration accounts for any potential changes in the V0 detector's performance over time, such as gradual wear and degradation, ensuring that the percentile rankings remain consistent throughout the duration of data collection. The V0 detector itself consists of two parts: V0A and V0C. These are arrays of scintillator counters located on opposite sides of the interaction point and are used to measure the multiplicity of particles. The V0M signal is a combination of signals from V0A and V0C, providing a measure of the total particle multiplicity in an event. By using both V0A and V0C, the V0M gives a broader view of the particles produced in the collision. Tables 3 and 4 present the specific multiplicity bins used in the analysis, as well as the corresponding average charged particle multiplicity, denoted by $\langle \mathrm{d}N_{\mathrm{ch}}/\mathrm{d}\eta \rangle$, and the triggers employed to collect events within each multiplicity category. The term INEL > 0 refers to a class of events where at least one charged particle is produced. In this analysis, it specifically means that there is at least one particle-producing interaction that results in at least one tracklet being reconstructed by the SPD in the pseudorapidity interval $|\eta| < 1$. When using the SPD tracklet count as the multiplicity estimator, this condition is implicitly considered

by starting the tracklet count at one instead of zero. Employing the INEL > 0 selection has become standard practice in recent ALICE analyses involving multiplicity, as it helps to harmonize experimental results with theoretical models and ensures consistency across different analyses. It is a way to account for about 75% of the total inelastic cross-section, which is a measure of the probability that any kind of inelastic interaction occurs during a collision.

Table 3: SPD tracklet multiplicity bins, along with the $\langle \mathrm{d}N_{\mathrm{ch}}/\mathrm{d}\eta \rangle$ for $|\eta| < 1$

$\mathrm{N}_{tracklets}$	$\langle \mathrm{d}N_{\mathrm{ch}}/\mathrm{d}\eta \rangle$	trigger
INEL>0 ($[1, \infty]$)	$17.35^{+0.10}_{-0.08}$	MB
$[1, 40]$	8.5 ± 0.02	MB
$[40, 65]$	15 ± 0.01	MB
$[65, 200]$	46 ± 0.07	MB

Table 4: V0M amplitude bins, along with the $\langle \mathrm{d}N_{\mathrm{ch}}/\mathrm{d}\eta \rangle$

V0M [%]	$\langle \mathrm{d}N_{\mathrm{ch}}/\mathrm{d}\eta \rangle$	trigger
$[0, 100]$	$17.35^{+0.10}_{-0.08}$	MB
$[60, 100]$	$6.8^{+0.07}_{-0.05}$	MB
$[10, 60]$	$21.04^{+0.18}_{-0.15}$	MB
$[0, 10]$	$40.5^{+0.18}_{-0.15}$	MB

4.5.1 Conversion of SPD tracklets to $\mathrm{d}N_{\mathrm{ch}}/\mathrm{d}\eta$

The number of SPD tracklets, which acts as an estimator for the multiplicity detected by the Silicon Pixel Detector (SPD), is not a fundamental physical quantity but rather a reflection of the current state of the detector, which may change due to the SPD's aging. As such, multiplicity classifications based on $N_{\mathrm{tracklets}}$ require conversion to a standard physical measure to facilitate comparisons outside of the specific conditions of the ALICE experiments. To achieve this, a procedure has been established to recalibrate the $N_{\mathrm{tracklets}}$, after adjusting for variations in the longitudinal collision position (Z_{vtx}), into the absolute number of primary charged particles, N_{charged}. The recalibration process incorporates comprehensive Monte Carlo simulations that mirror the experimental conditions during the same data-taking periods,

using the exact run lists as the data analysis for each period. The procedure for making Z_{vtx}-related adjustments to $N_{\mathrm{tracklets}}$ aligns with the methodology employed in previous ALICE research, specifically in the study of D-meson production in p-Pb collisions as a function of event multiplicity [97].

4.5.2 Removal of daughter tracks

The decay tracks from the D^0 or Λ_{c}^+ can affect both (i) the tally of tracklets, altering the estimated multiplicity, and (ii) the calculation of the primary vertex's location, which in turn impacts the resolution of the vertex position and the geometrical criteria employed for selecting D^0 meson candidates. In this analysis, the decay tracks were not considered in the determination of the primary vertex and were also omitted from the multiplicity assessment. Consequently, any tracklets originating from the D^0 mesons were deducted from the total $N_{\mathrm{tracklets}}$ count. In summary, D^0 mesons and their decay products are excluded from the multiplicity count to ensure accurate event characterization. This exclusion prevents artificial inflation of the multiplicity, avoids analysis bias, maintains the integrity of the primary vertex determination, and ensures that the multiplicity reflects only the initial collision's complexity, thereby providing a more precise and unbiased dataset for analysis.

4.6 MC reweighting

The efficiency of reconstructing and selecting heavy-flavour hadrons, particularly those that form a secondary vertex, is influenced by the charged particle multiplicity in the collisions. This is because the resolution of the primary vertex improves with higher multiplicities. Consequently, the accuracy of selection variables that rely on the primary vertex position—such as the track's impact parameter, the decay length of the particle, and the pointing angle—also enhances as the multiplicity increases. This improvement introduces a dependency of the selection efficiency on multiplicity. Therefore, it is crucial for Monte Carlo (MC) simulations to accurately reflect the multiplicity distribution observed in real

data. However, should the MC simulations fail to adequately represent the barrel multiplicity, it becomes necessary to re-weight the tracklet number ($N_{\text{tracklets}}$) distributions in the MC to match those from the data. Additionally, since the V0M percentile is not calibrated within the MC simulations, analyses that utilize as a multiplicity estimator must also apply re-weighting to the MC events based on the barrel multiplicity. This is illustrated in Figures 33, 34 for the SPD tracklets, and in Figures 35, 36 for the V0M percentile. To derive the necessary MC weights, a set of procedures is followed:

1. Full event selection on MC and data (no selection on the multiplicity estimator),
2. Select only events in MC and data with at least one candidate by applying all candidate selection criteria and require the candidate invariant mass to be at most 20 MeV/c^2 off the PDG value,
3. Extract normalised n_{trkl}distribution for MC and data,
4. Divide obtained distribution from data by the MC one to obtain event weights ω_i in each barrel multiplicity bin i.

Then for each slice the above procedure is applied, resulting in one set of weights per multiplicity bin. This results in an efficiency correction according to

$$(\text{Acc} \times \varepsilon)_{\text{corr}} = \frac{\sum_i N_{\text{sel},i}\omega_i}{\sum_i N_{\text{gen},i}\omega_i} \tag{50}$$

for barrel multiplicity bins i where $N_{\text{sel},i}$ and $N_{\text{gen},i}$ are the reconstructed+selected and generated number of candidates in bin i in MC (see Figure 36), respectively. The effect on final efficiency is negligible.

4.7 Analysis Strategy

The final result of these analyses is the per-event corrected yield within each multiplicity class for the observed heavy-flavour hadrons. The approach adopted for this analysis remains

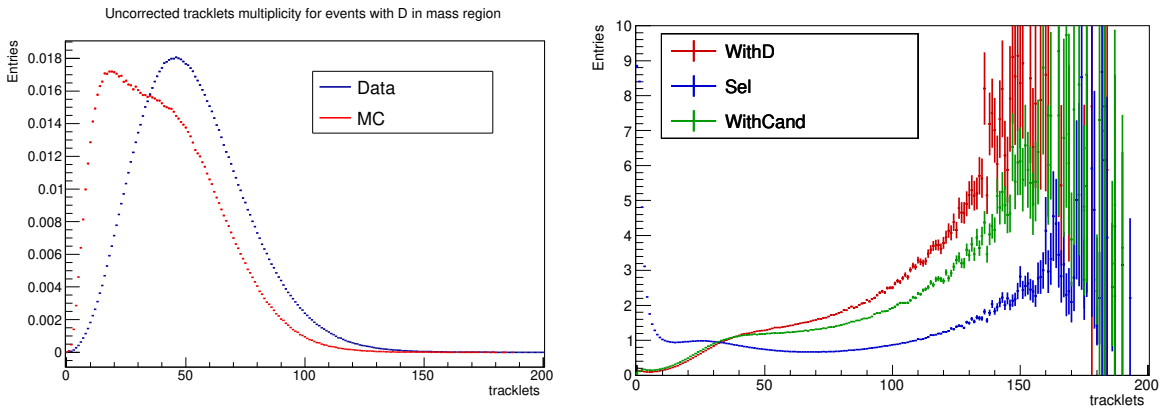

Figure 33: D^0 $N_{\text{tracklets}}$ distribution in data and MC(left). Multiplicity weights as a ratio of $N_{\text{tracklets}}$ distribution in data/MC for all three different selections(right). Three types of weights are shown: events with D^0 (red), events with one D^0 in a mass region (green), all events (blue). This analysis uses the weights with a D^0 in meson in the mass region.

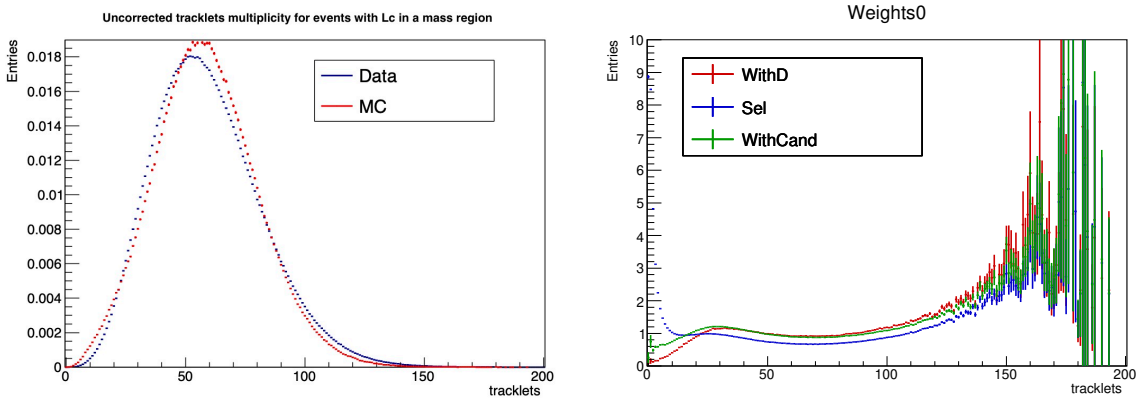

Figure 34: Λ_c^+ $N_{\text{tracklets}}$ distribution in data and MC(left). Multiplicity weights as a ratio of $N_{\text{tracklets}}$ distribution in data/MC for all three different selections(right). Three types of weights are shown: events with D^0 (red), events with one Λ_c^+ in a mass region (green), all events (blue). This analysis uses the weights with a Λ_c^+ in meson in the mass region.

consistent across all hadron species. Once the hadron candidates have been selected across different multiplicity and p_T bins—a process henceforth described as 'signal extraction'—their invariant mass distributions are fitted to separate the 'raw' signal from the background yields. This fit's specific shape is unique to each hadron type and is detailed in the sections discussing the precise fit procedures. The raw hadron yield per event is then normalized by the number of selected events after applying the necessary corrections to acquire the relative yield for each hadron.

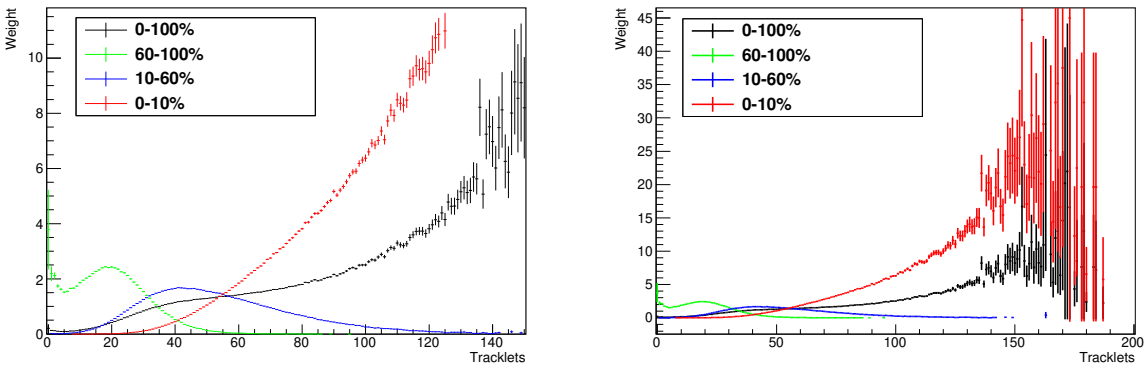

Figure 35: Λ_c^+ multiplicity weights in V0M estimator classes (left). D^0 multiplicity weights in V0M estimator classes (right)

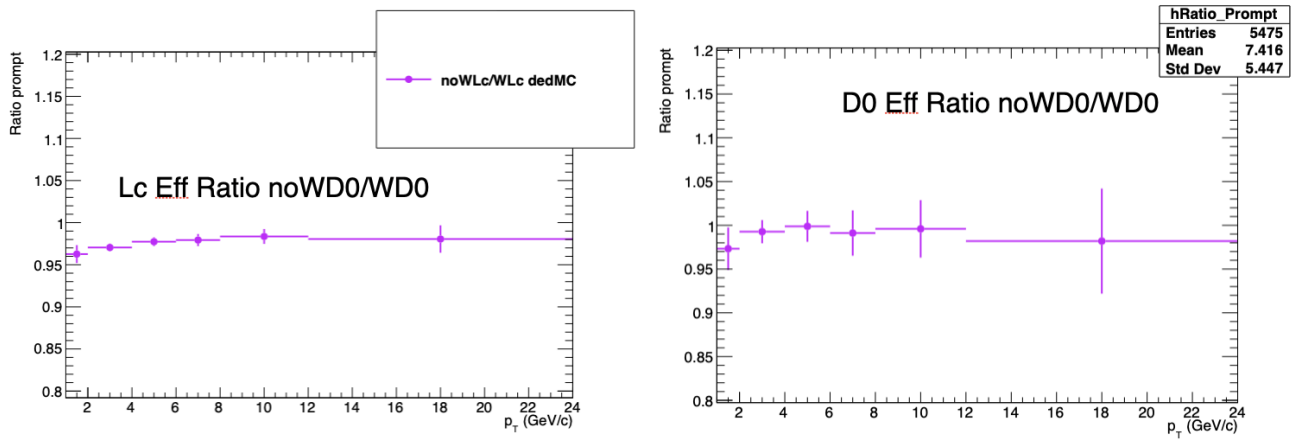

Figure 36: MC efficiency for Λ_c^+(left) and D^0 (right) for the MB case, with/without weights

$$\left.\frac{\mathrm{d}N_{\mathrm{mult}}^{\mathrm{hadron}}/\mathrm{d}p_{\mathrm{T}}}{N_{\mathrm{mult}}^{\mathrm{ev}}}\right|_{-0.96<y<0.04} = \frac{f_{\mathrm{prompt}}(p_{\mathrm{T}}) \cdot \epsilon_{\mathrm{trigger}} \cdot \frac{1}{2} N_{\mathrm{mult}}^{\mathrm{hadron,raw}}(p_{\mathrm{T}})_{|y|<y_{\mathrm{fid}}}}{N_{\mathrm{mult}}^{\mathrm{ev}} \Delta y \Delta p_{\mathrm{T}} (Acc \times \epsilon)_{\mathrm{prompt}}(p_{\mathrm{T}})(\mathrm{BR})} \tag{51}$$

where $N_{\mathrm{mult}}^{\mathrm{hadron,raw}}(p_T)$ is the value of the raw yield (sum of particles and antiparticles) extracted from the fit to the candidate invariant-mass distribution in the corresponding $p_{\mathrm{T}}$and multiplicity interval in the fiducial rapidity range ($|y| < y_{\mathrm{fid}}$). It is corrected for the beauty-hadron decay (feed-down) contribution ($f_{\mathrm{prompt}}(p_{\mathrm{T}})$) and the trigger efficiency ($\epsilon_{\mathrm{trigger}}$), divided by the acceptance-times-efficiency for prompt hadrons, $Acc \times \epsilon$, and divided by a

factor of two to obtain the charge (particle and antiparticle) averaged yields. The yields were divided by the decay channel branching ratio (BR), the p_{T}interval width (Δp_{T}), and the rapidity coverage (Δy), and the number of events in each multiplicity bin ($N^{\mathrm{ev}}_{\mathrm{mult}}$). In p-Pb collisions, the rapidity coverage is selected to be from $y = -0.96$ to $y = 0.04$ due to the inherent asymmetry between the proton and lead nuclei, contrasting with pp collisions, which, being symmetric, allow for a balanced rapidity coverage from $y = -0.5$ to $y = 0.5$. The chosen rapidity range in p-Pb collisions is important for studying the effects induced from the lead (Pb) side, specifically to investigate the impact of the Pb nucleus on particle production. This focus is essential for understanding how the larger mass and size of the Pb nucleus compared to the proton influence the dynamics of the collision and the distribution of resulting particles.

4.8 $\mathrm{D}^0 \to \mathrm{K}^-\pi^+$ raw yield extraction

Panels of the Figures 37 show the fitting of invariant mass distributions across six p_{T} bins for D^0, showcasing data from the minimum bias sample in p-Pb collisions gathered in 2016. The process of extracting raw yields for D^0 encompasses considering the invariant mass distribution candidates, which include $\mathrm{D}^0 \to \mathrm{K}^-\pi^+$ and $\bar{\mathrm{D}}^0 \to \mathrm{K}^+\pi^-$ decays. The term 'reflection' refers to the combination of candidates with incorrect mass hypothesis assignments. Reflection distributions, discernible in MC simulations, allow for the differentiation between signal, background, and reflection D^0 candidates. These distributions are modeled using a function comprising two Gaussian distributions. The derived functions from this modeling are integrated into the standard fitting process as a reflection template, scaled according to the signal magnitude observed in the dataset. The proportion of reflection to signal D^0 is determined via Monte Carlo studies. The impact on signal extraction accuracy, comparing scenarios with and without the reflection template, is found to be within the 1–4 % of the raw yield. Figure 38 shows the signal extraction performance for the D^0

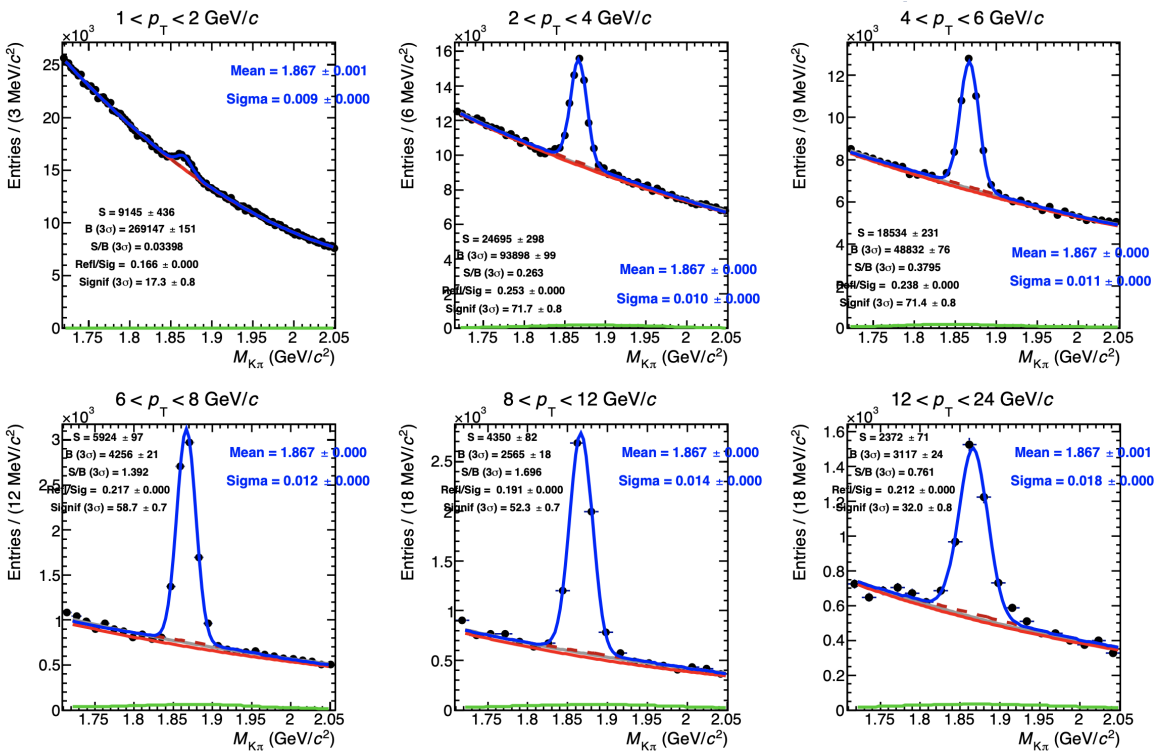

Figure 37: $D^0 \to K^-\pi^+$ mass spectra in pPb at 5.02 TeV collected in 2016, in the minimum bias triggered sample. The fits include the reflection contributions (green).

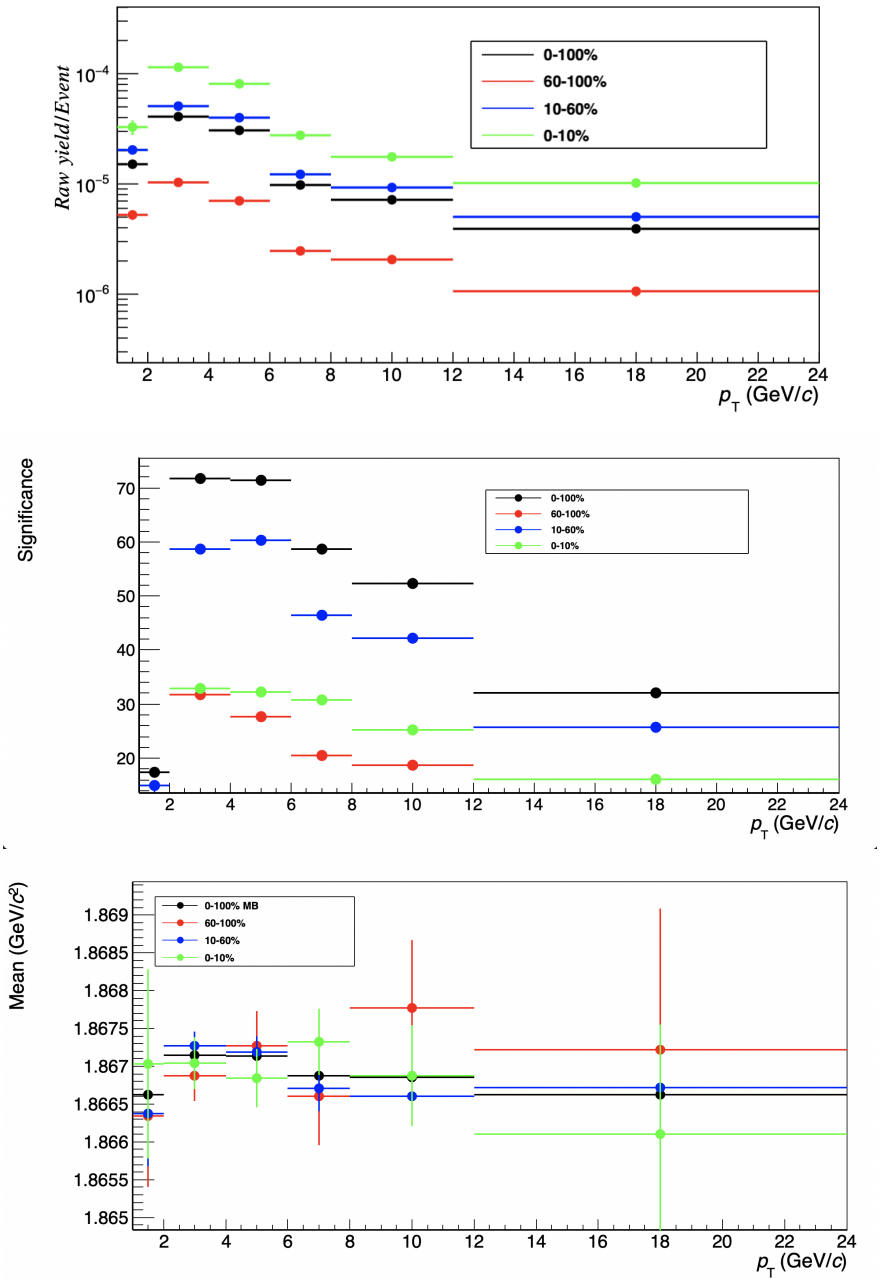

Figure 38: Performance of the D^0 yield extraction in the V0A percentile bins. On the top we show the raw yield/events, on the middle the extracted significance and on the bottom the mean mass. The width of the Gaussian peak is fixed to the MB case.

4.9 $\Lambda_c^+ \to pK^-\pi^+$ raw yield extraction

The extraction of $\Lambda_c^+ \to pK^-\pi^+$ yields across various p_T bins involved fitting the invariant mass distribution. The background of $\Lambda_c^+ \to pK^-\pi^+$ was modeled using a second-order

polynomial function, while the signal was fitted with a Gaussian function. In the analysis of multiplicity-dependent spectra, the sigma value was fixed to that derived from Monte Carlo (MC) (see Figure 40) simulations for the minimum bias (MB) scenario. The mass spectra section displays different fitting curves: the background is represented by the red curve, the total fit by the blue curve, and the dashed gray line corresponds to the fit of the sidebands exclusively. The $\Lambda_c^+ \to pK^-\pi^+$ extraction was conducted using the same p_T bins as those in the D^0 analysis. The mass spectra for the minimum bias triggered sample are illustrated in Figure 39, Figure 40 for MB, 41 for SPD multiplicity bins and 42 for V0M multiplicity bins offers an assessment of the $\Lambda_c^+ \to pK^-\pi^+$ yield extraction performance, showcasing the Gaussian signal peak's mean and sigma in both data and MC, along with the signal/event, background/event, and significance.

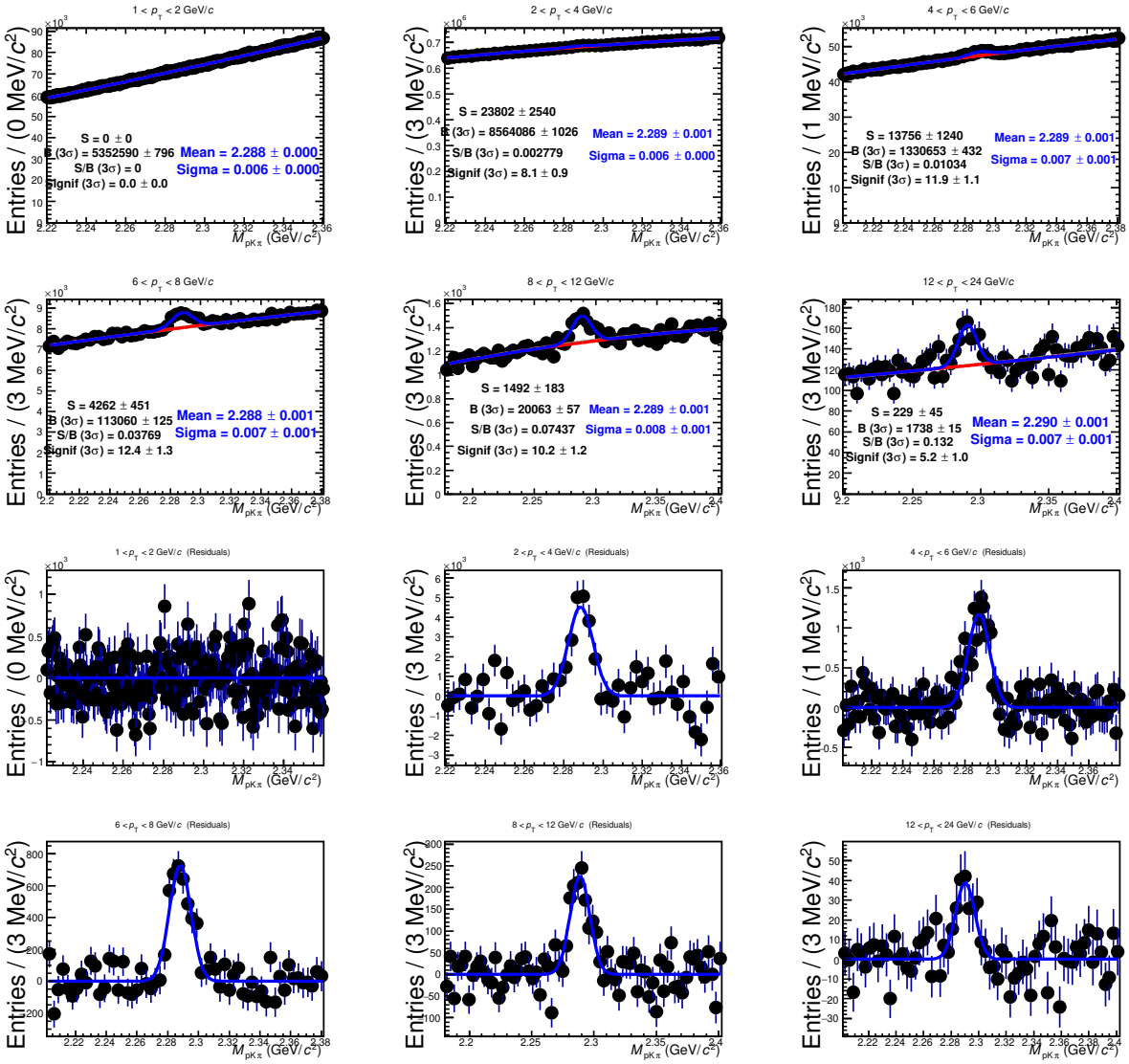

Figure 39: $\Lambda_c^+ \to pK^-\pi^+$ mass spectra in p–Pb at 5.02 TeV collected in 2016, in the minimum bias triggered sample. The residuals are shown in the bottom panels.

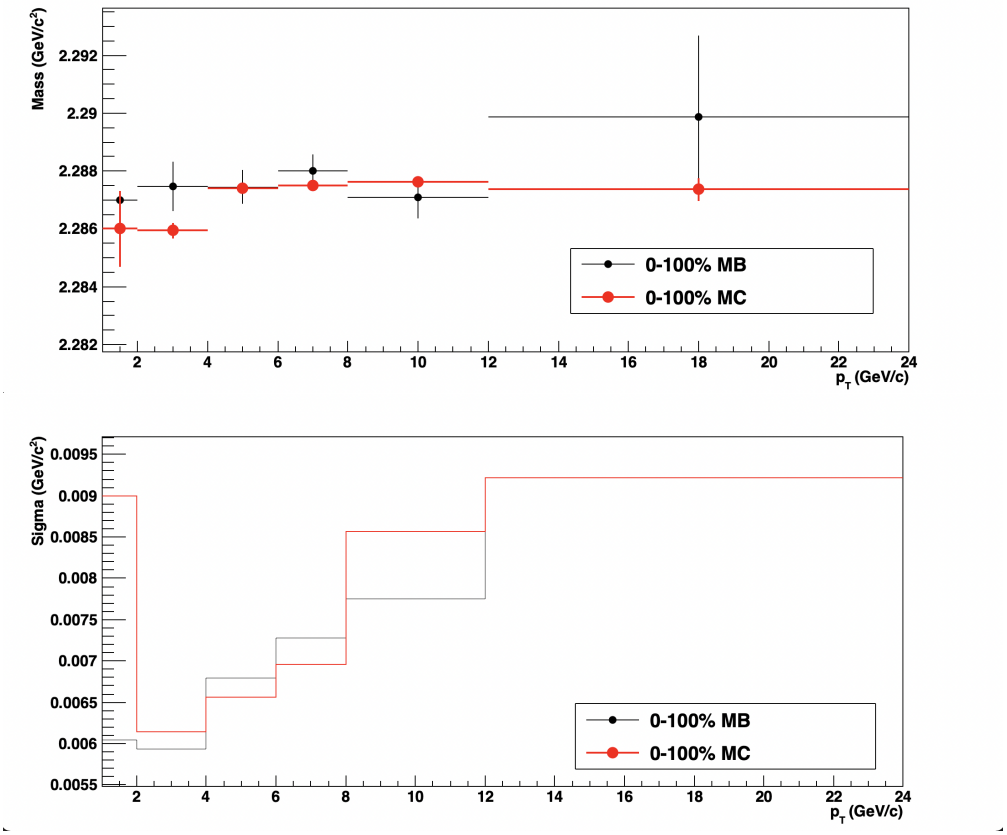

Figure 40: Performance of the $\Lambda_c^+ \to pK^-\pi^+$ yield extraction in p–Pb 5.02 TeV. A comparison of the extracted mean (top), extracted MC width of the Gaussian peak, and the width of the data peak are shown(bottom)

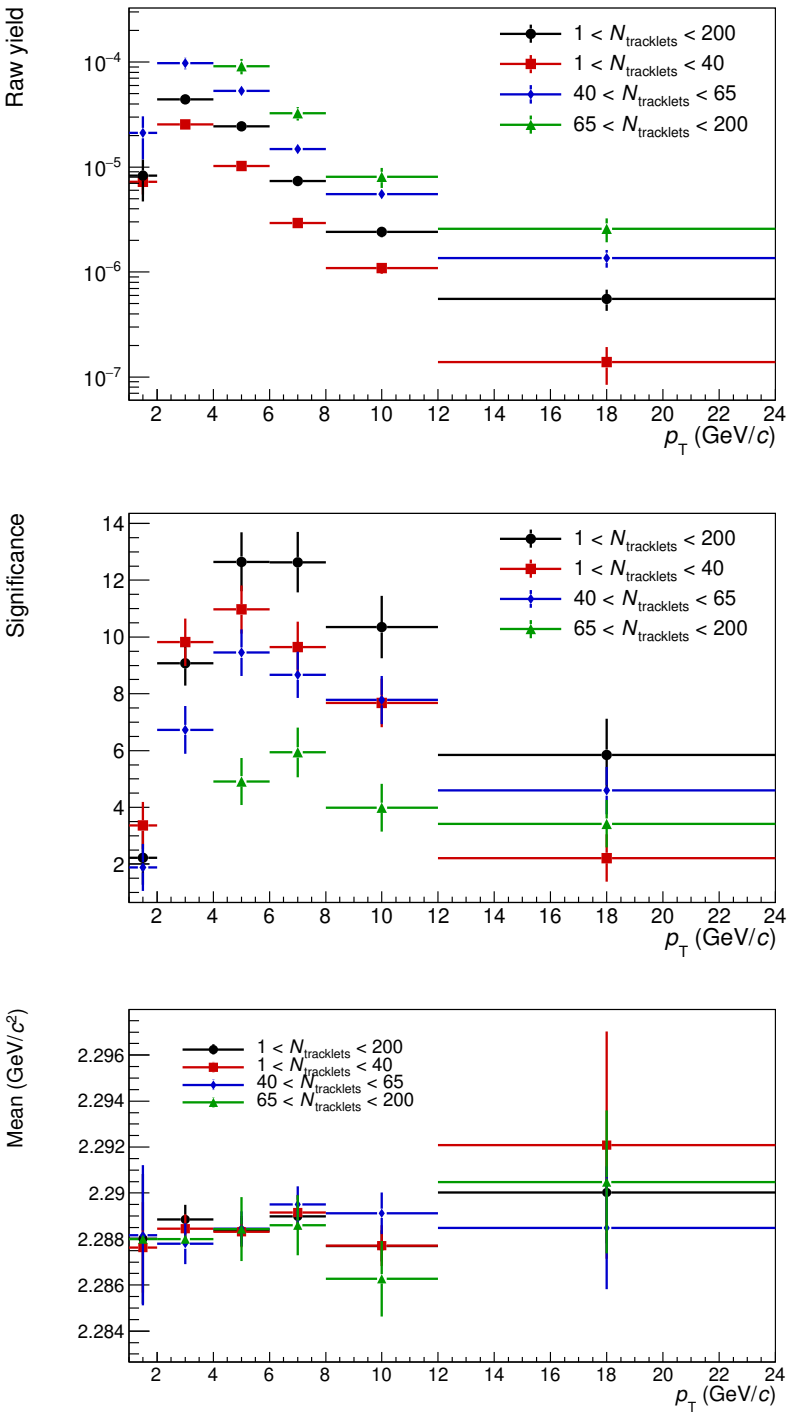

Figure 41: Performance of the $\Lambda_c^+ \rightarrow pK^-\pi^+$yield extraction in the SPD tracklet bins for pPb 5.02 TeV. On the Top we show the raw yield per event, on the bottom the extracted significance and the mean mass can be observed. The width of the Gaussian peak is fixed to the MB case, as shown in Figure. 40.

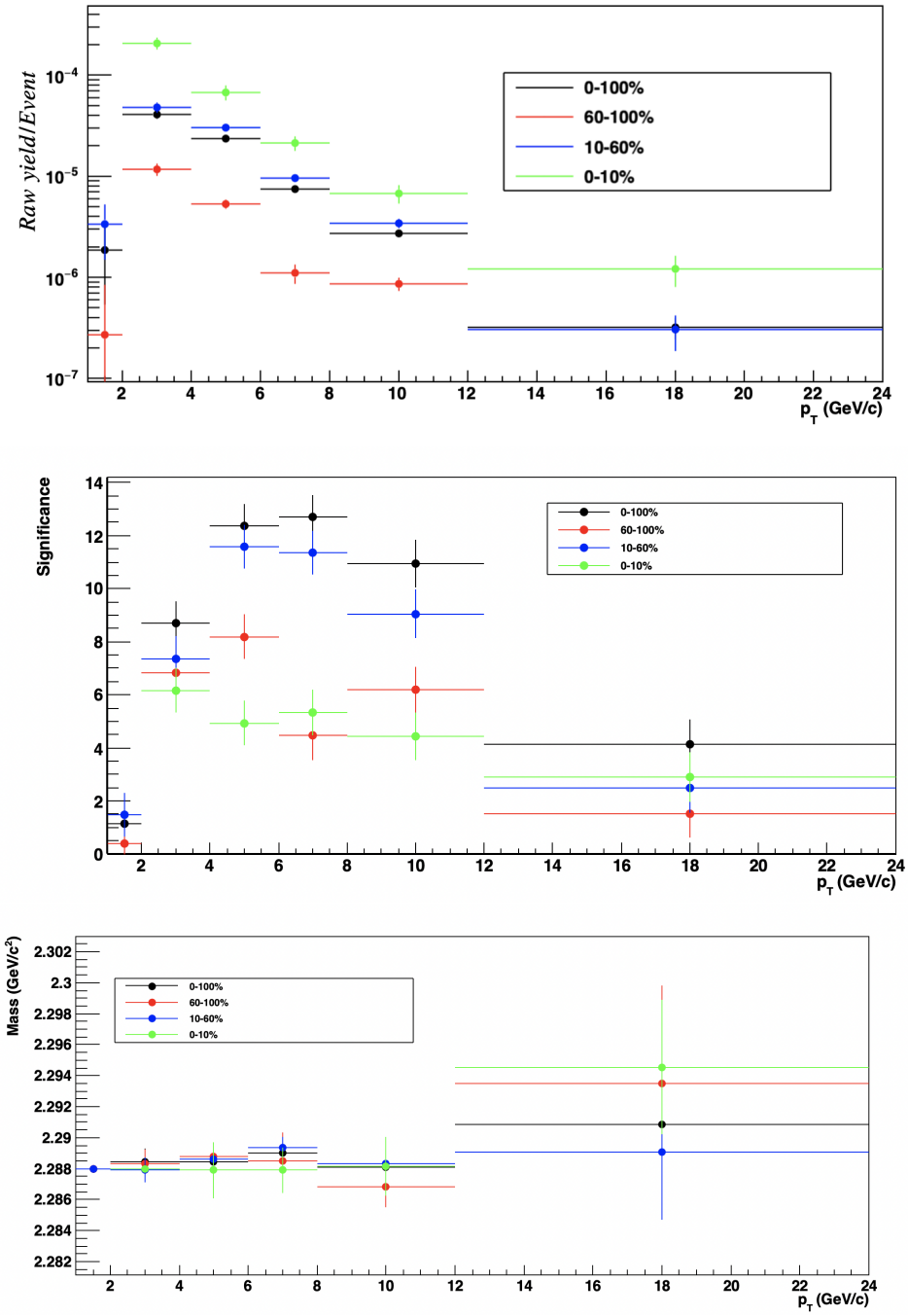

Figure 42: Performance of the $\Lambda_c^+ \to pK^-\pi^+$ yield extraction in the V0A percentile bins. On the top we show the raw yield per event, on the middle the extracted significance and on the bottom the mean mass. The width of the Gaussian peak is fixed to the MB case, as shown in Figure. 40.

4.10 Efficiency and acceptence

The extracted raw counts of D^0 mesons and Λ_c^+ baryons in each p_T and multiplicity interval underwent corrections for both the reconstruction and selection efficiency as well as for the acceptance. These correction factors were determined using Monte Carlo (MC) simulations. It is important to note that the reconstruction and selection efficiency is influenced by the event's charged particle multiplicity. This is because the precision of the primary vertex and the topological selection variables' resolution increase at higher multiplicities. Consequently, the accuracy of selection variables utilizing the primary vertex's position (such as the track impact parameter, particle decay length, and pointing angle) also enhances with an increase in multiplicity, leading to a dependency of the selection efficiency on multiplicity. Therefore, to address this, the MC multiplicity distributions are adjusted as elaborated in the MC weighting section. Efficiency measurement in the ALICE experiment at different stages of data reconstruction and selection includes: 'Vertex' refers to primary vertex reconstruction efficiency, 'Refit' denotes efficiency after track refitting with vertex constraints, 'Reconstructed' represents efficiency following full event reconstruction, 'RecAcc' indicates efficiency with reconstruction acceptance criteria applied, 'RecoITSClus' includes the ITS cluster requirement, 'RecoCut' corresponds to efficiency after applying specific reconstruction cuts, and 'RecoPID' is efficiency post particle identification cuts. The correction factors for acceptance and efficiency, denoted as (Acc $\times$ ϵ), were calculated for the hadronic decays of D^0meson and Λ_c^+ baryons featured in this study, utilizing Monte Carlo simulations of proton-proton (pp) collisions generated with the PYTHIA 8 event generator. The simulated particles were navigated through the detector setup with the GEANT3 transport software. These simulations incorporated the luminous region's distribution and replicated the operational conditions of the ALICE detectors, including active channels, gain, noise levels, and alignment. The Monte Carlo productions employed for determining the (Acc $\times$ ϵ) factors exclusively processed events that contained a $c\overline{c}$ or $b\overline{b}$ quark pair, which were then propagated through the detector system and reconstructed. Additionally, in these simulations, D^0 mesons and Λ_c^+

baryons were specifically programmed to decay through the hadronic channels under analysis. The efficiency calculations were conducted distinctly for promptly produced charmed particles and those originating from B-meson decays, also known as feed-down. Figure 43 are respective $(\mathrm{Acc} \times \epsilon)$ for D^0 and Λ_c^+. Figures 44, 45, and 46 show the ratio of $(\mathrm{Acc} \times \epsilon)$ for each centrality class to minimum bias ratio.

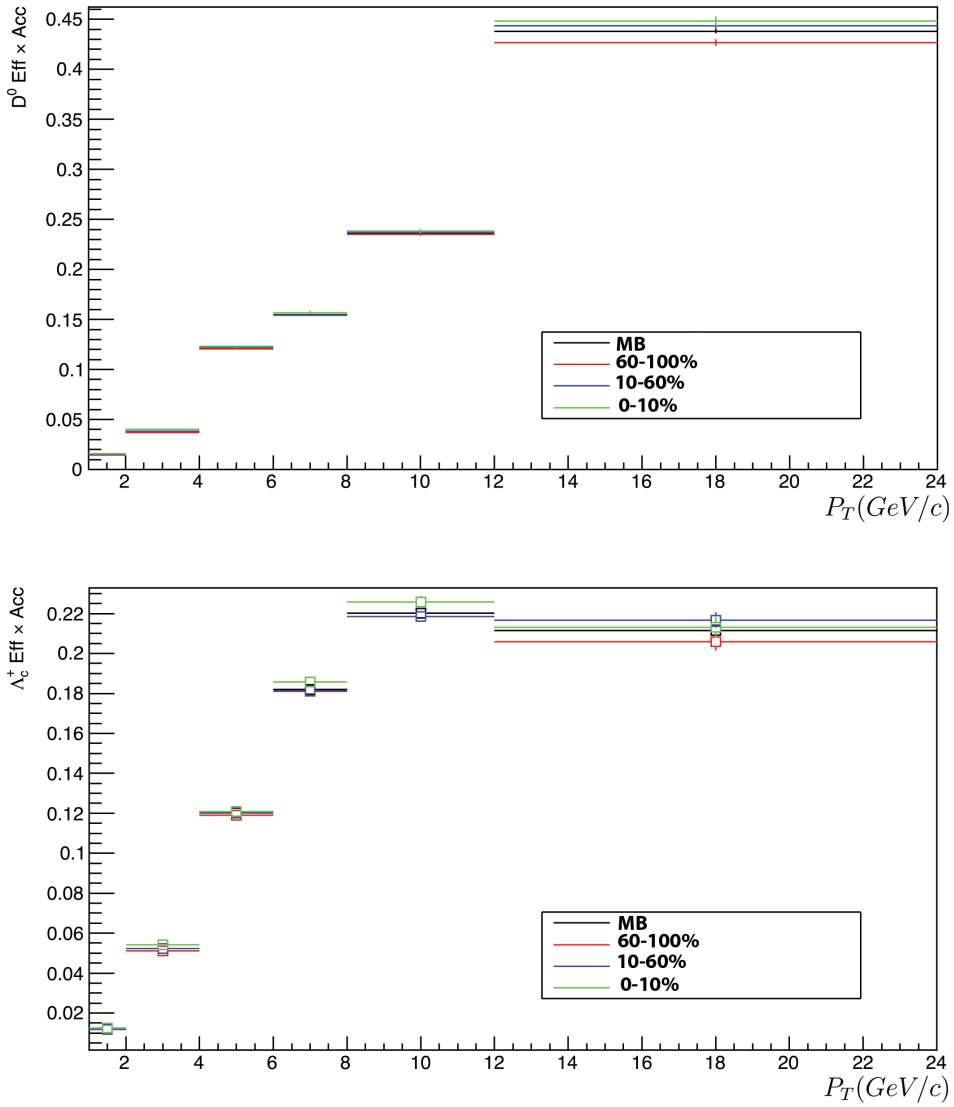

Figure 43: Acceptance-times-efficiency of prompt D^0 mesons (top) with standard analysis and prompt $\Lambda_c^+ \to \mathrm{pK}^-\pi^+$ (bottom) with dedicated Λ_c^+ weights analysis, in different centrality and p_T bins.

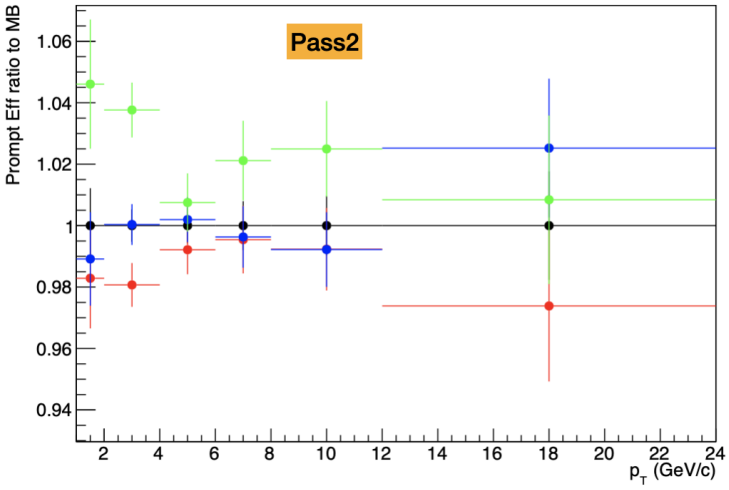

Figure 44: The ratio of Λ_c^+ SPD multiplicity classes: (1-40 Red), (40-65 Blue),(65-200 Green) to minimum bias (0-200)

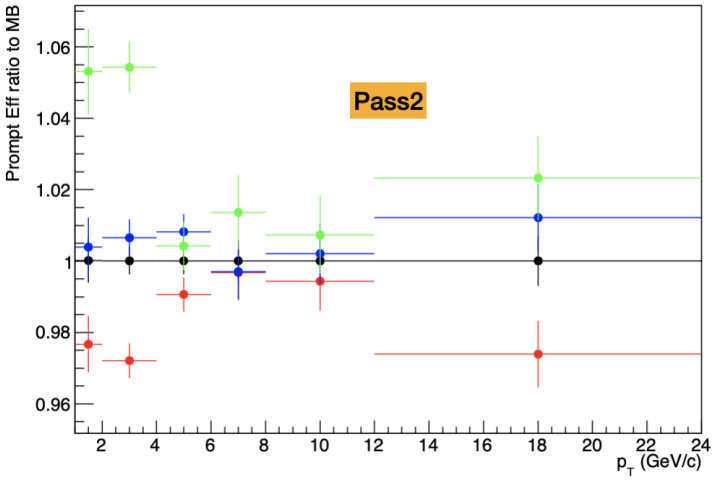

Figure 45: The ratio of D^0 SPD multiplicity classes: (1-40 Red), (40-65 Blue),(65-200 Green) to minimum bias (0-200)

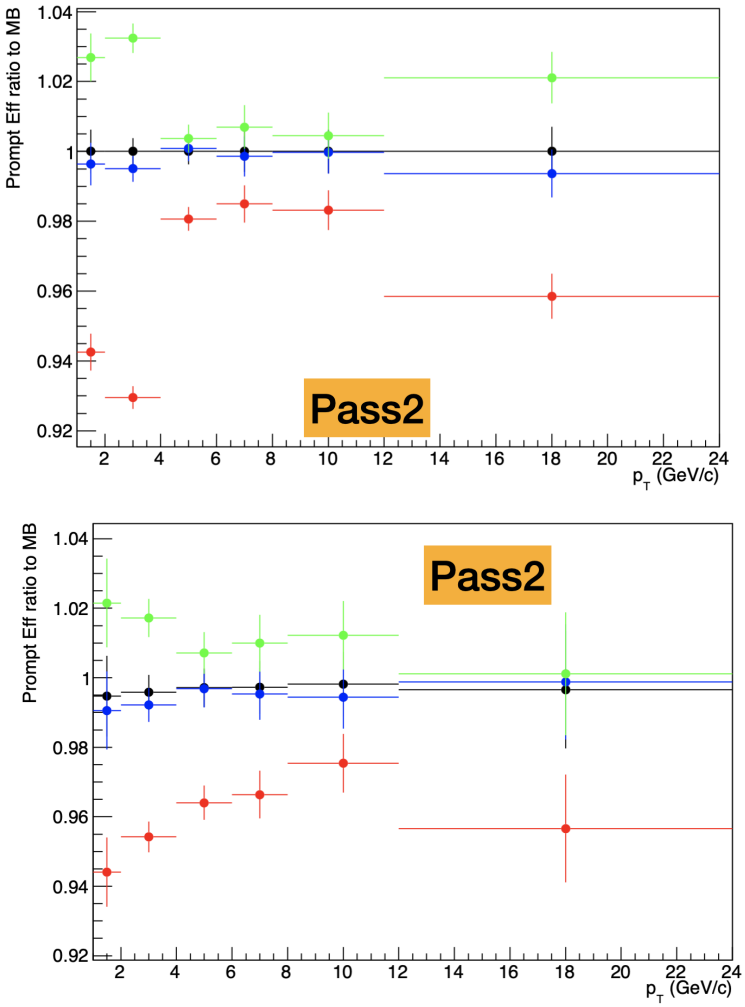

Figure 46: The ratio of V0 multiplicity classes efficiencies (top: D^0), (bottom:Λ_c^+) (60-100 % Red), (10-60 % Blue),(0-10 % Green) to minimum bias (0-200) pass2 V0 analysis with applied multiplicity weights for each V0 class

4.11 Feed Down

The yields of prompt D^0 and Λ_c^+ production, normalized by the number of events in proton-proton (pp) collisions, were determined by subtracting the contributions from B-decay-produced D and Λ_c^+ baryons. Specifically, the contribution of D-meson feed-down was calculated using the beauty production cross-section provided by FONLL calculations, combined with the decay kinematics of $H_b \to D + X$ as modeled by the PYTHIA8 decayer,

and the Monte Carlo efficiencies for the feed-down D mesons. Therefore, simplifying the notation by not explicitly mentioning the transverse momentum (p_{T}) dependence, the fraction representing prompt D mesons is expressed as follows:

$$\begin{aligned} f_{\mathrm{prompt}} &= 1 - (N^{\mathrm{D\ feed-down\ raw}}/N^{\mathrm{D\ raw}}) = \\ &= 1 - \left(\frac{\mathrm{d}^2\sigma}{\mathrm{d}y\,\mathrm{d}p_{\mathrm{T}}}\right)^{\mathsf{FONLL+PYTHIA8}}_{\mathrm{feed-down}} \cdot \frac{(\mathrm{Acc}\times\epsilon)_{\mathrm{feed-down}} \cdot \Delta y\,\Delta p_{\mathrm{T}} \cdot \mathrm{BR} \cdot N_{\mathrm{evt}}}{N^{\mathrm{D\ raw}}/2}\,, \end{aligned} \tag{52}$$

Here, (Acc $\times$ ϵ)feed $-$ down represents the acceptance-times-efficiency factor for feed-down D mesons, and the inclusion of the factor 2 in the denominator accounts for the combined counting of both particles and antiparticles, whereas such a combination is not considered in the FONLL calculations. The systematic uncertainties associated with the subtraction of feed-down contributions are partly evaluated by varying the parameters used in the FONLL predictions for B hadrons. Since the FONLL calculations are independent of event multiplicity, it is assumed that the feed-down fraction is not significantly affected by the multiplicity, and the feed-down efficiencies show minimal variation across various multiplicity intervals. Consequently, the fraction f_{prompt} for the analysis dependent on multiplicity is adopted from the values obtained in the corresponding multiplicity-integrated analysis. The fragmentation functions for beauty hadrons concerning D mesons are sourced from $\mathrm{e^+e^-}$ experimental results as cited from the Particle Data Group (PDG). In contrast, for Λ_{c}^+ baryons, the fraction of beauty quarks fragmenting into Λ_{b}^0 baryons is estimated based on measurements from the LHCb collaboration [98].The two panels in Figure 47 illustrate the feed down ratios for D^0 and Λ_{c}^+

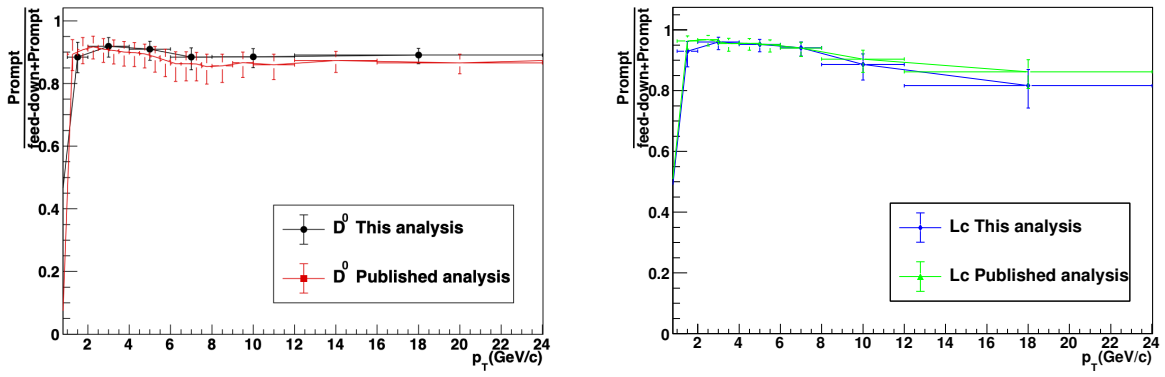

Figure 47: D^0 feed-down fraction as a function of p_T for the multiplicity integrated case (right), using the so-called N_b method. The central predictions used for the analysis with the new FONLL predictions are shown in black, the old FONLL predictions are shown in red, Λ_c^+ feed-down fraction as a function of $p_T$for the multiplicity integrated case (left), using the so-called N_b method. The central predictions used for the analysis with the new FONLL predictions are shown in blue, the old FONLL predictions are shown in Green.

4.12 Systematic uncertainties

In this section, the investigations conducted to assess the various sources of systematic uncertainties in these analyses are detailed. The systematic uncertainties considered are:

- Raw yield extraction, which varies with the multiplicity analysis;
- Selection efficiency, also dependent on the multiplicity analysis;
- Particle identification accuracy;
- Tracking, encompassing track quality and the efficiency of ITS-TPC matching;
- The p_T shape in Monte Carlo simulations;
- Feed-down subtraction, accounting for both FONLL calculations and multiplicity dependence, relevant to multiplicity analysis;
- Efficiency, inclusive of multiplicity weights and the specified interval, both pertinent to multiplicity analysis;

- Branching ratio
- $\mathrm{d}N_{\mathrm{ch}}/\mathrm{d}\eta$ estimation
- Trigger correction

This comprehensive list encapsulates the key factors that influence the systematic uncertainties in the presented analyses, with several elements being particularly sensitive to the multiplicity-dependent aspects of the study.

4.12.1 Raw yield extraction systematic

The systematic uncertainties related to yield extraction were assessed using a MultiTrial approach, where the yields were extracted by varying several aspects: the background fit function, the invariant mass spectrum range, the binning, and the sigma of the mass peak. Additionally, within this framework, four variations in the fitting strategy were explored:

- Fitting by constraining both the mean and the sigma of the signal fit function
- Fitting by constraining only the mean while letting the sigma vary
- Fitting by constraining only the sigma while letting the mean vary
- Fitting without constraints, allowing both the mean and sigma to vary freely

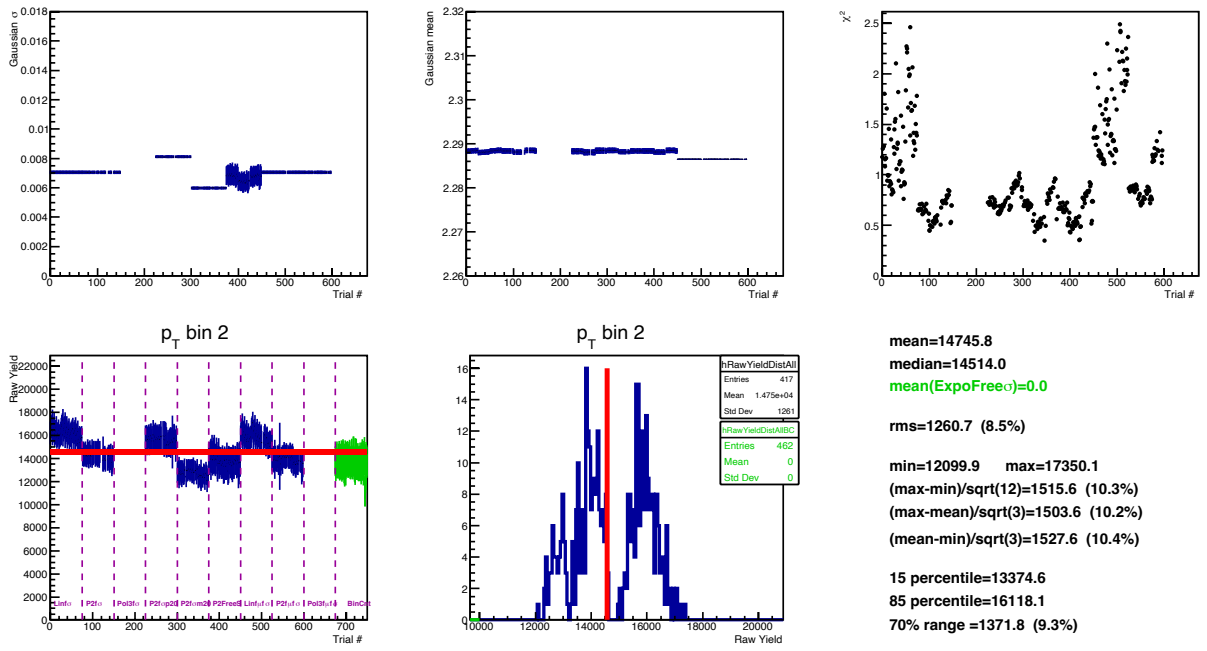

Figure 48: Λ_c^+ Raw yield systematic error evaluation with multi trial approach for $4-6$ GeV/c, Minimum bias

Table 5: Raw yield extraction systematic error for D^0 in different centrality classes

$D^0 \to K^-\pi^+$ p_T / Mult	2-4 GeV	4-6 GeV	6-8 GeV	8-12 GeV	12-24 GeV
0-100%	2%	2%	1%	1%	4%
0-10%	3%	2%	2%	2%	4%
10-60%	2%	2%	1%	1%	4%
60-100%	2%	2%	2%	2%	4%

Table 6: Raw yield extraction systematic error for Λ_c^+ in different centrality classes

$\Lambda_c^+ \to pK^-\pi^+$ p_T / mult	2-4 GeV	4-6 GeV	6-8 GeV	8-12 GeV	12-24 GeV
0-100%	7%	7%	7%	7%	10%
0-10%	10%	10%	8%	8%	15%
10-60%	7%	8%	8%	8%	10%
60-100%	10%	8%	8%	8%	10%

Moreover, two distinct methods of bin counting were incorporated among the variations to extract the signal. One method involves subtracting the background fit function from the total histogram in the signal region, while the other method applies the same procedure but considers the entire invariant mass range. Only those fits that resulted in a reduced χ^2 (chi-squared) value below two were accepted as valid variations for this analysis. The comprehensive parameter spaces, encompassing all the variations and methods applied, are systematically summarized in Tables 5 and 6. These tables detail the different configurations and outcomes of the yield extraction, providing a robust framework for evaluating the systematic uncertainties associated with this part of the analysis. (see Figure 48)

4.12.2 Systematic uncertainties in Candidate Selection

Systematic uncertainties linked to candidate selection are closely tied to the established parameters of the selection cuts. These cuts are pivotal, impacting the raw yield extractions and efficiency computations significantly. To assess these systematic uncertainties, one usually modifies the cut parameters and examines the changes in yields and efficiencies. The process includes: Setting a baseline using central values of the selection cuts, which acts as the reference for the analysis. Applying systematic adjustments of the most relevant cut, here cosine of pointing angle, generally about 10 percent from the baseline figures, to evaluate the robustness of the findings to the selection conditions. This adjustment aims to test the stability of the yield extraction and efficiency determination against variations in the selection parameters. In the case of D^0 mesons, the evaluation involves six variations: three involve progressively less stringent cuts($\cos\theta_p > 0$, $\cos\theta_p > 0.4$, $\cos\theta_p > 0.8$), and three involve more stringent cuts ($\cos\theta_p > 8.8$, $\cos\theta_p > 0.92$, $\cos\theta_p > 0.96$) compared to the baseline. This method assesses how the yield and efficiency react to changes in the strictness of the cuts. For the Λ_c^+ baryon, the strategy differs slightly, with three adjustments that involve increasingly stricter cuts. This aims to explore the particular responses of the Λ_c^+ selection efficiency and its influence on the resultant yield under stricter conditions. The implications of these cut

alterations are thoroughly scrutinized to determine their impact on the ultimate corrected yields. The findings are often summarized in tables (see Tables 7 and 8), illustrating the cut variations and their effects on the raw yields and efficiencies. This meticulous approach guarantees that the derived yields are stable and comprehensively reflect the uncertainties due to the selection criteria. (see Figure 49).

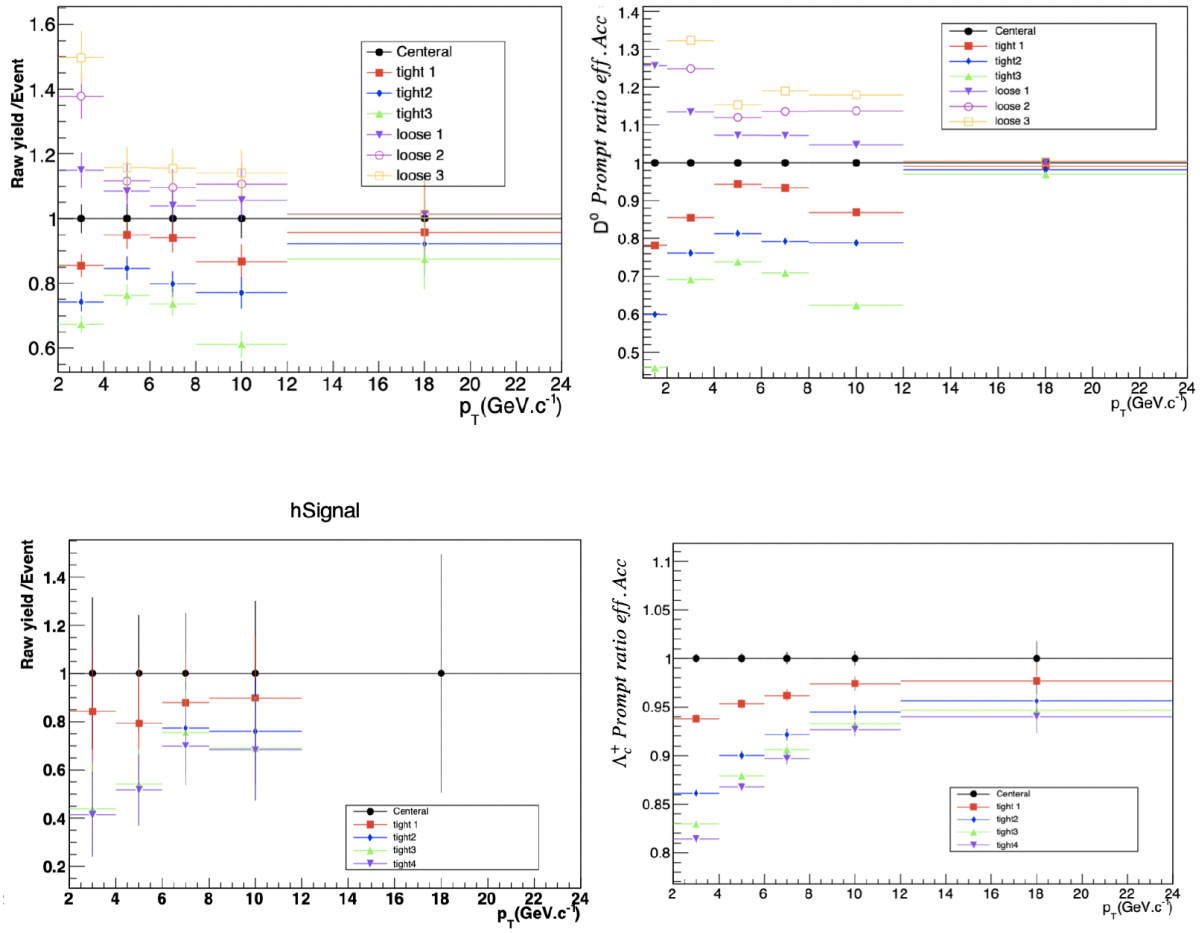

Figure 49: The corrected yield, raw yield, and efficiency of the D^0 (top), presented for three tight and three loose cut selections, and of the Λ_c^+ (bottom), shown for three tight cut selections.

Table 7: D^0 candidate selection systematic uncertainties

D^0	[2, 4] GeV/c	[4, 6] GeV/c	[6, 8] GeV/c	[8, 12] GeV/c	[12, 24] GeV/c
[0, 100]	5%	3%	3%	3%	3%
[60, 100]	5%	3%	3%	3%	3%
[10,60]	5%	3%	3%	3%	3%
[0,10]	10%	3%	25	3%	3%

Table 8: Λ_c^+ candidate selection systematic uncertainties

Λ_c^+	[2, 4] GeV/c	[4, 6] GeV/c	[6, 8] GeV/c	[8, 12] GeV/c	[12, 24] GeV/c
[0-100]%	10%	5%	5%	5%	5%
[0-10]%	15%	10%	10%	10%	-
[60-100]%	20%	10%	10%	10%	10%

4.12.3 Minimum bias systematics

The systematic errors influencing our final results are independent of event multiplicity, suggesting that the selection based on multiplicity does not affect them. These errors are related to tracking, particle identification, and the Monte Carlo (MC) shape at the generation level. These systematics have been assessed in proton-proton collisions at 13 TeV, and have been integrated into this analysis. Tables 9 and 10 show detailed information.

Table 9: Minimum bias systematic uncertainties for $D^0 \to K^-\pi^+$

$D^0 \to K^-\pi^+$	[1, 2] GeV/c	[2, 4] GeV/c	[4, 6] GeV/c	[6, 8] GeV/c	[8, 12] GeV/c	[12, 24] GeV/c
PID	0	0	0	0	0	0
MC pT shape	2%	0	0	0	0	0
tracking	3.5%	4%	5%	5%	5%	5%

Table 10: Minimum bias systematic uncertainties for $\Lambda_c^+ \rightarrow pK^-\pi^+$

$\Lambda_c^+ \rightarrow pK^-\pi^+$	[1, 2] GeV/c	[2, 4] GeV/c	[4, 6] GeV/c	[6, 8] GeV/c	[8, 12] GeV/c	[12, 24] GeV/c
PID	5%	5%	5%	5%	5%	5%
MC pT shape	2%	0	0	0	0	0
tracking	4.5%	5.5%	6%	7%	7%	7%

4.12.4 Feed down contribution

Recent results from proton-proton collisions at 13 TeV indicate that the feed-down contribution is independent of the event's multiplicity. A conservative approach would involve adjusting the range of the nuclear modification factor for various PYTHIA (see Figure 50) modes and assessing the percentage change in the prompt-to-feed-down ratio. (see tables 11 and 12)

Table 11: Feed down contribution systematic uncertainties for D^0 in V0 multiplicity estimator

$D^0 \rightarrow K^-\pi^+$	**[2, 4] GeV/c**	**[4, 6] GeV/c**	**[6, 8] GeV/c**	**[8, 12] GeV/c**	**[12, 24] GeV/c**
[0, 10]	-4% +2%	-4% +2%	-4% +2%	-4% +2%	-4% +2%
[10, 60]	-2% +2%	-2% +2%	-2% +2%	-2% +2%	-2% +2%
[60, 100]	0% +5%	0% +6%	0% +7%	0% +7%	0% +6%

Table 12: Feed down contribution systematic uncertainties for Λ_c^+ in V0 multiplicity estimator

$\Lambda_c^+ \rightarrow pK^-\pi^+$	[2, 4] GeV/c	[4, 6] GeV/c	[6, 8] GeV/c	[8, 12] GeV/c	[12, 24] GeV/c
[0, 10]	-2 % ± 1%	-3 % ± 1%	-4 % ± 2%	-5 % ± 2%	-5 % ± 2%
[10, 60]	-1 % ± 1%	-1 % ± 1%	-2 % ± 2%	-2 % ± 2%	-2 % ± 2%
[60, 100]	0 % ± 2%	0 % ± 4%	0 % ± 6%	0 % ± 7%	0 % ± 7%

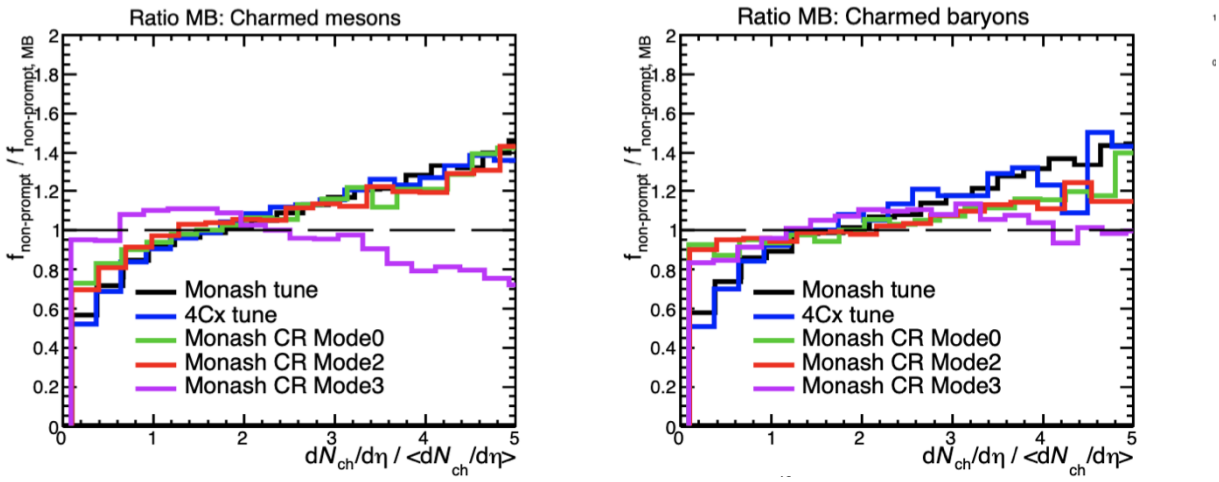

Figure 50: The variation of feed-down contribution as a function of multiplicity in PYTHIA across different modes of PYTHIA color reconnection and the Monash tune.

4.12.5 Multiplicity weights

The efficiency of reconstructing and selecting heavy-flavour hadrons, particularly those identified through secondary vertices, is influenced by the charged particle multiplicity in the event. The event multiplicity within Monte Carlo (MC) simulations often does not match the more precisely defined multiplicity in real data, leading to the need for a correction factor to tune the MC to data. In this analysis, events are chosen from both MC and data if they include at least one candidate that meets all selection criteria and has an invariant mass no more than 20 MeV/c^2 from the Particle Data Group (PDG) reference value, a condition denoted as $\Delta m < 20$. For these events, normalized multiplicity distributions are determined, labeled f_{MC} for MC and f_{data} for data. Event weights ω_i for each multiplicity bin in the detector barrel region are then calculated by dividing the data distribution by the MC distribution. The event weight calculations can be found in Tables 13 and 14.

Table 13: Systematic error for the events multiplicity weights for D^0

D^0	[2, 4] GeV/c	[4, 6] GeV/c	[6, 8] GeV/c	[8, 12] GeV/c	[12, 24] GeV/c
[0, 100]	0.5%	0.2%	0.2%	0.2%	0.2%
[60, 100]	1%	1%	0.2%	0.2%	0.2%
[10,60]	0.2%	0.2%	0	0	0
[0,10]	0	0	0	0	0

Table 14: Systematic error for the events multiplicity weights for Λ_c^+

Λ_c^+	[2, 4] GeV/c	[4, 6] GeV/c	[6, 8] GeV/c	[8, 12] GeV/c	[12, 24] GeV/c
[0, 100]	0.5%	0.5%	0.5%	0.5%	0.5%
[60, 100]	1%	1%	1%	0.5%	0.5%
[10,60]	0.5%	0.5%	0.5%	0.5%	0.5%
[0,10]	0.5%	0	0	0	0

4.13 Results

The corrected yield for the Λ_c^+ and D^0 is calculated in SPD (see Figure 51) and the V0 (see Figure 52. The Λ_c^+/D^0 ratio is then calculated using those corrected yields, as it is shown in figure 53, only statistical error bars in counter. In the figure 60 the systematic errors bars are also incorporated alongside statistical error bars. To ensure consistency between the minimum bias cross-sections from initial (pass1) and advanced (pass2) data processing, several tests were conducted. Pass1 refers to the primary processing of raw data, which includes elementary calibration and event selection, whereas pass2 involves more sophisticated analyses and refined calibration techniques. The compatibility of the final results from both passes is critical for the reliability of the data, as demonstrated in Figures 55 and 56. Further comparisons were made with published results from minimum bias analyses of Λ_c^+ and D^0 hadrons, as shown in Figures 57 and 59, considering both the $\Lambda_c^+ \to pK^-\pi^+$ and $\Lambda_c \to pK_S^0$ decay channels. The

ratio of the raw yield per event to the efficiency was separately evaluated with a linear fit to scrutinize the discrepancy between pass1 and pass2, validating the compatibility of the MB cross-section. For D^0 hadrons, as seen in Figure 54, pass2 showed a 3 percent increase in raw yield compared to pass1. In the case of Λ_c^+, Figure 55 indicates about a 5 percent higher ratio. Efficiency comparisons revealed that pass2's efficiency times acceptance for D^0 is up by 4 percent and Λ_c^+ by 14 percent. This difference has led to a 3 percent decrease in the final cross-section for D^0 in pass2 compared to pass1, shown in Figure 56, and about an 8 percent decrease for Λ_c^+, as depicted in Figure 57. The corrected yields of Λ_c^+ and D^0 were calculated using both SPD (Figure 51) and V0 estimators (Figure 52), and the Λ_c^+/D^0 ratio was derived from these yields (Figure 53). The statistical errors are represented by error bars in these figures. A more comprehensive analysis that includes systematic uncertainties alongside statistical ones is presented in Figure 60, where the p_T-differential corrected yields for Λ_c^+ and D^0 across various multiplicity intervals in p–Pb collisions are illustrated.

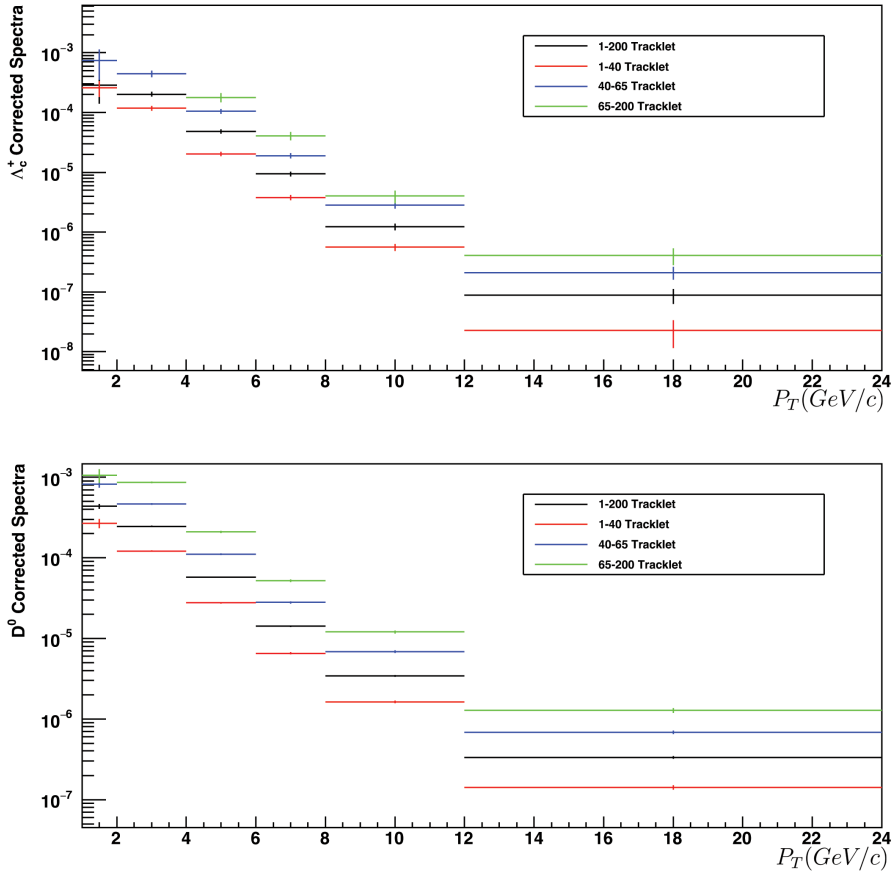

Figure 51: Corrected yield per event for the different SPD multiplicity estimator classes for Λ_c^+ (top) and D^0 (bottom)

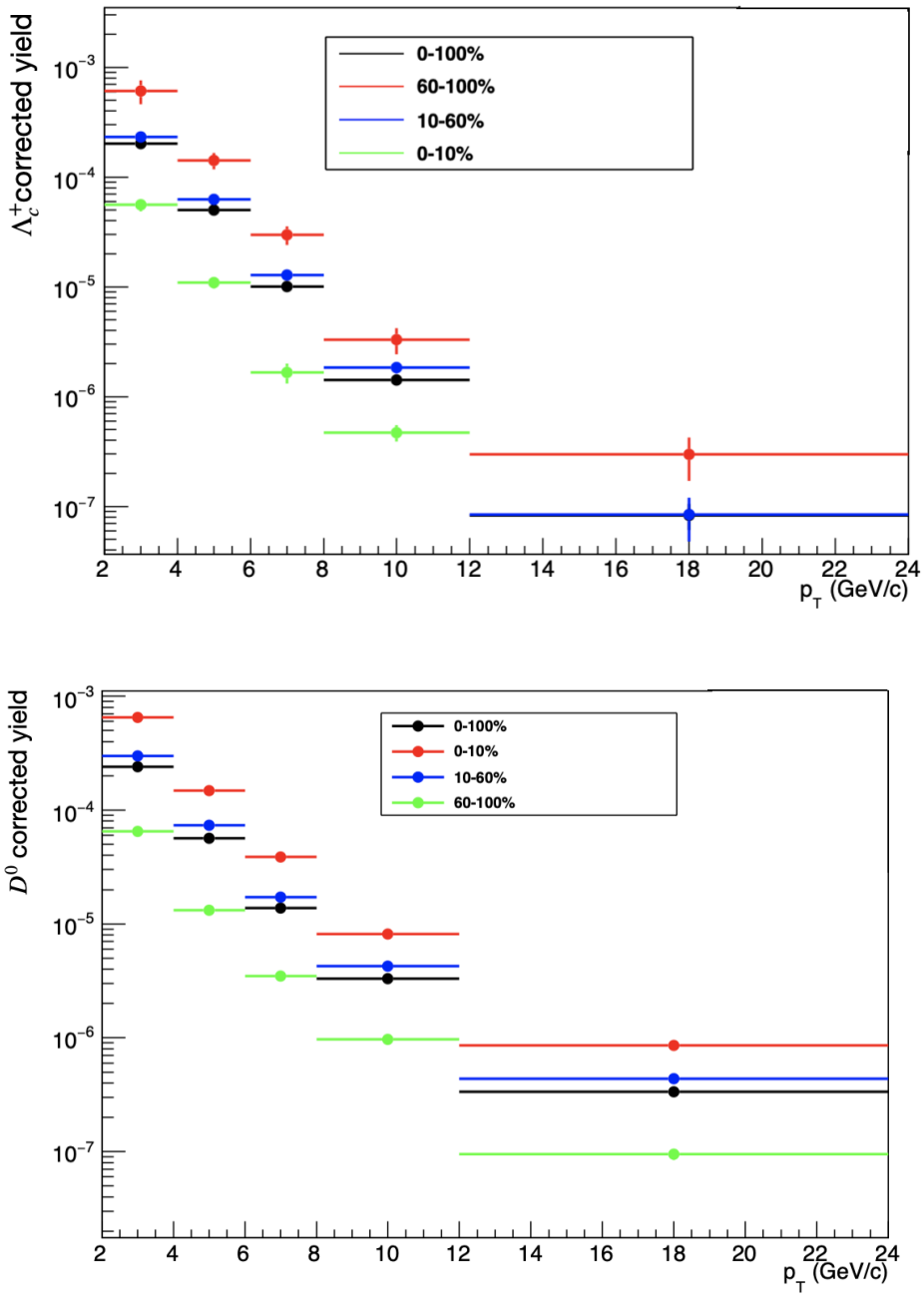

Figure 52: Raw yield per event for the different V0 multiplicity estimator classes for Λ_c^+ (top) and D^0 (bottom)

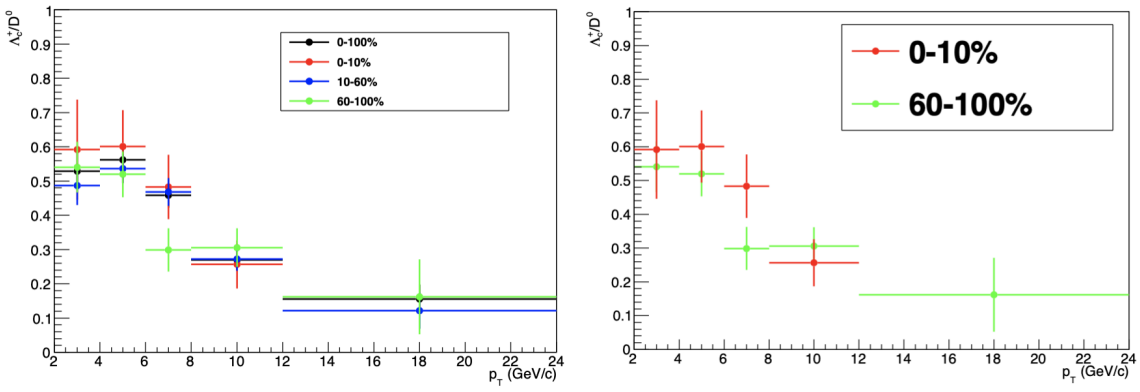

Figure 53: Λ_c^+/D^0 ratios in the different multiplicity intervals (left) for the V0 multiplicity estimators. Same ratio (right) only for the most Central (red) and the most peripheral events(green)

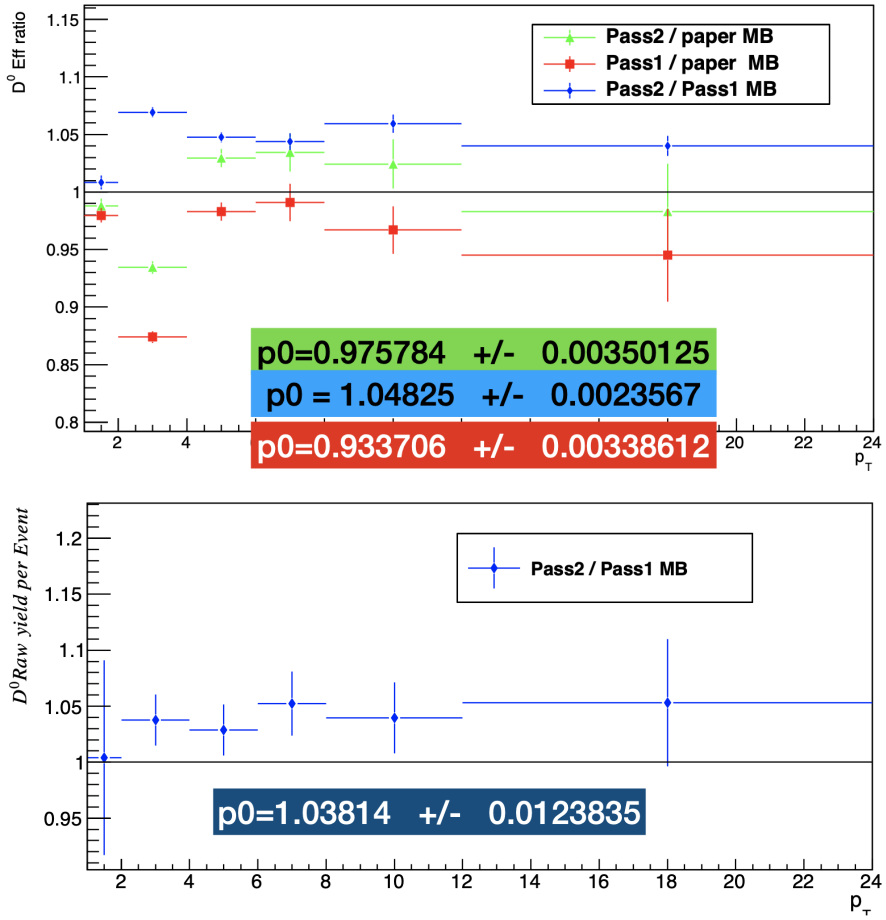

Figure 54: The ratio of raw yield per event for pass1, pass2 for D^0, The ratio of prompt efficiencies for pass1, pass2, and published MB D^0 mesons

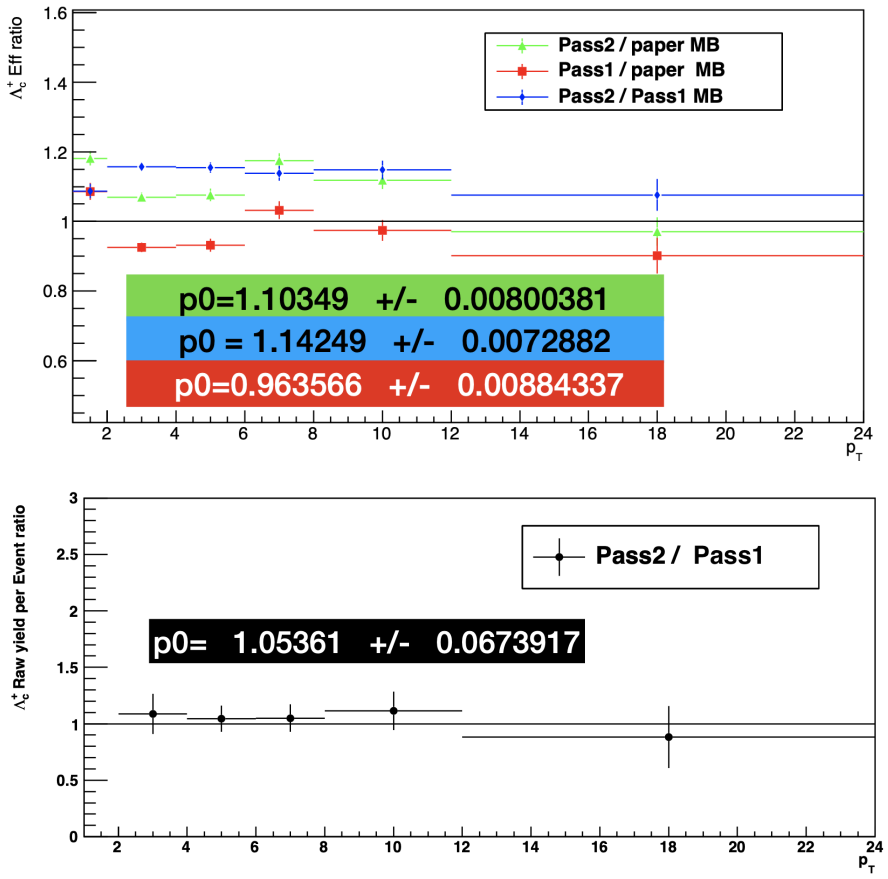

Figure 55: The ratio of raw yield per event for pass1, pass2 for Λ_c^+, The ratio of prompt efficiencies for pass1, pass2, and published MB Λ_c^+ baryons

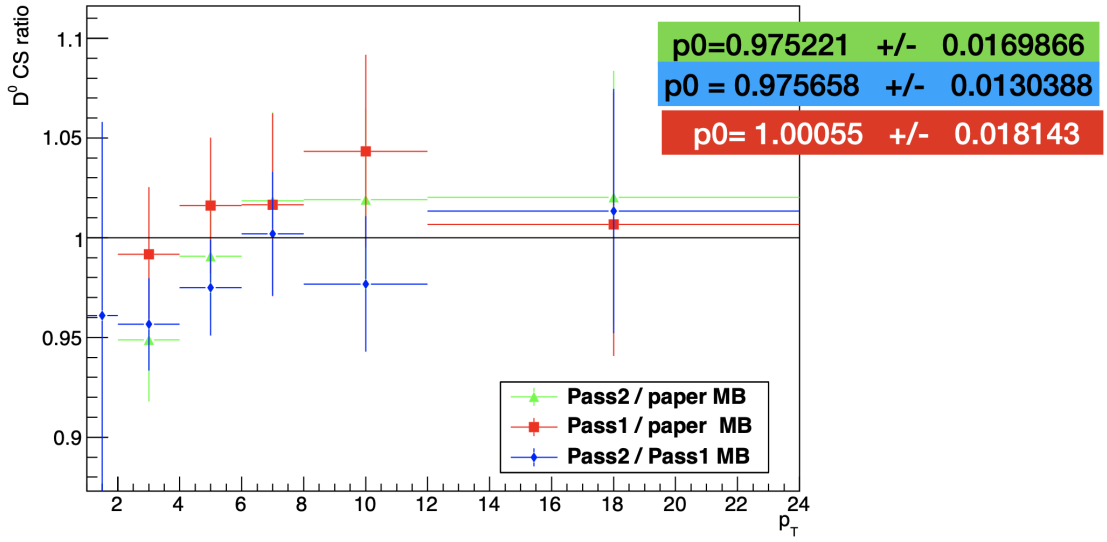

Figure 56: The ratio of MB cross section for pass1, pass2, and published MB D^0 mesons

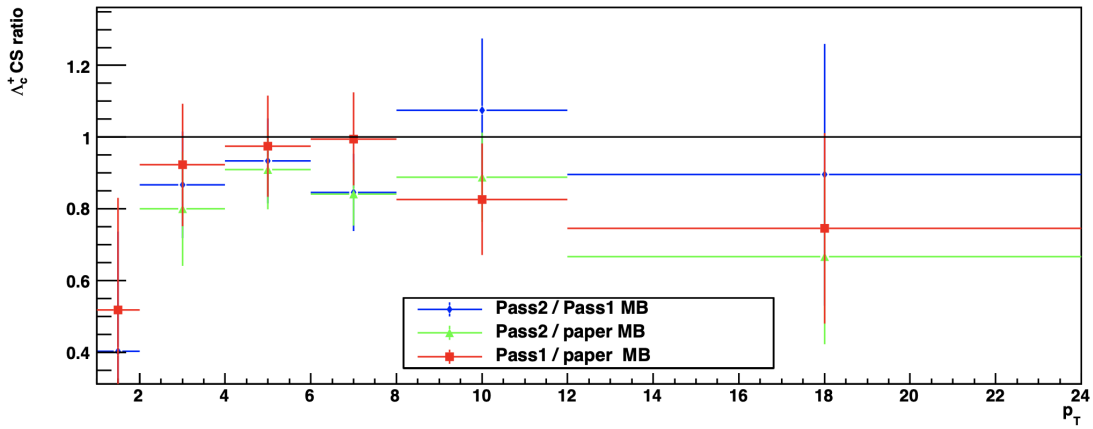

Figure 57: The ratio of MB cross section for pass1, pass2, and published MB Λ_c^+ baryons

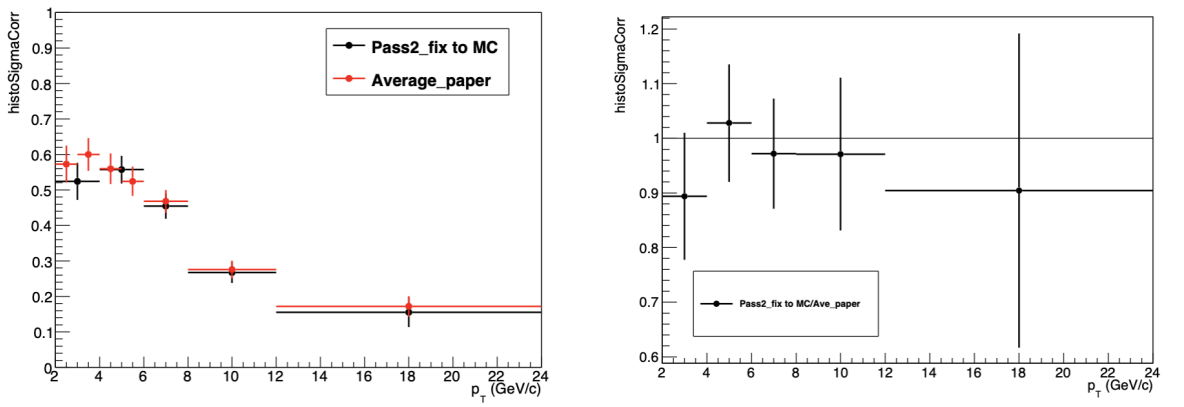

Figure 58: Comparison between the Λ_c^+/D^0 ratios with the published paper in $\Lambda_c^+ \to pK_s^0 \to p\pi^+\pi^-$ channel

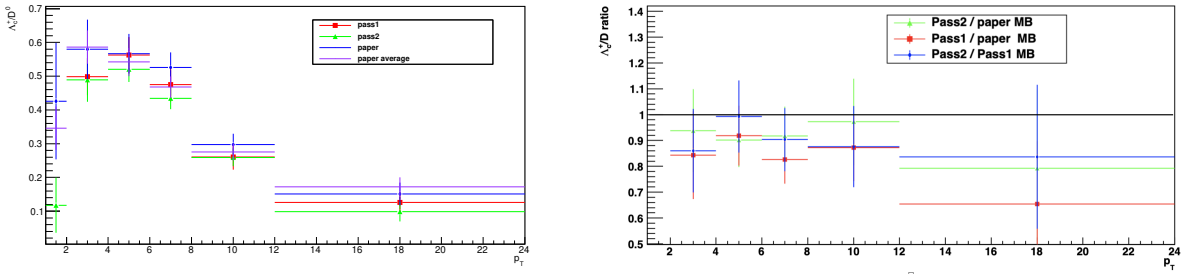

Figure 59: Λ_c^+/D^0 obtained by MB cross section of pass1, pass2, paper and paper average, note the paper only has $\Lambda_c^+ \to pK^-\pi^+$and paper average use both $\Lambda_c^+ \to pK^-\pi^+$and $\Lambda_c^+ \to pK_s^0 \to p\pi^+\pi^-$.

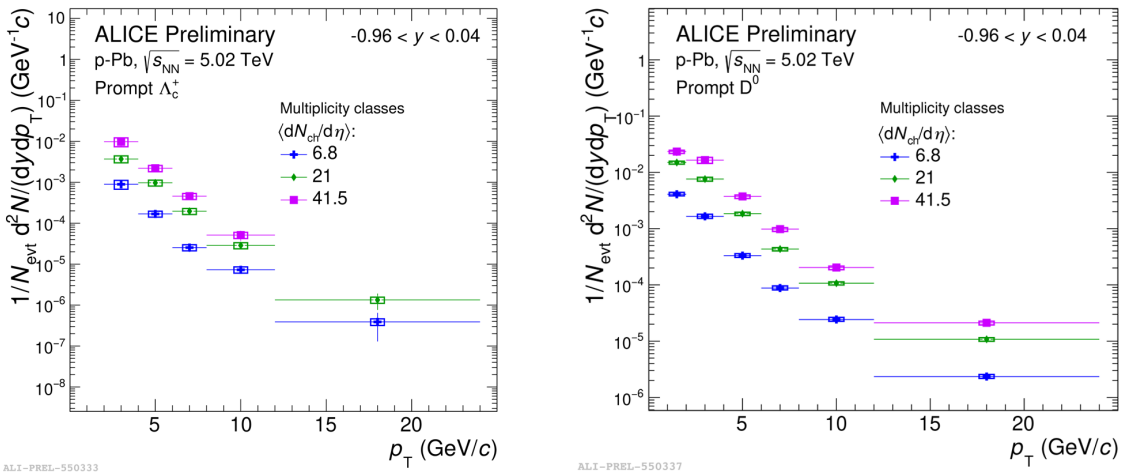

Figure 60: p_{T}-differential Λ_{c}^{+} (left) and D^0 (right) corrected yields in three intervals of charged-particle multiplicity, in p–Pb collisions at $\sqrt{s_{\mathrm{NN}}} = 5.02$ TeV

5 Machine learning studies for the $\Lambda_c^+ \to pK^-\pi^+$ decay mode in the p_T bin of 1-2 GeV/c.

In the previous chapter, we explored how the implementation of geometrical and kinematic cuts enables us to collate the mass distribution of candidates. The core concept revolves around the fact that near the physical mass of the particle we aim to detect, there is a superposition of contributions from both the signal and the background. The signal consists of real particles reconstructed from their decay daughters, while the background comprises all the candidate mothers constructed from uncorrelated pairs. The background's contribution to the mass distribution is expected to follow a smooth function that can be subtracted, and typically, the signal around the physical mass manifests as a Gaussian function. However, scenarios exist where the system's resolution is insufficient to distinguish between the decay length and the correct secondary vertex. For example the resolution of the ITS at 1-2 GeV/c is almost equal to Λ_c^+ decay lenght ($c\tau \approx 60\mu$m). If the resolution surpasses the decay length (see Figure 61, right), the secondary vertex can be accurately identified, enhancing the signal. Conversely, if the decay length is comparable to the system's resolution, it is likely that many events and the candidates reconstructed from them are background. In such cases, the mass distribution doesn't visibly exhibit any peak superimposed on the background, rendering the conventional method of applying a lower threshold for cuts—in other words, selecting variables exceeding a minimum threshold—ineffective. Consequently, the fitting strategy fails to extract a significant signal and extract the raw yield. Here, machine learning tools prove beneficial. Unlike classical methods that do not account for all decay variables, their interrelations, and their collective correlation to signal and background, we can train a binary classifier. This classifier leverages signals from simulations and contrasts them with sets of background candidates formed from uncorrelated pairs. The premise is that machine learning models can analyze variable correlations to discern the distinct "fingerprints" differentiating signal from background.

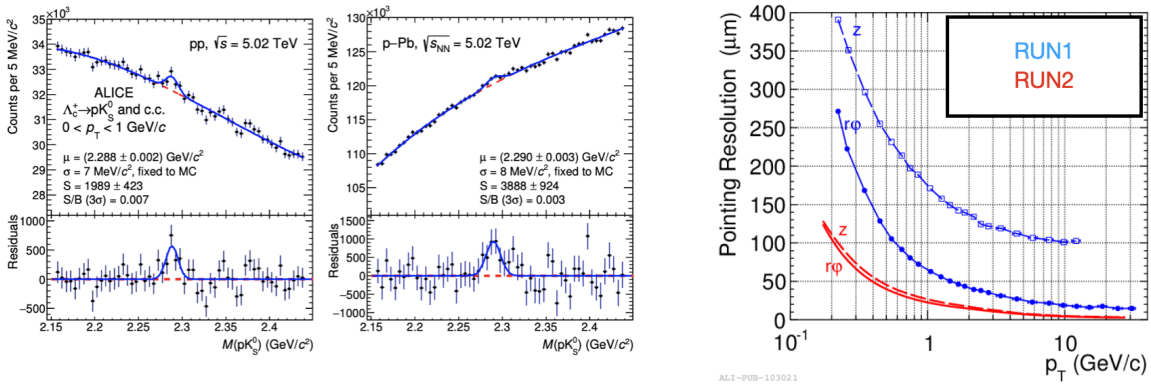

Figure 61: The invariant mass extracted with machine learning model for the $\Lambda_c^+ \to pK_0$ decay channel (left) [99], the spatial resolution of the ITS as function of p_T at Run1 and Run2 (right)

5.1 Machine learning configuration

HIPE4ML is a framework which uses xgboost python libraries for training a binary classifier. XGBoost, which stands for eXtreme Gradient Boosting, is an open-source software library that provides a scalable, portable, and distributed gradient boosting framework. It is designed to efficiently handle large-scale and complex data, making it a popular choice for machine learning competitions and real-world applications. The core algorithm is based on the gradient boosting framework, which constructs new models that predict the residuals or errors of prior models and then combines them to make the final prediction more accurate. HIPE4ML is a project that aims to utilize innovative techniques, like XGBoost, in the analysis of data from particle physics experiments. XGBoost applies advanced regularization (L1 and L2), which improves model robustness and accuracy, vital for identifying subtle patterns in complex background.

5.2 Providing the data frame

Pandas dataframes is a common format that is used in many python based machine learning library which is a two-dimensional, size-mutable, and potentially heterogeneous tabular

data structure with labeled axes (rows and columns). dataframes support a wide range of operations such as slicing, reshaping, joining, merging, and more, making them highly versatile for data manipulation, statistical analysis, and data transformation. To initially provide the candidates in the dataset we use the another data structure TTREE in order to store the Λ_c^+ candidate information on event by event basis. A TTREE is a tree-like data structure designed to store large datasets in a structured way. It consists of branches (TBranch), which can be likened to columns in a spreadsheet, where each branch can hold data of different types, including simple types (like integers or floating-point numbers) or more complex types (like objects) and is optimized for efficient data storage and retrieval. It allows for the storage of large quantities of data in a compact form, making it possible to manage data volumes that are typical in high-energy physics experiments, which can amount to several petabytes. TREE handler method is used in the HIPE4ML class to convert this tree to data frame that is being used for the machine learning purposes.

5.3 Data frame

Each candidate exhibits 54 variables in total (see Figure 62), including the geometry and topology of decay, most importantly decay length, and the cosine of the pointing angle. The PID (Particle Identification) information of the systems is available in three classes: first, the TPC (Time Projection Chamber) and TOF (Time Of Flight) signals standalone; second, the combined signal from TPC and TOF; and third, the Bayesian combination of TPC and TOF to maximize the likelihood of particle identification.

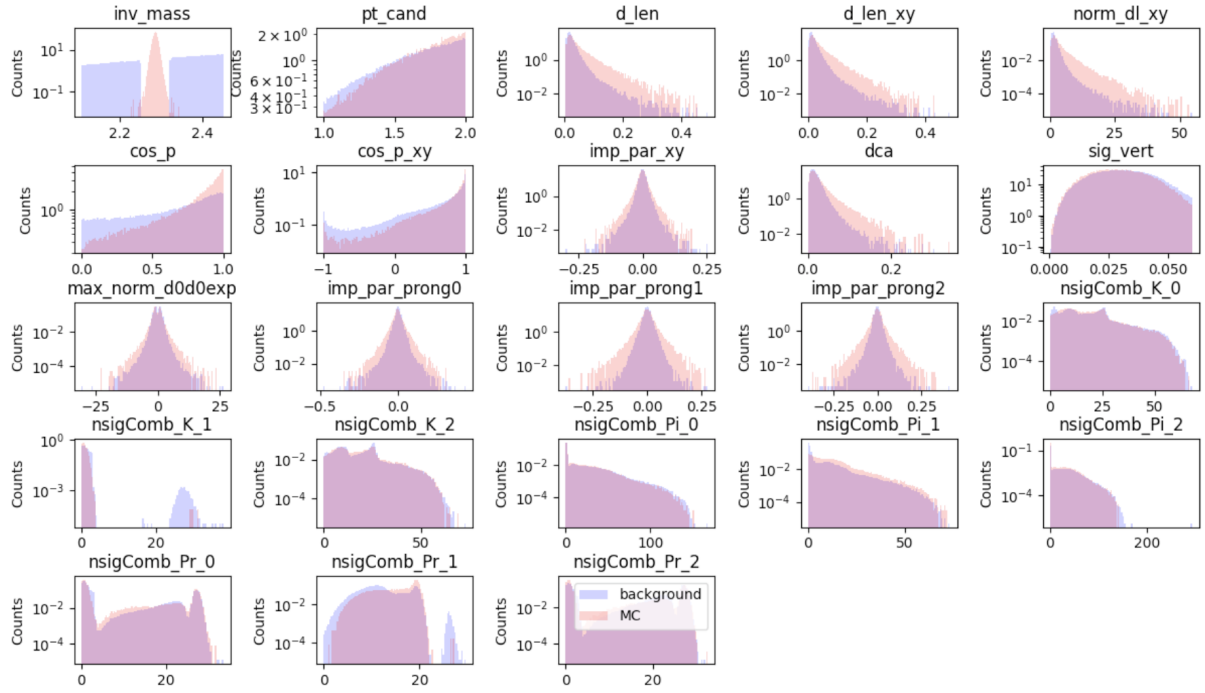

Figure 62: Multiple histograms representing various machine learning features used in $\Lambda_c^+ \to pK^-\pi^+$ analysis. The inv mass represents the invariant mass of a particle candidate. The pt cand is the transverse momentum of the candidate. cosp and cospxy are the cosine of the pointing angle in three dimensions and the transverse plane, respectively, which indicate the alignment of the candidate momentum vector with the vector from the primary vertex to the decay vertex. dlen and dlenxy correspond to the decay length in three dimensions and the transverse plane. normdlxy is the normalized decay length in the transverse plane. dca refers to the distance of closest approach to the primary vertex. sigvert is the significance of the vertex displacement from the primary vertex. impparprongX (where X is 0, 1, or 2) indicates the impact parameter of each decay prong. maxnormd0d0exp represents the maximum normalized product of impact parameter significances. nsigCombXY (where X is the particle type K, π, p and Y is the hypothesis index 0, 1, or 2) are the number of sigma combinations from the expected signal for particle identification. These variables help differentiate signal from background ('background') as trained and evaluated on Monte Carlo simulated data ('MC').

5.4 Configuration of machine learning model

In machine learning, the dataset is typically divided into two main sets: the training set and the test set. The training set plays a crucial role in building the model. It contains a large portion of the data along with the correct answers (labels), and it is used to teach the model how to make predictions. The model learns and adjusts its parameters during this phase.

On the other hand, the test set is used to evaluate the model's performance. It is a separate dataset not seen by the model during training, enabling evaluators to assess how well the model generalizes to new, unseen data. This division helps in mitigating issues like overfitting, where the model performs exceptionally well on the training data but poorly on any unseen data, ensuring that the model is robust, versatile, and reliable in real-world applications. 70 percent of the dataset is used for training the model, and the remaining 30 percent is used for testing. This ratio is often chosen as a balance between having enough data to train the model effectively and enough data to test and validate the model's performance.

5.5 Hyper parameter optimization

Hyperparameter optimization is a crucial process in machine learning that involves tuning the parameters of a model that are set before the learning process begins. These parameters, known as hyperparameters, influence the training process and the performance of the model, but are not adjusted automatically during the training (unlike model parameters). The aim of hyperparameter optimization is to find the set of hyperparameters that yields the best performance, as measured by a predefined metric. The term "hyper" in hyperparameters essentially means "above" or "beyond." Unlike regular parameters, hyperparameters are not learned from the data during the training process. They are set prior to training and define higher-level concepts about the model, such as its complexity or how fast it should learn. The optimal hyperparameters heavily depend on the dataset and the specific problem you're addressing. Different datasets have different characteristics (like the number of features, the amount of noise, or the data distribution), and what works well for one dataset might not work well for another. This is why hyperparameter optimization is usually an integral part of the model-building process, requiring a separate validation dataset or cross-validation to evaluate the performance of different hyperparameters objectively. Optimization refers to the process of searching for the most effective hyperparameters that result in the best model performance. The goal is to find the hyperparameters that lead to the optimal

balance between underfitting and overfitting, or more specifically, to maximize or minimize a specified performance metric. When the optimization is meant to maximize the Area Under the Receiver Operating Characteristic Curve (AUC) and use cross-validation, it implies that the hyperparameter tuning process aims to find the hyperparameters that lead to the model with the highest AUC value, ensuring the model's robustness and generalizability.

A Boosted Decision Tree is an ensemble learning method where multiple decision trees are combined in a sequential manner to improve the model's accuracy. The method boosts weak learners (simple decision trees) by iteratively learning from the mistakes of previous trees, and the final model is a weighted sum of these trees. The key hyperparameters include the number of estimators, which determines the number of trees to be included in the model; the depth of the tree, which controls the maximum number of levels in each tree and helps in managing the model's complexity and tendency to overfit; and the learning rate, which dictates the speed at which the model learns by controlling the contribution of each tree to the final combination. Tuning these hyperparameters is crucial as they significantly influence the model's performance, balancing the trade-off between bias and variance.

5.6 Correlation Matrix

Given 54 variables from a Monte Carlo simulation (e.g., PYTHIA) representing signal and background, where these variables form uncorrelated pairs but show distinct correlation patterns between the signal and background, machine learning techniques, especially boosted decision trees, can efficiently leverage these patterns to differentiate between the two categories. Boosted decision trees build a series of decision trees where each tree attempts to correct the mistakes of the previous one. Throughout the learning process, the algorithm evaluates the importance of each feature (or variable) in separating the signal from the background. Features that are more indicative of a class will be used more frequently and earlier in the tree structure, allowing the model to exploit the distinct "fingerprint" of correlations present

(Figure 63) in the signal and background.

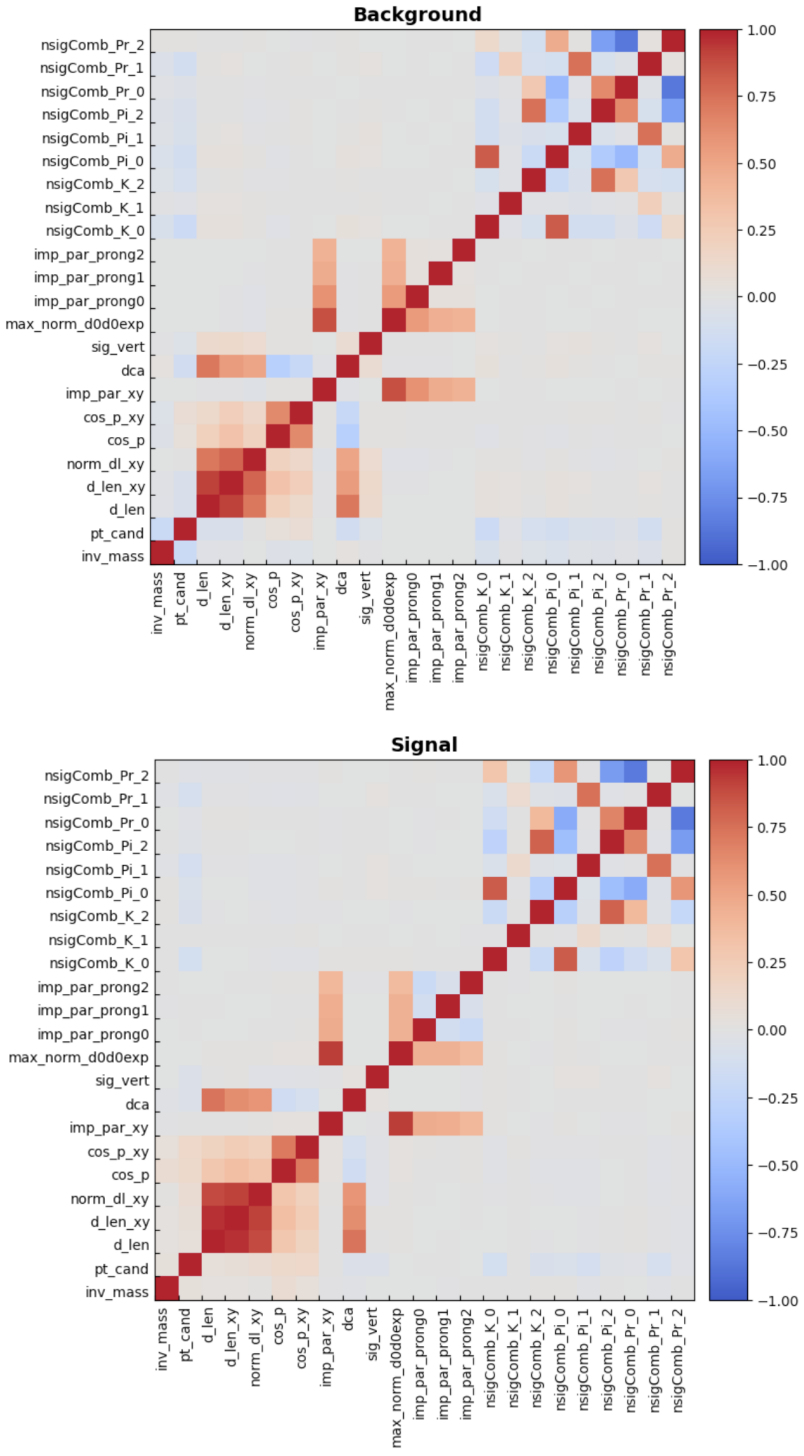

Figure 63: Correlation matrices for background (top) and signal (bottom), serving as fingerprints for a binary classifier in particle physics. Each matrix element represents the Pearson correlation coefficient between two features, ranging from -1 (perfect negative correlation) to 1 (perfect positive correlation), with 0 indicating no correlation.

5.7 Receiver operating characteristic curves

The Receiver Operating Characteristic (ROC) curve is a graphical plot (Figure 64 and 65) used to evaluate the performance of a binary classifier system as its discrimination threshold is varied. It is a fundamental tool for diagnostic test evaluation and is widely used in machine learning for classification tasks. On the y-axis, the ROC curve plots the true positive rate, also known as recall or sensitivity, which measures the proportion of actual positives that are correctly identified. On the x-axis, it plots the false positive rate, which measures the proportion of actual negatives that are incorrectly identified as positives. The area under the ROC curve (AUC) is a measure of the classifier's ability to distinguish between the classes and is used as a summary of the model's performance. An AUC of 0.5 suggests no discriminative ability (equivalent to random guessing), while an AUC of 1.0 represents a perfect model. Ideally, the ROC curves for the training and test sets should be close to each other. This indicates that the model has generalized well from the training data to unseen data, for the case of using only geometry and separated signal from TPC and TOF (Figure 64). The closer these curves are, the more confidence you can have that the model will perform well on new, unseen data. The final strategy is to use geometry and combined signal from TPC and TOC (Figure 65).

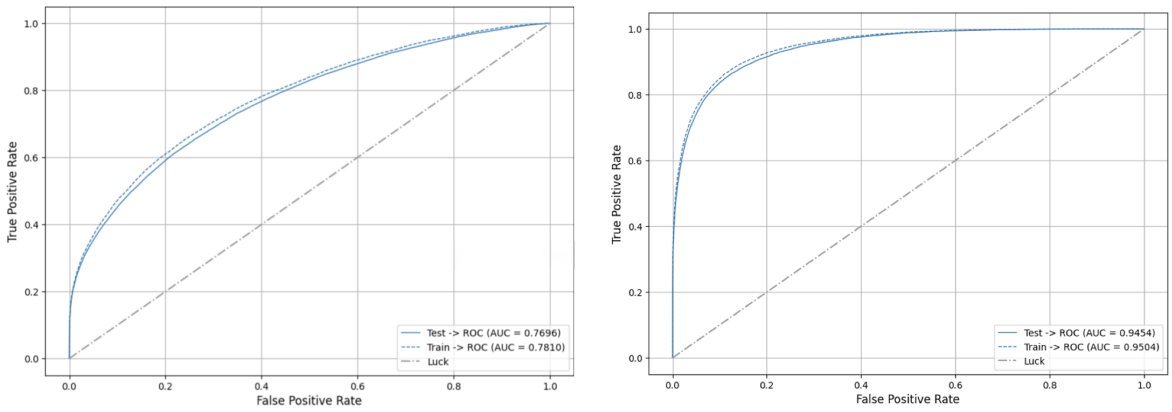

Figure 64: Characteristic operating curves for different scenarios of training a binary classifier are presented, from left respectively: decay geometry only, and decay geometry combined with Bayesian response from TPC and TOF. for the analysis to avoid overfitting, as evidenced by the lack of a complete match between the training and test sets.

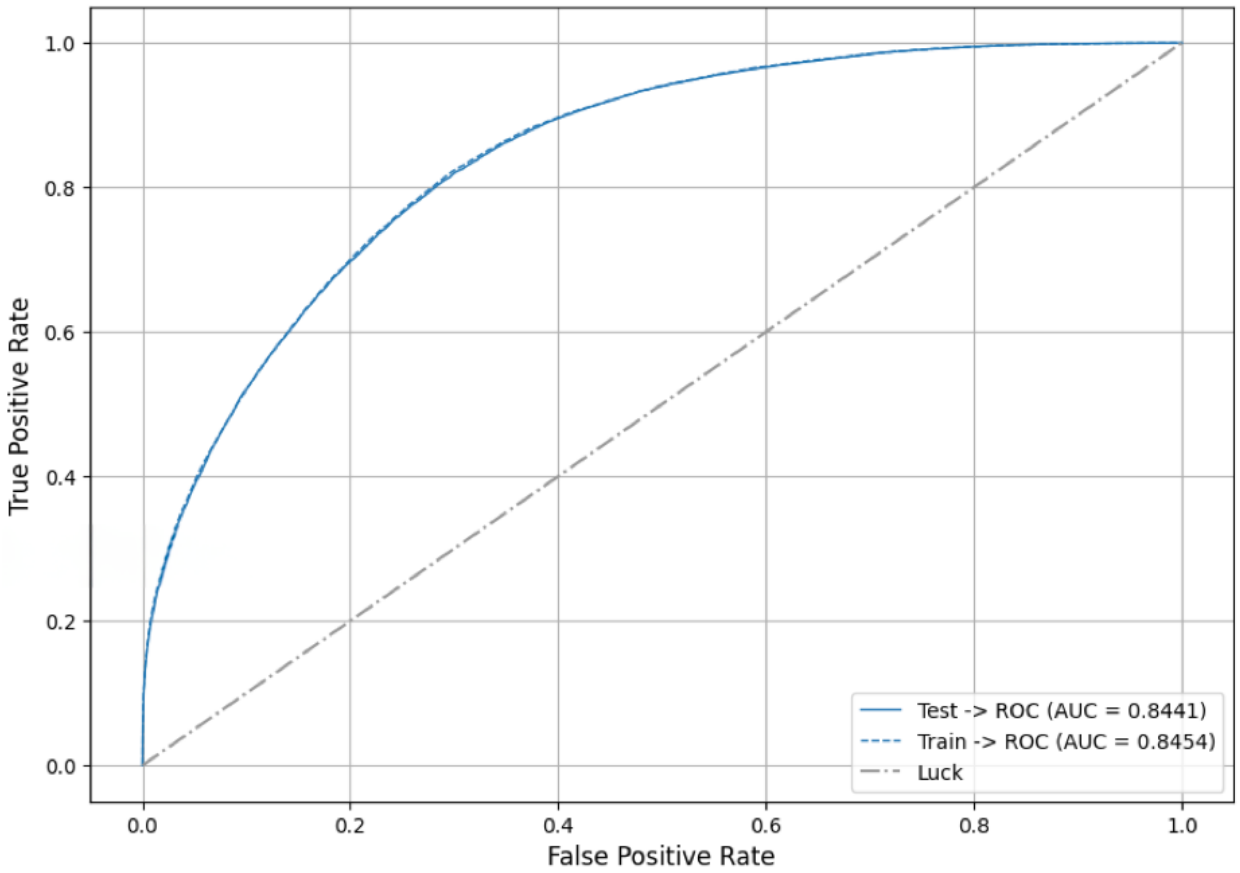

Figure 65: Characteristic operating curves for decay geometry combined with Nsigma response from TPC and TOF, as final strategy

5.8 BDT distribution

After the model is trained, all candidates are assigned a boosted decision tree (BDT) score that quantifies the probability that a candidate is either signal or background. A score of 0 represents the lowest scored candidates, and a score of 1 is the highest possible score. It is important to note that assigning this score does not completely separate the signal from the background but rather provides a measure that quantifies the quality of the candidates. One of the plots used in this analysis is the BDT distribution function over the candidates and over the background for both training and test samples. This distribution shows how the scores are spread across the background and signal. Typically, the background will show a

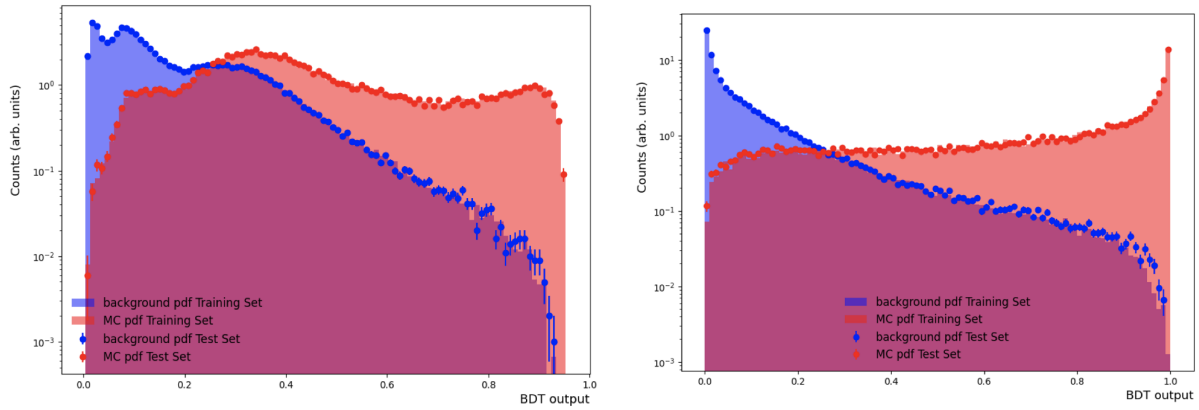

Figure 66: The distribution of the BDT score among signal and background for different scenarios of training a binary classifier are presented, from left respectively: decay geometry only, and decay geometry combined with Bayesian response from TPC and TOF.

higher number of candidates at lower BDT scores, and in general, the signal will demonstrate a decreasing trend with increasing BDT scores. As the BDT score increases, the number of candidates that exhibit the highest scores also decreases. There is an intersection between the background and the signal, which determines a BDT score above which the background and signal can be effectively separated. Therefore, when considering applying a BDT cut to the candidates, we must choose a threshold that is at least larger than the intersection score (Figure 66 and 67)

5.9 Signal extraction

After the training process, candidates are evaluated and given scores by the boosted decision tree (BDT). If a BDT threshold is set, only a fraction of the candidates—those with scores above the minimum—are retained. As the BDT threshold is raised, both signal and background are reduced simultaneously. The objective is to set a BDT threshold such that the signal can emerge from the background. It is necessary to reduce the background to a level where the signal becomes visible. However, as the BDT score increases and the background decreases, background subtraction becomes less accurate due to the reduction in background events. This inaccuracy in the background subtraction at high BDT scores

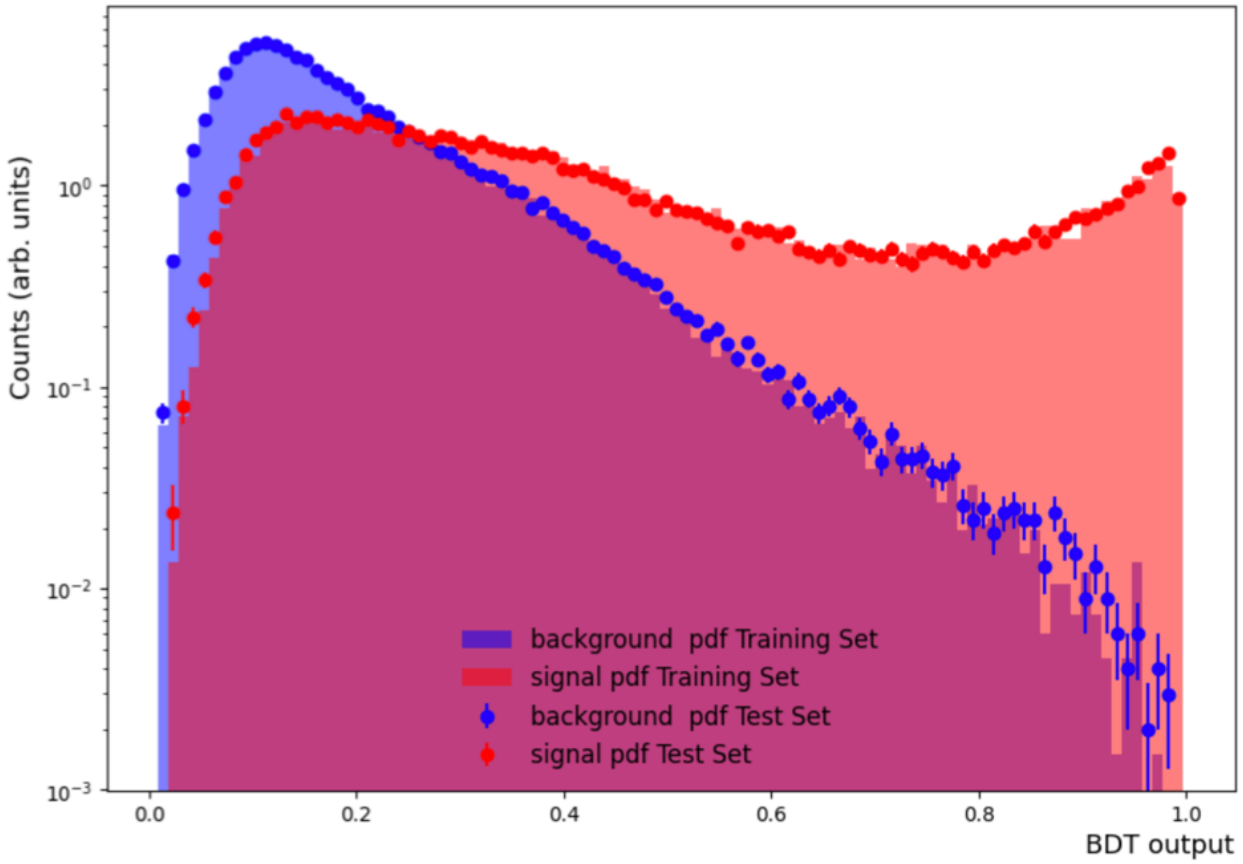

Figure 67: The distribution of the BDT score among signal and background for decay geometry combined with Nsigma response from TPC and TPC as final strategy

prevents the signal peak from being visually discernible in the mass distribution at low BDT scores. Therefore, an optimal point on the BDT scale must be identified where the fitting procedure is still considered reliable. Finding the optimum point in setting BDT thresholds involves first evaluating the expected signal which is based on theoretical predictions or experimental measurements. The efficiency of the BDT is calculated by determining the fraction of the signal that remains after each BDT cut relative to the total initial number of signal events. As we increase the BDT threshold, we observe a monotonic decrease in the base ground signal, The calculated extracted signal can then be plotted as a function of BDT cuts. The significance in the fitting procedure of the mass distribution is calculated as the fraction of the integral of the Gaussian part within three standard deviations and integrating the background function. Significance is defined as the ratio of the signal to the square root of the sum of the signal plus background. This variable is based on the mass distribution without any BDT selection applied. When applying BDT selection to our fitting procedure, it is necessary to evaluate the effect of BDT on the background. Instead of using significance, we should use a variable called pseudo-significance (Figure 68, bottom, right), which is the product of significance and a correction factor derived from the ratio of the expected signal (Figure 68, top, right) to the extracted signal. The expected signal, taken from theoretical predictions, is manually combined with the sidebands of the data representing the background. The fitting procedure is then performed on this toy model to extract the dependence of significance on the BDT selection. The extracted signal (Figure 68, top, left) evaluated with the above methods is summarized in Table 15 and Figure 69 shows the the invariant mass of the $\Lambda_c^+ \to pK^-\pi^+$, after the BDT cuts applied for the minimum bias

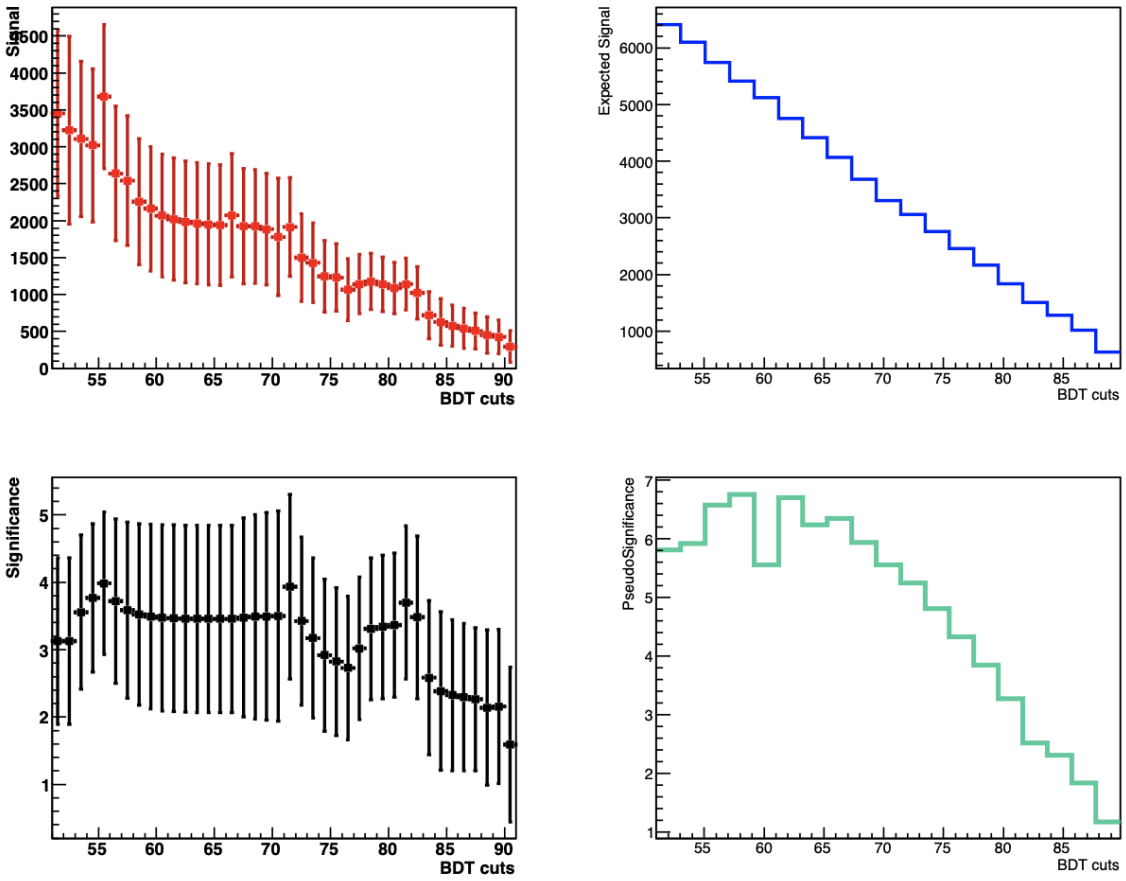

Figure 68: Calculating the pseudo-significance of the extracted signal using the theoretical prediction and estimation of the background effect for the minimum bias, Top Left: Raw yield vs BDT cuts, Top Right: Expected signal vs BDT, Bottom Left: Significance of the yield vs BDT, Bottom Right: pseudo-significance vs BDT

Table 15: BDT threshold cuts for each centrality bin: MB, 0-10%, 60-100%

Multiplcity class	BDT cut	Extracted Signal	Corrected Signal	Number of events
Minimum bias	0.51	3378	6752	599M
0-10% (most central)	0.61	991	2470	62 M
60-100% (least central)	0.51	492	984	243M

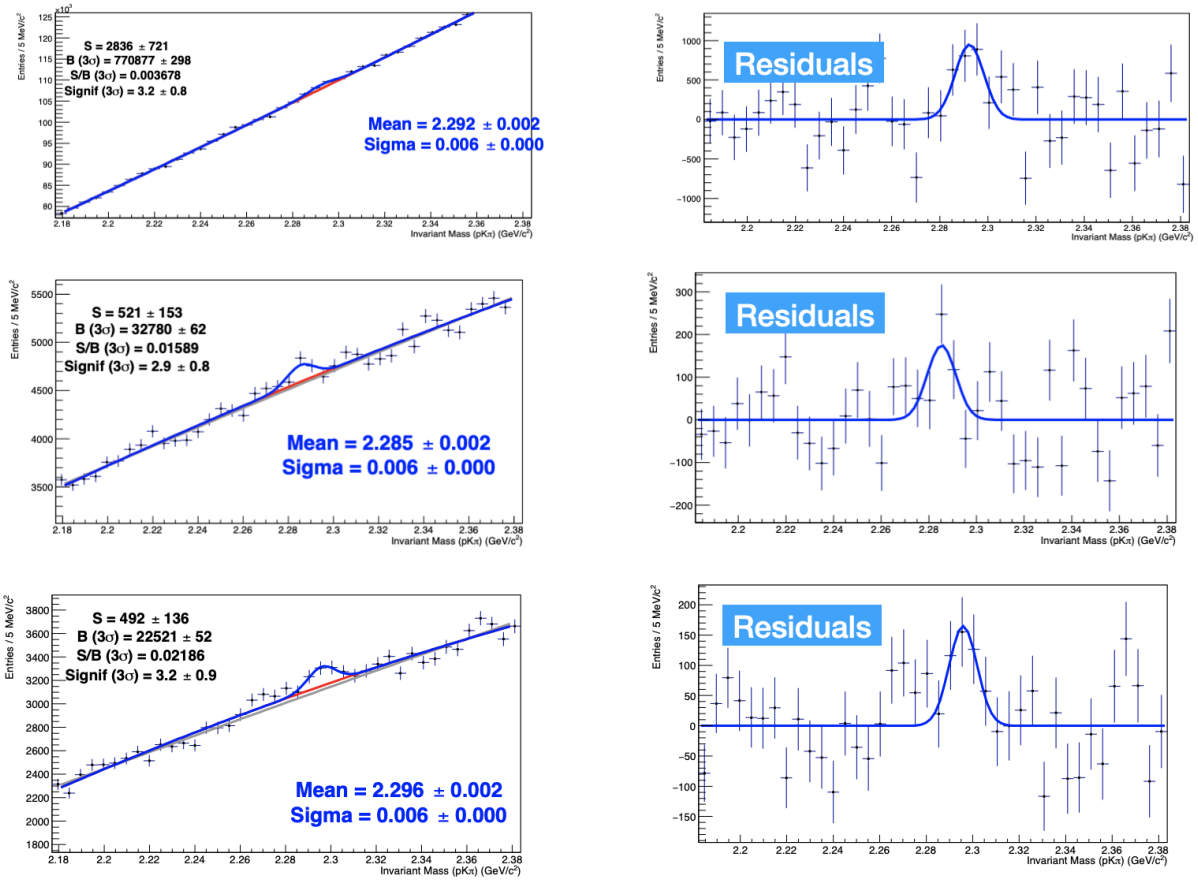

Figure 69: Extracted signal for minimum bias (top), the most central (middle), and the most peripheral collisions (bottom).

6 Conclusion

The results are presented for the Λ_c^+/D^0 ratios across three multiplicity classes, including the lowest and highest multiplicity classes, as shown in Figure 70. Figure 71 compares the Λ_c^+/D^0 ratios in p-Pb collisions with those in high-multiplicity in pp (Figure 71, left) and Pb-Pb collisions (Figure 71, right)[100]. These p_T differential ratios can be utilized to assess the p_T dependence of hadronization, serving as a tool to explore the momentum distribution between reconstructed Λ_c^+ and D^0. The Multiplicity in p-Pb collisions is higher than in the minimum bias pp collisions, with the p-Pb collision showing $dN_{ch}/d\eta \approx 17$ charged particles in the SPD, and pp shows $dN_{ch}/d\eta \approx 6$. Thus, the Pb nuclei generate more scattered charged particles in p-Pb compared to pp collisions, increasing the combinatorial background in the reconstruction of the D^0 and Λ_c^+. This background results in the dilution of the signal. The available statistics for pp collisions are approximately four times larger than those for proton-lead collisions leading to smaller statistical error bars. The significant expansion of systematic error bars in p-Pb collisions (see Figure 70, right) can be largely attributed to the challenges in extracting the raw yield, which is heavily influenced by the combinatorial background. Variability in the mass plots around the expected physical mass introduces substantial uncertainty in subtracting the background, leading to variations in the area under the curve of the anticipated signal,especially noticeable in the $2 < p_T < 4\,\mathrm{GeV}/c$ interval. This issue becomes more effective by the limited data available for the most central events (around 60M) and the most peripheral events (approximately 240M) in p-Pb, in contrast to the nearly 300 million events recorded for the highest multiplicity pp collisions and a billion for the lowest multiplicity collisions. .

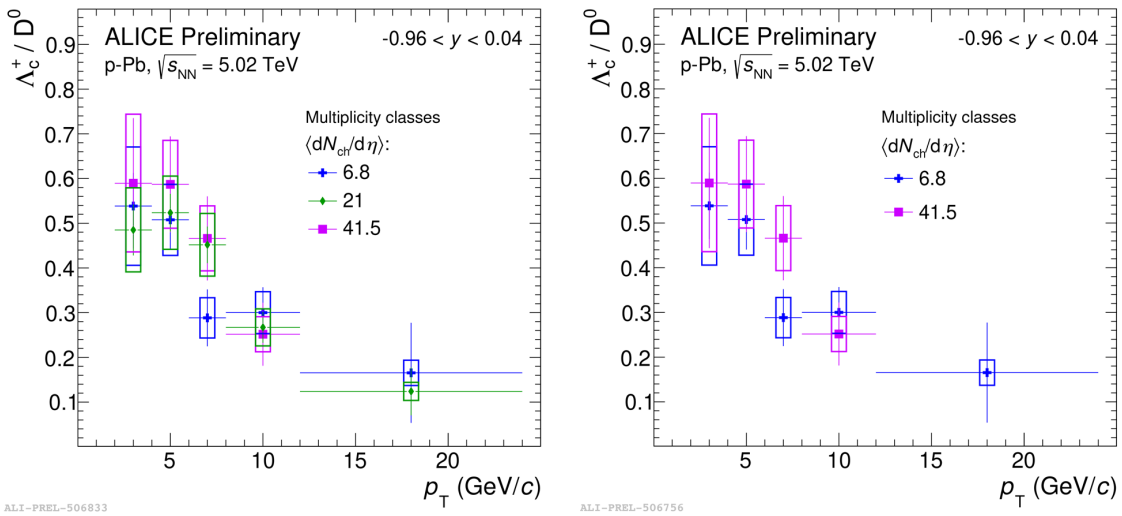

Figure 70: p_T differential Λ_c^+/D^0 ratio across three multiplicity classes (left) and a comparison between the most and least central multiplicity classes (right).

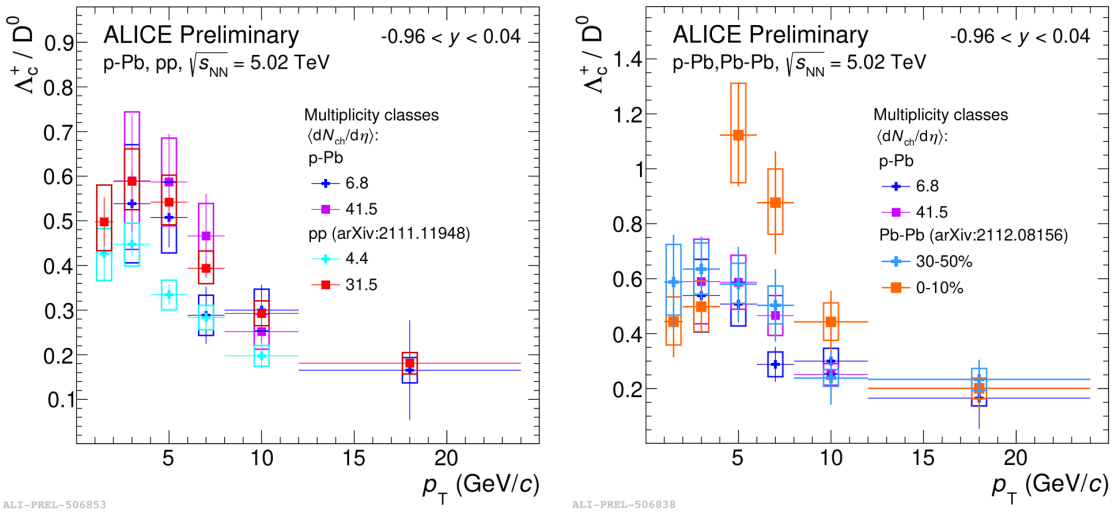

Figure 71: p_T-differential Λ_c^+/D^0 production yield ratios for three intervals of charged-particle multiplicity in p–Pb collisions at $\sqrt{s_{NN}} = 5.02$ TeV compared with measurements in pp (left) and Pb–Pb collisions (right) at the same center-of-mass energy.

6.1 Comparison between p-Pb and pp multiplicity measurements

In general, the comparison between the baseline pp and p-Pb collisions (see Figure 71, left) can be utilized to evaluate the cold nuclear matter (CNM) effect. CNM effects change the hadron spectrum in p-Pb collisions compared to pp collisions. These effects are measured

using nuclear suppression factors for each type of hadron. These changes occur because of the lead nuclei, which include 207 more nucleons than a single proton. This difference creates a potential that changes the Parton Distribution Functions (PDFs) of the partons in each nucleon. Shadowing, an example of an initial state effect, happens when the density of partons decreases because of the presence of additional nucleons. Other initial state effects include antishadowing, where parton densities go up at certain momentum fractions, and the EMC effect, which shows a surprising change in how muons scatter off nucleons in heavy nuclei compared to deuterium. This shows that the quark structure of nucleons changes when they are part of a nucleus. Another effect, Fermi motion, affects parton momentum because of how nucleons move inside the nucleus. Due to quantum mechanics, nucleons aren't still within the nucleus; they move around, their positions and momenta limited by the Heisenberg uncertainty principle and the nuclear potential. The Cronin effect results in more hadron production at intermediate transverse momenta because of multiple scatterings before the main scattering event. In contrast, final state effects involve interactions after the partons have scattered. For example, produced particles may scatter again within the Pb nuclei, leading to energy loss or absorption of outgoing hadrons by the nuclear medium. These various effects help explain the complex dynamics of particle production in p-Pb collisions.

The evaluation of the results demonstrates that the Λ_c^+/D^0 ratio (Figure 71, left) shows no significant dependence on multiplicity, even with the notable 5.3 sigma deviation observed in pp collisions. This consistency across the three multiplicity intervals suggests that in p-Pb collisions, the p_T differential ratios of Λ_c^+/D^0 do not vary significantly across different multiplicity classes. This implies that in p-Pb collisions, the multiplicity, which serves as an indicator of the system size, has a minimal impact on the p_T differential ratios of Λ_c^+/D^0 . A comparison of the lowest multiplicity classes in both pp and p-Pb collisions reveals consistent ratios across all p_T bins, except for the 4-6 and 6-8 GeV/c intervals (see Figure 71, left), suggesting an enhancement of the Λ_c^+/D^0 ratios when comparing the lowest multiplicity

classes in both types of collisions. This could be interpreted as an indication of the peak shift to the higher p_{T} in the least Central collisions in p-Pb, compared the similar multiplicity class in pp. Furthermore, an analysis of the highest multiplicity classes in both p-Pb and pp collisions shows uniform ratios across all p_T bins, indicating that the ratio converges at higher multiplicities. This suggests that as the multiplicity increases, the hadronization mechanisms in both environments become similar, and it appears that cold nuclear matter effects do not influence the hadronization of $\Lambda_{\mathrm{c}}^{+}/\mathrm{D}^{0}$ significantly.

6.2 Comparison between p-Pb and Pb-Pb multiplicity measurements

Comparing the p-Pb and Pb-Pb collision data (see Figure 71, right), we observe that the semi-central ratios in Pb-Pb collisions align with both the highest and lowest multiplicity ratios in p-Pb collisions. This alignment suggests that Pb-Pb events with lower multiplicities (around 400 charged particles) exhibit hadronization patterns similar to those seen in pp and p-Pb collisions. However, the most central Pb-Pb collisions display a significant change in the $\Lambda_{\mathrm{c}}^{+}/\mathrm{D}^{0}$ ratio, which could be attributed to the influence of the quark-gluon plasma. This influence is particularly noticeable at $4 < p_T < 6$ GeV/c, where the enhancement of the $\Lambda_{\mathrm{c}}^{+}/\mathrm{D}^{0}$ ratio beyond unity signifies an increased production of baryons in a specific momentum range, potentially due to a redistribution of momentum from the D^0 to the Λ_c^+. The peak of the $\Lambda_{\mathrm{c}}^{+}/\mathrm{D}^{0}$ is significantly shifted to higher p_{T}, comparing the peak in pp and p-Pb at 2-4 GeV/c to the 4-6 GeV/c, indicating the effect of radial flow in the quark gluon plasma, hardening the maxium of the $\Lambda_{\mathrm{c}}^{+}/\mathrm{D}^{0}$ ratio by increasing the average momentum of the tracks, leading to shift of p_{T} of the reconstructed candidates.

6.3 $\Lambda_{\mathrm{c}}^{+}/\mathrm{D}^{0}$ across pp, p-Pb, and Pb-Pb collisions

The p_T-integrated results for the $\Lambda_{\mathrm{c}}^{+}/\mathrm{D}^{0}$ (see Figure 72 for pp collisions, see Figure 73 for this ratio across all nucleon-nucleon systems). This ratio indicate no dependency on the system size, implying that the overall ratio remains constant and the hadrochemistry pertaining to

Λ_c^+/D^0 is consistent across different collision systems. However, the mechanisms involved in hadronization could alter the momentum distribution in such a way that p_T differential Λ_c^+/D^0 ratio becomes multiplicity-dependent at certain p_T ranges, including 4-6 GeV/c and 6-8 GeV/c across all the collision systems (see Figure 74). This suggests that the numbers of D^0 and Λ_c^+ are predominantly determined by the nucleon-nucleon collisions where the ratio is 30 percent in the nucleon-nucleon system, compared to 10 percent in e^+e^- and ep collisions. In nucleon-nucleon environments tend to generate more Λ_c^+ and other types of baryons, such as Ξ_c, relative to e^+e^- and ep collisions which was discussed as non-universality of fragmentation in chapter 3. The enhancement of the p_T-differential Λ_c^+/D^0 ratio in specific momentum ranges within Pb-Pb collisions is indicative of coalescence processes. This is because, in the dense environment of these collisions, charm quarks have a higher probability of combining with nearby light quarks to form Λ_c^+ baryons, leading to increased Λ_c^+/D^0 ratios at these p_T ranges. Although this enhancement occurs at particular p_T intervals, the overall p_T-integrated Λ_c^+/D^0 ratio remains constant across the spectrum, as the increases due to coalescence are offset by the broader, dominant fragmentation processes that prevail in other momentum ranges. As the system size or multiplicity increases, the enhanced density and volume of the medium promote conditions favorable for coalescence, leading to a more pronounced enhancement of Λ_c^+ production. As anticipated, the ratios in the high p_T windows, specifically for $12 < p_T < 24$ GeV/c, tend to converge towards the values predicted solely by fragmentation processes, similar to those observed in e^+e^- and ep collisions. This indicates that at higher p_T, the effects of the medium diminish, and fragmentation becomes the dominant hadronization mechanism, aligning the Λ_c^+/D^0 ratio closely with the 10% production typical in e^+e^- and ep environments.

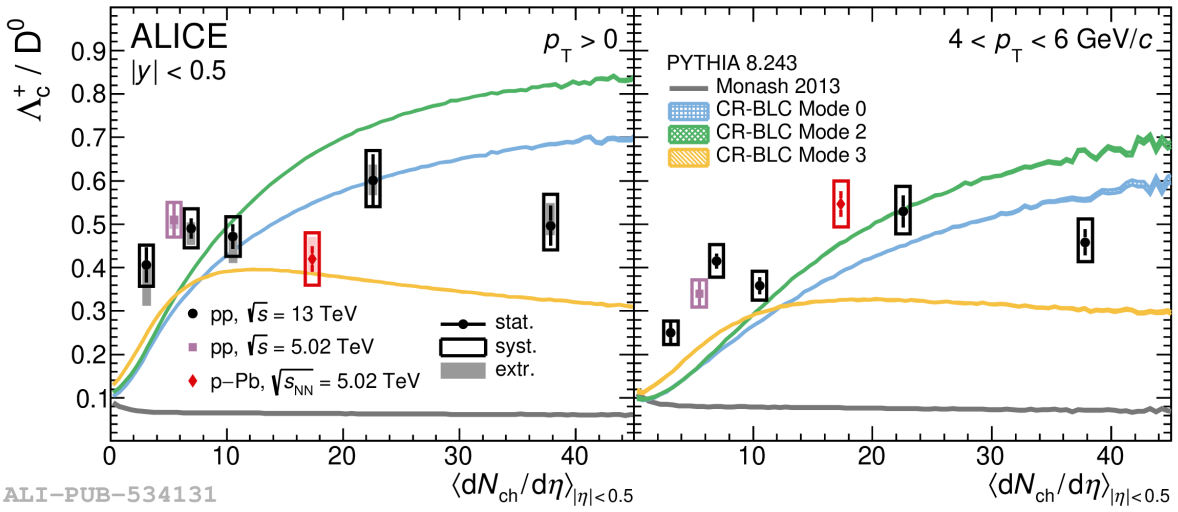

Figure 72: p_{T}-integrated $\Lambda_{\mathrm{c}}^{+}/\mathrm{D}^{0}$ yield ratios extrapolated for $p_{\mathrm{T}} > 0$ (left) and for the $4 < p_{\mathrm{T}} < 6$ GeV/c interval (right) for the pp collisions

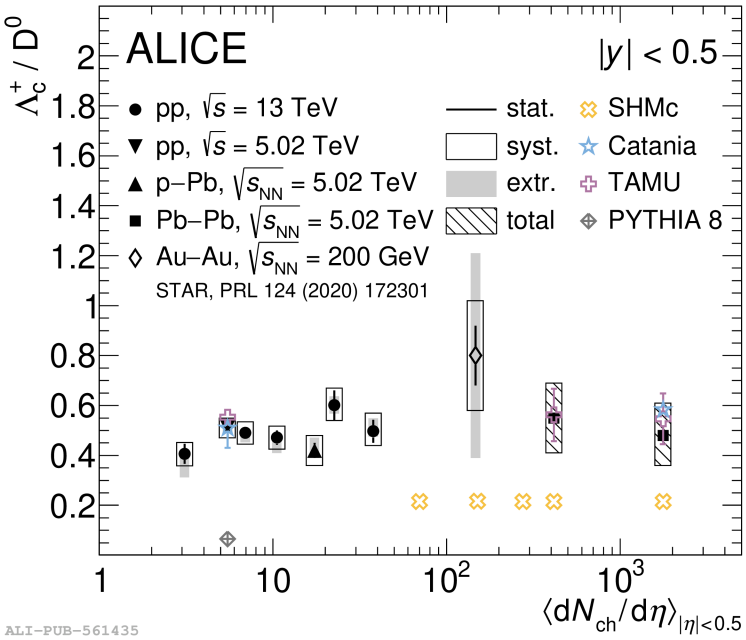

Figure 73: p_{T}-integrated $\Lambda_{\mathrm{c}}^{+}/\mathrm{D}^{0}$ yield ratios extrapolated for $p_{\mathrm{T}} > 0$ across all nucleon-nucleon systems as function of multiplicity

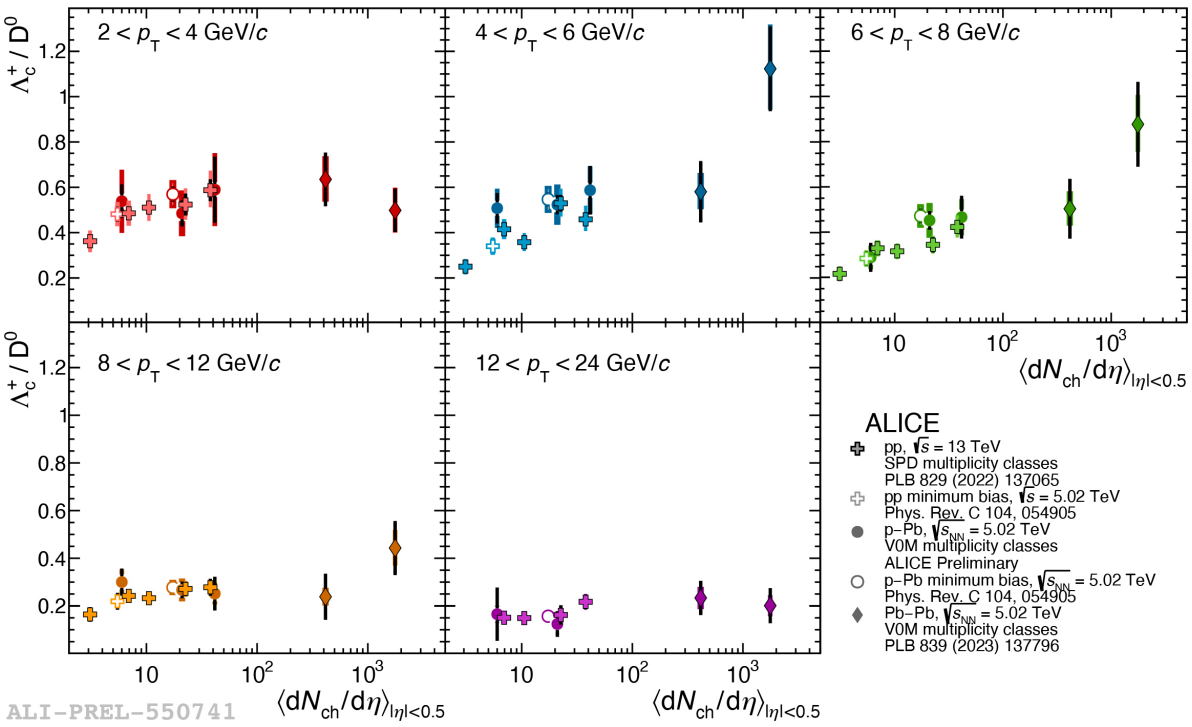

Figure 74: p_{T}-differential $\Lambda_{\mathrm{c}}^{+}/\mathrm{D}^{0}$ production yield ratios as a function of charged-particle multiplicity in pp, p–Pb, and Pb–Pb collisions at $\sqrt{s_{\mathrm{NN}}} = 5.02$ TeV

6.4 Comparison between p-Pb and pp minimum bias measurements

In Figure 75, one can observe the minimum bias analysis of the $\Lambda_{\mathrm{c}}^{+}/\mathrm{D}^{0}$ ratio in pp and p-Pb collisions through the $\Lambda_c^+ \to pK_S^0$ decay channel. The consistency between this and other hadronic decay channels is discussed in Chapter 5. These measurements extend the $\Lambda_{\mathrm{c}}^{+}/\mathrm{D}^{0}$ ratios into lower p_T bins, owing to the distinctive geometry of the decay. Comparing results between pp and p-Pb collisions necessitates consideration of the analysis strategy. Specifically, the analysis within the minimum bias dataset of p-Pb collisions effectively captures smaller p_T ranges (0.1-1 GeV/c, 1-2 GeV/c, 2-3 GeV/c, and 3-4 GeV/c), highlighting a shift in the peak from pp to p-Pb collisions. The $\Lambda_c^+ \to pK_S^0$ transition exhibits a more distinct signal (see Figure 75, left) compared to the $\Lambda_{\mathrm{c}}^{+} \to \mathrm{pK}^{-}\pi^{+}$ transition. This is primarily because K_S^0 particles are less prone to be formed from unrelated kaon and pion pairings, thereby reducing combinatorial noise. The observed signal width for $\Lambda_c^+ \to pK_S^0$ in the $0.1-1$ GeV/c and $1-2$

GeV/c ranges is broader by 8 MeV/c^2 compared to that of $\Lambda_c^+ \to pK^-\pi^+$, which exhibits a width of 6 MeV/c^2.

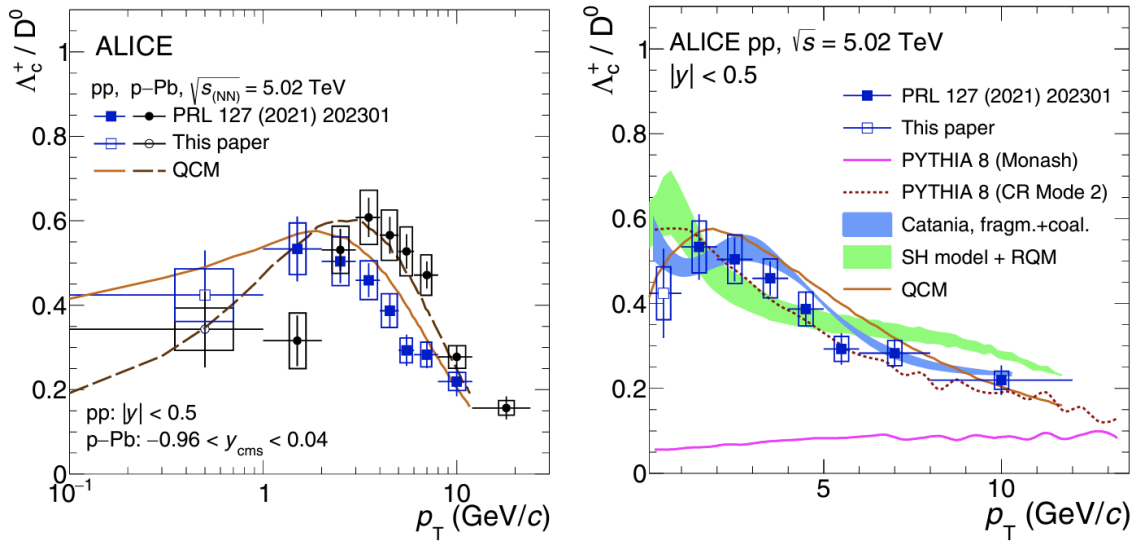

Figure 75: The p_T-differential Λ_c^+/D^0 production yield ratios in p–Pb and pp collisions for minimum bias analysis are documented in [99], with a comparison to the Quark Coalescence Model (QCM) [101, 102]. Additionally, the p_T-differential Λ_c^+/D^0 production yield ratios in pp collisions under minimum bias conditions are compared to predictions by PYTHIA (Monash+Color Reconnection) [103, 104], the Catania model [105], Statistical hadronization models [106], and QCM [102].

6.5 Quark (re)Combination Model (QCM)

This model (see Figure 75, right) stands out among the various models attempting to explain the transition from pp to p-Pb collisions. It successfully accounts for the shift of the peak to higher p_T when moving from pp to p-Pb collisions, attributed to the incorporation of coalescence and radial flow into the QCM. This model adopts a thermal approach to hadronization, wherein a charm quark can combine with light quarks to form either a Λ_c^+ or a D^0, depending on their proximity in phase space (both spatially and in momentum). The light quarks are presumed to be thermally distributed, following the Fermi-Dirac distribution. Additionally, each baryon and meson is assigned a degeneracy factor, reflecting the various possible configurations of color charge, isospin, and quark spin. The coalescence mechanism,

as opposed to fragmentation, operates in an inverse manner. Fragmentation typically leads to a reduction in momentum as charm quarks break down into lower-momentum partons. Conversely, coalescence tends to increase the momentum by merging partons, thereby enhancing the resultant particle's momentum. When fragmentation is solely implemented in models like PYTHIA, it fails to produce any p_T-dependent effects, indicating a uniform fragmentation behavior across different p_T ranges. However, the combination of fragmentation and coalescence in a unified model explains the observed enhancements. Specifically, while fragmentation establishes the baseline ratio, coalescence contributes to an increase in Λ_c^+ production, particularly in the p_T range of 2-4 GeV/c, predicting and accounting for the peak and its shift with system size. This collaboration between fragmentation and coalescence allows the model to predict the peak and adjust for its shift corresponding to the size of the system, effectively capturing the dynamics influenced by the transition from pp to p-Pb collisions.

6.6 Statistical Hadronization Models

The Statistical Hadronization Model is a framework that employs a statistical method to calculate the yields of particles based on their mass and the temperature at the freeze-out surface in canonical ensemble scheme [95, 96, 107]. This model does not implement any microscopic mechanisms for hadronization, using instead statistical approach to assign a temperature to different species of hadrons. It relies on the masses of the observed hadronic states. Once the temperature is derived from fits to the light hadron spectrum, energy can be statistically allocated among various hadrons of different masses to deduce their yields and the p_T spectrum. The success of the Statistical Hadronization Model relies on the number of measured states listed in the Particle Data Group. This model aligns well with the light hadron spectrum and supports the flavor dependent hierarchy in the light sector, suggesting that strange hadrons reach freeze-out earlier or at higher temperatures compared to non-strange hadrons. However, the applicability of this model to heavy-flavor

sectors remains controversial, largely due to the necessity of incorporating a fugacity factor to account for the non-thermal nature of the charm quark. In the context of the canonical ensemble approach, incorporating additional states from relativistic quark models allows for a reproduction of the Λ_c^+/D^0 ratio's shape, though it falls short of matching the exact peak value for the most central collisions. Nevertheless, this adaptation shows improved alignment with low-multiplicity pp collision results. Despite these successes, the model tends to overestimate the D_s^+/D^0 ratio (see Figure 76, top). While it successfully captures the flat p_T trend for the lower multiplicity classes—accurate to within about 20 percent it tends to over-predict the yields in this sector, highlighting the challenges in accurately modeling heavy-flavor hadronization in the strange sector. As we discussed in chapter 3, mode 0, mode2, and mode 3 can capture the multiplicity dependency of the Λ_c^+/D^0 ratio, but fail to reproduce the peak shape and their transition to higher p_T in higher multiplicities. This model however fails to reproduce the p_T integrated Λ_c^+/D^0 ratio correctly (see Figure 72)

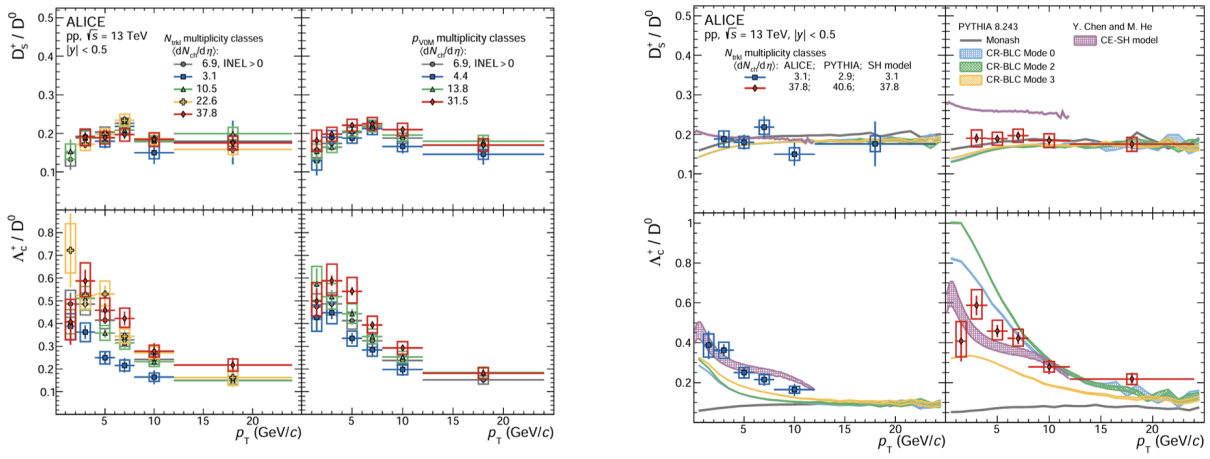

Figure 76: p_T-differential D_s/D^0 (top) and Λ_c^+/D^0 (bottom) production yield ratios in pp collisions (left) and the comparison of the data with PYTHIA and Statictical hadronization model in canonical ensemble (right) [95, 96, 107]

6.7 PYTHIA and the problem of baryonization

Different modes of PYTHIA can be observed in Figure 72, right, and Figure 76, right, which correspond to constraints on the hadronization parameters, primarily the time dilation needed for two di-quarks or a di-quark and a parton to form a new flux tube [104]. Modes 0 and 2 impose the least strict conditions for color reconnection beyond the leading color. In contrast, Mode 3 applies the most stringent condition for color reconnection. As discussed in Chapter 3, all three modes can explain the multiplicity dependency of the p_{T}-differential $\Lambda_{\mathrm{c}}^{+}/\mathrm{D}^{0}$ ratio in pp collisions but fail to predict the peak value and the shift to higher p_{T} as the system size increases. For the p_{T}-integrated results, Modes 0 and 2, which allow more frequent color reconnection, predict a steep increase in the $\Lambda_{\mathrm{c}}^{+}/\mathrm{D}^{0}$ ratio as a function of multiplicity at low multiplicity where there is no data point to investigate that. However, the data points suggest a uniform ratio across multiplicities. Mode 3, despite a similar rise at low multiplicity, shows the saturation of the $\Lambda_{\mathrm{c}}^{+}/\mathrm{D}^{0}$ ratio at high multiplicities. However, the values predicted by Mode 3 deviate from the actual data (approximately 30%) and tend to converge to the results observed in $e^{+}e^{-}$ and ep collisions (approximately10%).When expanding the investigation of PYTHIA to other species of charmed baryons, such as Ξ_c/D^0 (see Figure 77, right), it is observed that the p_{T}-differential ratio is significantly underestimated by the three modes of PYTHIA, as well as by the Coalescence model and the Statistical Hadronization Model (SHM). This indicates a failure to propose a universal framework for charmed baryon formation, especially concerning strange content (Ξ_c and D_s^+). Even though these models can approximately explain the $\Lambda_{\mathrm{c}}^{+}/\mathrm{D}^{0}$ ratio, the lightest charm baryon to the lightest charmed meson (see Figure 77, left), they fall short in providing a comprehensive understanding of the formation mechanisms for all charmed baryon species.

6.8 Future outlook

In Run 3, which commenced in 2022 following the lengthy shutdown of Run 2, the ALICE Collaboration entered a new era of data acquisition. During this period, the detectors and

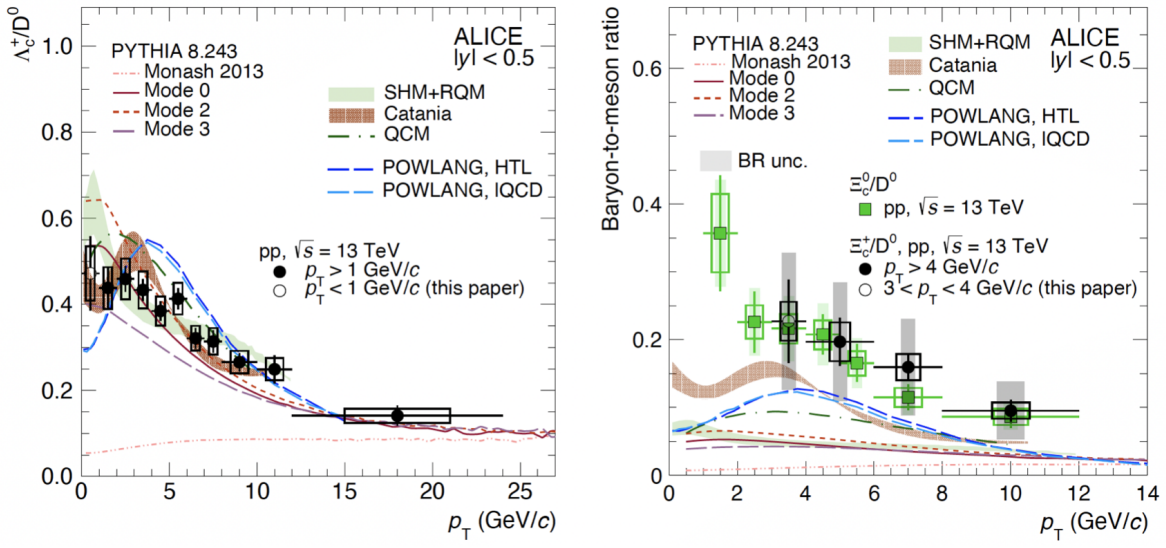

Figure 77: p_{T}-differential $\Lambda_{\mathrm{c}}^{+}/\mathrm{D}^{0}$ (left) and Ξ_c/D^0 (right) production yield ratios in pp collisions (Left) and the comparison of the data with PYTHIA and Statictical hadronization model in canonical ensemble (Right)[95]

sub-detectors within the ALICE experiment were significantly enhanced. Most notably, the resolution of the Inner Tracking System (ITS) was increased, and the Time Projection Chamber (TPC) resolution and readout systems were substantially upgraded with cutting-edge technologies. Concurrently, the luminosity of the beam was increased, leading to a higher interaction rate. These enhancements in the detector capabilities, combined with enhanced readout power, have facilitated a shift from an event-by-event system to continuous readout, allowing for more efficient data collection and analysis. In such a case, the increased statistics will be more readily available to expand similar analyses in the heavy flavor sector, enabling finer p_T and multiplicity binning, which leads to more accurate data. Alongside this, efforts are being focused on developing multi-purpose event generators up to the point where a more universal approach towards hadronization can be understood.

Bibliography

[1] R. Hagedorn. Statistical thermodynamics of strong interactions at high energies. *Nuovo Cimento Suppl.*, 3:147–186, 1965.

[2] R. Hagedorn. Hadronic matter near the boiling point. *Nuovo Cimento A*, 56(4):1027–1057, 1968.

[3] R. Hagedorn and J. Ranft. Statistical thermodynamics of strong interactions at high-energies. *Nuovo Cimento, Supplement*, 6:169–354, 1968. Report number: CERN-TH-851.

[4] G. Zweig. An SU(3) Model for Strong Interaction Symmetry and its Breaking. *CERN Report*, 1964. Report No. 8419/TH.412.

[5] M. Y. Han and Y. Nambu. Three-triplet model with double SU(3) symmetry. *Physical Review B*, 139(4B):1006, 1965.

[6] M. Gell-Mann. A schematic model of baryons and mesons. *Physics Letters*, 8(3):214–215, Jan. 1964.

[7] E. D. Bloom, D. H. Coward, H. DeStaebler, J. Drees, G. Miller, L. W. Mo, R. E. Taylor, M. Breidenbach, J. I. Friedman, G. C. Hartmann, and H. W. Kendall. High-Energy Inelastic e-p Scattering at 6° and 10°. *Physical Review Letters*, 23(16):930, oct 1969.

[8] M. Breidenbach et al. Observed behavior of highly inelastic electron–proton scattering. *Physical Review Letters*, 23(16):935–939, 1969.

[9] O. W. Greenberg. Spin and unitary-spin independence in a paraquark model of baryons and mesons. *Physical Review Letters*, 13(20):598–602, 1964.

[10] O. W. Greenberg. Color charge degree of freedom in particle physics. *Contemporary Physics*, 19(3):267–278, 1978.

[11] O. W. Greenberg. Color in particle physics. *Foundations of Physics*, 39(7):766–779, 2009.

[12] R. P. Feynman. Space-time approach to quantum electrodynamics. *Physical Review*, 76(6):769–789, 1949.

[13] J. Schwinger. On quantum-electrodynamics and the magnetic moment of the electron. *Physical Review*, 73(4):416–417, 1948.

[14] S. Tomonaga. On a relativistically invariant formulation of the quantum theory of wave fields. *Progress of Theoretical Physics*, 1(2):27–42, 1946.

[15] C. N. Yang and R. L. Mills. Conservation of isotopic spin and isotopic gauge invariance. *Physical Review*, 96(1):191–195, 1954.

[16] H. D. Politzer. Reliable perturbative results for strong interactions? *Physical Review Letters*, 30(26):1346, 1973.

[17] D. J. Gross and F. Wilczek. Asymptotically free gauge theories. i. *Physical Review D*, 8(10):3633, 1973.

[18] D. J. Gross and F. Wilczek. Ultraviolet behavior of non-abelian gauge theories. *Physical Review Letters*, 30(26):1343, 1973.

[19] C. G. Callan Jr, R. Dashen, and D. J. Gross. Toward a theory of the strong interactions. *Physical Review D*, 17(10):2717, 1973.

[20] G. 't Hooft. Renormalization of massless yang-mills fields. *Nuclear Physics B*, 33(1):173–199, 1971.

[21] S. Glashow, J. Iliopoulos, and L. Maiani. Weak interactions with lepton-hadron symmetry. *Physical Review D*, 1970.

[22] S. Glashow, J. Iliopoulos, and L. Maiani. Weak interactions with lepton-hadron symmetry. *Physical Review D*, 2:1285–1292, 1970.

[23] M. Kobayashi and T. Maskawa. CP-Violation in the Renormalizable Theory of Weak Interaction. *Progress of Theoretical Physics*, 1973.

[24] B. Richter et al. Observation of a New Particle in the Search for the Monopole at the SLAC SPEAR Detector. *Physical Review Letters*, 33:1406–1408, 1974.

[25] S. Ting et al. Discovery of a Narrow Resonance in e^+e^- Annihilation. *Physical Review Letters*, 33:1404–1406, 1974.

[26] et al Herb. Observation of a Dimuon Resonance at 9.5 GeV in 400-GeV Proton-Nucleus Collisions. 1977.

[27] B. Knapp et al. Evidence for a narrow anti-charmed baryon state. *Physical Review Letters*, 1976.

[28] S. W. Herb, D. C. Hom, L. M. Lederman, J. C. Sens, H. D. Snyder, J. K. Yoh, et al. Observation of Upsilon Resonance Production in 400 GeV Proton-Nucleus Collisions. *Phys. Rev. Lett.*, 39:252–255, 1977.

[29] S. Behrends et al. Observation of B Meson Production. *Physical Review Letters*, 1980.

[30] C. Albajar et al. First Observation of the Beauty Baryon Λ_b^0 in the Decay $\Lambda_b^0 \to J/\Psi\Lambda$. *Physics Letters B*, 1991.

[31] F. Abe et al. Observation of Top Quark Production in $\bar{p}p$ Collisions with the Collider Detector at Fermilab. *Physical Review Letters*, 74(2626), 1995.

[32] S. Abachi et al. Observation of the top quark. *Physical Review Letters*, 74(2632), 1995.

[33] A. Einstein. The field equations of gravitation. *Prussian Academy of Sciences*, 1915.

[34] A. Friedmann. Über die krümmung des raumes. *Zeitschrift für Physik*, 10(1):377–386, 1922.

[35] G. Lemaître. A homogeneous universe of constant mass and growing radius accounting for the radial velocity of extra-galactic nebulae. *Annales de la Société Scientifique de Bruxelles*, 47:49–59, 1927.

[36] R. A. Alpher and R. C. Herman. On the relative abundance of the elements. *Physical Review*, 74(12):1737–1742, 1948.

[37] A. A. Penzias and R. W. Wilson. A Measurement of Excess Antenna Temperature at 4080 Mc/s. *Astrophysical Journal*, 142:419–421, 1965.

[38] E. Shuryak. Quantum chromodynamics and the theory of superdense matter. *Physics Reports*, 61(2):71–158, 1980.

[39] M. Neubert. Heavy quark symmetry. *Physics Reports*, 245(5-6):259–396, 1994.

[40] V. E. Barnes et al. Observation of a hyperon with strangeness -3. *Physical Review Letters*, 12:204–206, 1964.

[41] K. M. Watson. Theory of the capture of negative pions by complex nuclei. *Physical Review*, 88(5):1163–1171, 1952.

[42] R. Brandelik et al. Evidence for Planar Events in e^+e^- Annihilation at High Energies. *Physics Letters B*, 86(2):243–249, 1979.

[43] J. Ellis and I. Karliner. Measuring the spin of the gluon in e^+e^- annihilation. *Nuclear Physics B*, 148(1):141–147, 1979.

[44] R. Brandelik et al. Evidence for a spin-1 gluon in three-jet events. *Physics Letters B*, 97(3-4):453–458, 1980.

[45] C. Berger et al. A study of multi-jet events in e^+e^- annihilation. *Physics Letters B*, 97(3-4):459–464, 1980.

[46] G. Alexander et al. Measurement of Three-Jet Distributions Sensitive to the Gluon Spin in e^+e^- Annihilations at $s = 91$ GeV. *Zeitschrift für Physik C*, 52(4):543, 1991.

[47] K. G. Wilson. Renormalization group and critical phenomena. *Physical Review B*, 4(9):3174–3183, 1971.

[48] Kenneth G. Wilson. Confinement of quarks. *Physical Review D*, 10(8):2445, 1974.

[49] J. Greensite. *An Introduction to the Confinement Problem*. Springer, 2011.

[50] S. Coleman. *Aspects of Symmetry: Selected Erice Lectures*. Cambridge University Press, 1985.

[51] T. Schäfer and E. V. Shuryak. Instantons in QCD. *Rev. Mod. Phys.*, 70:323–426, 1998.

[52] D. Diakonov. Instantons at work. *Prog. Part. Nucl. Phys.*, 51:173–222, 2003.

[53] M. Gell-Mann and M. Lévy. The axial vector current in beta decay. *Nuovo Cimento*, 16(4):705–726, 1960.

[54] M. Lévy. Possible existence of a meson with mass intermediate between the electron mass and the nucleon mass. *Proceedings of the Physical Society, Section A*, 80(4):781, 1962.

[55] J. Schwinger. A theory of the fundamental interactions. *Annals of Physics*, 2(5):407–434, 1957.

[56] J. Schwinger. On gauge invariance and vacuum polarization. *Physical Review*, 82(5):664–679, 1951.

[57] J. Jalilian-Marian, A. Kovner, L. McLerran, and H. Weigert. The intrinsic glue distribution at very small x. *Phys. Rev. D*, 55:5414–5428, 1997.

[58] Y. V. Kovchegov. Small-x F2 structure function of a nucleus including multiple pomeron exchanges. *Phys. Rev. D*, 60:034008, 1999.

[59] E. Iancu, A. Leonidov, and L. McLerran. Nonlinear gluon evolution in the color glass condensate i. *Nucl. Phys. A*, 692:583–645, 2001.

[60] E. Iancu and R. Venugopalan. The color glass condensate and high energy scattering in QCD. 2003.

[61] A. H. Mueller. Parton saturation at small x and in large nuclei. *Nucl. Phys. B*, 558:285–303, 2002.

[62] H. Weigert. Evolution at small x_{bj}: The color glass condensate. *Prog. Part. Nucl. Phys.*, 55:461–565, 2005.

[63] ALICE Collaboration. Enhanced production of multi-strange hadrons in high-energy nucleus-nucleus collisions. *Nature Physics*, 13:535–539, 2017.

[64] P. W. Anderson. More is different. *Science*, 177(4047):393–396, 1972.

[65] C. Ratti and R. Bellwied. Lecture notes in physics. *Lect. Notes Phys.*, 981:1–216, 2021.

[66] C. Ratti. Report on progress in physics. *Rept. Prog. Phys.*, 81:084301, 2018.

[67] J. C. Maxwell. *Theory of Heat*. Longmans, Green and Co., London, 1872.

[68] J. P. Joule. On the mechanical equivalent of heat. *Philosophical Transactions of the Royal Society of London*, 1845.

[69] S. Carnot. *Reflections on the Motive Power of Fire*. 1824.

[70] W. Nernst. On a new theoretical basis for the third law of thermodynamics. *Journal of the Royal Society*, 1906.

[71] L. Boltzmann. Further studies on the thermal equilibrium of gas molecules. *Sitzungsberichte Akademie der Wissenschaften, Vienna*, II, 1872.

[72] L. D. Landau. On the theory of phase transitions. *Zh. Eksp. Teor. Fiz.*, 7, 1937.

[73] Y. Aoki et al. The order of the quantum chromodynamics transition predicted by the standard model of particle physics. *Nature*, 443:675–678, 2006.

[74] S. Ejiri. Canonical partition function and finite density phase transition in lattice QCD. *Phys. Rev. D*, 78:074507, 2008.

[75] S. Gupta et al. Scale for the phase diagram of quantum chromodynamics. *Science*, 332:1525–1528, 2011.

[76] O. Philipsen. The QCD phase diagram at zero and small baryon density. *Prog. Part. Nucl. Phys.*, 70:55–107, 2013.

[77] C. Gale, S. Jeon, and B. Schenke. Hydrodynamic modeling of heavy-ion collisions. *Int. J. Mod. Phys. A*, 28:1340011, 2013.

[78] J. S. Moreland, J. E. Bernhard, and S. A. Bass. Alternative ansatz to wounded nucleon and binary collision scaling in high-energy nuclear collisions. *Phys. Rev. C*, 92:011901, 2015.

[79] U. Heinz and R. Snellings. Collective flow and viscosity in relativistic heavy-ion collisions. *Annu. Rev. Nucl. Part. Sci.*, 63:123–151, 2013.

[80] P. K. Kovtun, D. T. Son, and A. O. Starinets. Viscosity in strongly interacting quantum field theories from black hole physics. *Phys. Rev. Lett.*, 94:111601, 2005.

[81] HotQCD Collaboration, A. Bazavov, et al. Equation of state in (2+1)-flavor qcd. *Phys. Rev. D*, 90:094503, 2014.

[82] Fei Gao and Jan M. Pawlowski. Chiral phase structure and critical end point in qcd. *Physics Letters B*, 820:136584, 2021.

[83] ALICE Collaboration. The ALICE experiment at the CERN LHC. *JINST*, 3:S08002, 2008.

[84] A. D. Martin, W. J. Stirling, R. S. Thorne, and G. Watt. Parton distributions for the lhc. *The European Physical Journal C*, 63(2):189–285, 2009.

[85] R. D. Ball et al. Parton distributions with lhc data. *Nuclear Physics B*, 867(2):244–289, 2012.

[86] S. Dulat, T.-J. Hou, J. Gao, M. Guzzi, J. Huston, J. Pumplin, C. Schmidt, D. Stump, and C.-P. Yuan. New parton distribution functions from a global analysis of quantum chromodynamics. *Physical Review D*, 93(3):033006, 2016.

[87] R. P. Feynman. Very high-energy collisions of hadrons. *Physical Review Letters*, 23(24):1415–1417, 1969.

[88] J. D. Bjorken and E. A. Paschos. Inelastic electron-proton and -proton scattering and the structure of the nucleon. *Physical Review*, 185(5):1975–1982, 1969.

[89] G. Altarelli and G. Parisi. Asymptotic freedom in parton language. 1977.

[90] V. N. Gribov and L. N. Lipatov. Deep inelastic e p scattering in perturbation theory. *Soviet Journal of Nuclear Physics*, 15(4):438–450, 1972.

[91] Y. L. Dokshitzer. Calculation of the Structure Functions for Deep Inelastic Scattering and e^+e^- Annihilation by Perturbation Theory in Quantum Chromodynamics. *Soviet Physics JETP*, 46(4):641–653, 1977.

[92] B. Andersson et al. Parton fragmentation and string dynamics. *Physics Reports*, 97:31–145, 1983.

[93] T. Sjöstrand, S. Mrenna, and P. Skands. A Brief Introduction to PYTHIA 8.1. *Computer Physics Communications*, 178:852–867, 2008.

[94] P. Skands, S. Carrazza, and J. Rojo. Tuning pythia 8.1: the monash 2013 tune. *European Physical Journal C*, 74:3024, 2014.

[95] ALICE Collaboration. Charm production and fragmentation fractions at midrapidity in pp collisions at $\sqrt{s} = 13$ TeV. *Journal of High Energy Physics*, 2023(12):086, 2023.

[96] ALICE Collaboration. Observation of a multiplicity dependence in the pT-differential charm baryon-to-meson ratios in proton-proton collisions at $\sqrt{s} = 13$ TeV. *Physics Letters B*, 829:137065, 2022.

[97] Shreyasi Acharya et al. Measurement of prompt D^0, D^+, D^{*+}, and D_S^+ production in p–Pb collisions at $\sqrt{s_{NN}} = 5.02$ TeV. *JHEP*, 12:092, 2019.

[98] Roel Aaij et al. Measurement of b hadron fractions in 13 TeV pp collisions. *Phys. Rev. D*, 100(3):031102, 2019.

[99] ALICE Collaboration. First measurement of Λ_c^+ production down to $p_T = 0$ in pp and p–Pb collisions at $\sqrt{s_{NN}} = 5.02$ TeV . *Phys. Rev. C*, 107:064901, 2023.

[100] Oveis Sheibani. Measurements of prompt Λ_c^+/D^0 ratio as a function of multiplicity at midrapidity at $\sqrt{s}$=5.02 TeV. *arXiv:2312.15542.*, 2023.

[101] H.-h. Li, F.-L. Shao, J. Song, and R.-q. Wang. Production of single-charm hadrons by quark combination mechanism in pPb collisions at $\sqrt{s_{NN}} = 5.02$ TeV. *Physical Review C*, 97(6):064915, 2018.

[102] H. Li, F. Shao, and J. Song. Production of light-flavor and single-charmed hadrons in pp collisions at $\sqrt{s} = 5.02$ tev in an equal-velocity quark combination model. *Chinese Physics C*, 45(11):113105, 2021.

[103] P. Skands, S. Carrazza, and J. Rojo. Tuning PYTHIA 8.1: The Monash 2013 tune. *European Physical Journal C*, 74(3):3024, 2014.

[104] J. R. Christiansen and P. Z. Skands. String formation beyond leading colour. *Journal of High Energy Physics*, 2015(8):003, 2015.

[105] V. Minissale, S. Plumari, and V. Greco. Charm hadrons in pp collisions at lhc energy within a coalescence plus fragmentation approach. *Physics Letters B*, 821:136622, 2021.

[106] M. He and R. Rapp. Charm-baryon production in proton-proton collisions. *Physics Letters B*, 795:117, 2019.

[107] Y. Chen and M. He. Charged-particle multiplicity dependence of charm-baryon-to-meson ratio in high-energy proton–proton collisions. *Phys. Lett. B*, 815:136144, 2021.